ABSTRACT

Title of dissertation: NOVEL TRANSPORT PROPERTIES OF ELECTRON-DOPED SUPERCONDUCTORS $Pr_{2-x}Ce_xCuO_{4-\delta}$

Pengcheng Li, Doctor of Philosophy, 2007

Dissertation directed by: Professor Richard L. Greene
Department of Physics

The main focus of this thesis is the study of transport properties [thermomagnetic (Nernst) and thermoelectric (Seebeck) effects, Hall effect and magentoresistance in high magnetic field up to 58 T] of the electron-doped cuprate superconductor system $Pr_{2-x}Ce_xCuO_{4-\delta}$. One chapter of this thesis is devoted to a study of the vortex Nernst effect in Pr doped $YBa_2Cu_3O_{7-\delta}$ films.

Electron-doped cuprate superconductors have demonstrated many distinct properties from their hole-doped counterparts. A few of them are investigated in this thesis. For example, by taking advantage of the low upper critical field, we investigated the field driven normal state thermoelectric power at low temperature in $Pr_{2-x}Ce_xCuO_{4-\delta}$ films with various doping. We observed an abrupt change of low temperature thermopower at a critical doping x=0.16. The kink behavior in the doping dependent thermopower and the previously reported normal state Hall coefficient can be correlated via a simple model, strongly suggesting a Fermi surface rearrangement at the critical doping. This is taken as a further evidence for a

quantum phase transition in the electron-doped cuprate superconductors.

Prior vortex Nernst effect measurements have shown a weak superconducting fluctuation effect in electron-doped cuprates, suggesting a more conventional superconductivity. We measured Nernst effect carefully through the entire range of doping and temperature. A stronger superconducting fluctuation effect is observed in the underdoped region compared to the overdoped region. This behavior is similar but weaker than in hole-doped cuprates. We explain this as a result of the incoherent phase fluctuations.

The large normal state Nernst effect observed around optimal doping in electron-doped cuprates has been interpreted as a result of two-carrier transport. Our thorough Nernst effect measurements have revealed a fairly large Nernst signal at the doping extremes (slightly underdoped and highly overdoped) in the normal state, implying that the band structure at these dopings is not a simple one carrier Fermi pocket as suggested by the photoemission experiments.

Hall effect and magnetoresistance measurements in pulsed magnetic field (58 T) were performed on $Pr_{2-x}Ce_xCuO_{4-\delta}$ films. A strong non-linear field dependent Hall resistivity is observed for doping x above optimal doping in a certain temperature range, while the linearity persists up to 58 T in the underdoped region at all measured temperatures. Concomitant with the crossover of field dependent magnetoresistance in the overdoped regime, a spin density wave model is adapted to qualitatively explain the high field Hall effect. These results also imply that a quantum phase transition occurs under the superconductivity dome in electron-doped cuprates.

We also systematically measured the resistive superconducting transition in the electron-doped cuprates $Pr_{2-x}Ce_xCuO_{4-\delta}$ down to 1.5 K for magnetic field up to 58 T applied parallel to the conducting ab-planes. We found that the zero temperature parallel critical field ($H_{c2\|ab}(0)$) exceeds 58 T for the underdoped and optimally-doped films. For the overdoped films, 58 T is sufficient to suppress the superconductivity. We also find that the Zeeman energy $\mu_B H_{c2\|ab}(0)$ reaches the superconducting gap ($\triangle_0$), i.e., $\mu_B H_{c2\|ab}(0) \simeq \triangle_0$, for all the dopings, strongly suggesting that the parallel critical field is determined by the Pauli paramagnetic limit in electron-doped cuprates.

Measurements of Nernst effect, resistivity and Hall angle on epitaxial films of $Y_{1-x}Pr_xBa_2Cu_3O_{7-\delta}$ (Pr-YBCO, $0 \leq x \leq 0.4$) were performed over a broad range of temperature and magnetic field. While the Hall and resistivity data suggest a broad pseudogap regime in accordance with earlier results, these first measurements of the Nernst effect on Pr-YBCO show a large signal above the superconducting transition temperature T_c. This effect is attributed to vortex-like excitations in the phase incoherent condensate existing above T_c. A correlation between disorder and the width of the phase fluctuation regime has been established for the YBCO family of cuprates, which suggests a $T_c \simeq 110$ K for disorder-free $YBa_2Cu_3O_{7-\delta}$.

NOVEL TRANSPORT PROPERTIES OF ELECTRON-DOPED SUPERCONDUCTORS $Pr_{2-x}Ce_xCuO_{4-\delta}$

by

Pengcheng Li

Dissertation submitted to the Faculty of the Graduate School of the
University of Maryland, College Park in partial fulfillment
of the requirements for the degree of
Doctor of Philosophy
2007

Advisory Committee:

Professor Richard L. Greene, Chair/Advisor
Professor Christopher J. Lobb
Professor Robert J. Anderson
Professor Steven M. Anlage
Professor Lourdes Salamanca-Riba

DEDICATION

To my parents and my wife

ACKNOWLEDGMENTS

It has been a long journey for me to reach this point. Many people have taught and helped me during my rounding into a physicist. I acknowledge them all for their invaluable support and encouragement.

First and foremost, I would like to express deep gratitude to my advisor Prof. Rick Greene. Rick saved me from trouble and I am grateful for his compassion and providing me such a great opportunity to work in his well-known group. During the past four years, I have learned a lot from his broad knowledge and expertise on high temperature superconductivity. Rick's being strict on every scientific problems we confronted and his critical view on the physics we dealt with during a manuscript preparation have forced me to study my research precisely. I am indebted to Rick's sacrificing his off-work time to read my manuscripts. His patience on correcting my English and criticizing my physics problems have been crucial for this thesis and the publication of my work. Working under his wings has been a wonderful time in my life, the great research atmosphere of the group he created, his humble character and attractive personality are what made it a joy to be his student. After his four years' advising and training, I hope I have been shaped to be a good student of his.

I am grateful to the collaborators with whom I was lucky to work. Dr. Fedor Balakirev, a great scientist at NHMFL that we collaborated with on the high field experiments, helped me out of many research problems. His expertise on experi-

ments in pulsed magnetic field is indispensable for our productive transport measurements during my stay at Los Alamos. His insightful criticism and comments on my manuscripts were invaluable. The high-field experiments that I worked together with Fedor have ended up as a major part of this thesis. Dr. Ramesh Budhani, our visiting professor from India, proposed us many great research topics. Our collaborating Nernst effect experiments on the high-quality films he supplied also became an important part of my research. Dr. Budhani's great knowledge on superconductivity has broadened my research scope. His quick and crucial revision of my manuscript was essential for its publication. I was also benefited much from the wide knowledge of thermal transport that Dr. Kamran Behnia shares with us. His keen insight of condensed matter physics was very helpful for us to understand and interpret our thermopower measurements. I also would like to thank the fruitful discussions with the great theorists: Drs. Andy Millis, Victor Yakovenko and Andrew Chubukov. It was a great pleasure working with these great scientists, I hope I still have chance to learn from them in the future.

The former and current members in Greene's group were very instrumental to my research. Hamza Balci helped me many times after I joined the group. He was always patient on answering my naive questions, his expertise of the cryogenic equipments and computer automated controlling of electronics were helpful for my successfully constructing the experimental apparatus. Josh Higgins is another graduate student that I owe much for his help. His willing to help at anytime was an lubricant in the smooth progress of my experiments. It was a wonderful period of time working together with him, we have had many good times and I am glad to

have such a good friend around always. Mumtaz Qazilbash, a strict physicist and also a good friend, shared his many understanding of the physics with me. It was a quite pleasure to talk with him frequently. The post-docs in our group, Yoram Dagan, Alexander Zimmers, Weiqiang Yu and Bing Liang, also taught me and helped me on many experimental and physics problems. The fruitful discussions with them were always instructive. I also would like thank Hua Xu and Su Li for their helps on my physics course and experiments.

I would like to thank the graduate students that I met in the superconductivity research center, especially Yuanzhen Chen for his help on the construction of my experimental apparatus, and Dragos Mircea for sharing his thought of research and life with me. I appreciate the great service provided by the center staff, Belta Pollard, Brian Barnaby, Grace Sewlall, Cleopatra White, Brian Straughn, and Doug Bensen. I thank Russell Wood for his suggestions and help on the construction of my apparatus.

To my parents and in-laws, whose support and love have been essential for me to arrive at this point. I am thankful for all they have done for me. Finally, I would like to express my special gratitude to my wife, Yu Shu. Her never complaining of my ignoring her during experiments and her sacrificing of many off-work times being with me in the lab were crucial for my finishing my Ph.D study. I would like to dedicate this thesis to all my family members, especially to my wife.

Table of Contents

Curriculum Vita viii

List of Figures x

1 Introduction 1
- 1.1 Overview of high temperature superconductivity . . . 1
- 1.2 Lattice structure . . . 5
- 1.3 Phase diagram . . . 8
- 1.4 Mott insulator and antiferromagnetic state . . . 10
- 1.5 Electron-doped cuprates: Fermi Surface, Antiferromagnetism and Quantum Phase Transition . . . 15
- 1.6 Motivation and outline . . . 27

2 Review of Transport Theory 31
- 2.1 The Boltzmann equation . . . 31
- 2.2 Electrical conductivity . . . 34
- 2.3 Hall effect . . . 35
- 2.4 Thermoelectric and Nernst effects . . . 38
- 2.5 Two-band (carrier) model . . . 44
  - 2.5.1 Magnetoresistance and Hall effect . . . 45
  - 2.5.2 Thermoelectric power and Nernst effect . . . 47

3 Samples and Experimental Setup 49
- 3.1 Film fabrication and characterization . . . 49
- 3.2 Film patterning . . . 58
- 3.3 Experimental setups . . . 60
  - 3.3.1 Nernst effect measurement . . . 63
  - 3.3.2 Thermoelectric power measurement . . . 67
  - 3.3.3 Resistivity and Hall effect measurements in pulsed magnetic field . . . 73

4 Normal State Thermopower in $Pr_{2-x}Ce_xCuO_{4-\delta}$ 76
- 4.1 Introduction . . . 76
- 4.2 Experiments and results . . . 78
- 4.3 Discussion . . . 82
- 4.4 Conclusion . . . 92

5 High-field Hall Effect and Magnetoresistance in $Pr_{2-x}Ce_xCuO_{4-\delta}$ 93
- 5.1 Introduction . . . 93
  - 5.1.1 Spin density wave model . . . 95
- 5.2 Experiments and results . . . 98
- 5.3 Discussion . . . 103
  - 5.3.1 Two-band model . . . 103

5.3.2 A spin-density wave explanation . . . 106
5.4 Conclusion . . . 110

6 Upper Critical Field of $Pr_{2-x}Ce_xCuO_{4-\delta}$ in Parallel Magnetic Fields 111
6.1 Introduction . . . 111
6.2 Experiments and results . . . 113
6.3 Discussion . . . 118
6.4 Conclusion . . . 123

7 Nernst Effect in $Pr_{2-x}Ce_xCuO_{4-\delta}$ 124
7.1 Nernst effect in type II superconductor . . . 124
7.2 Nernst effect as a probe of superconducting fluctuations . . . 129
7.3 Vortex Nernst effect in $Pr_{2-x}Ce_xCuO_{4-\delta}$ . . . 134
7.3.1 Experiments and results . . . 134
7.3.2 Discussion . . . 138
7.3.3 Conclusion . . . 145
7.4 Normal state Nernst effect in $Pr_{2-x}Ce_xCuO_{4-\delta}$ . . . 146
7.4.1 Introduction . . . 146
7.4.2 Experiments and results . . . 148
7.4.3 Discussion . . . 152
7.4.4 Conclusion . . . 164

8 Nernst Effect in $Y_{1-x}Pr_xBa_2Cu_3O_7$ films 165
8.1 Introduction . . . 165
8.2 Experiments and results . . . 166
8.3 Discussion . . . 173
8.4 Conclusion . . . 178

9 Summary and Future Research 179
9.1 Summary of thermotransport of $Pr_{2-x}Ce_xCuO_{4-\delta}$ . . . 179
9.2 Summary of high-field transport of $Pr_{2-x}Ce_xCuO_{4-\delta}$ . . . 181
9.3 Summary of Nernst effect of $Y_{1-x}Pr_xBa_2Cu_3O_{7-\delta}$ . . . 183
9.4 Future research . . . 183

Bibliography 187

Curriculum Vita

Education

Ph.D. Physics, University of Maryland, 2007.

M.S. Physics, University of Science and Technology of China, 2002.

B.S. Physics, University of Science and Technology of China, 2000.

B.S. Management Science, University of Science and Technology of China, 2000.

Publications (during Ph.D period)

Pengcheng Li, F. F. Balakirev and R. L. Greene, *High field Hall resistivity and magnetoresistance of electron-doped* $Pr_{2-x}Ce_xCuO_{4-\delta}$, Physical Review Letters, **99**, 047003 (2007).

Pengcheng Li, F. F. Balakirev and R. L. Greene, *Upper critical field in electron-doped* $Pr_{2-x}Ce_xCuO_{4-\delta}$ *in parallel magnetic field*, Physical Review B **75**, 172508 (2007).

Pengcheng Li, S. Mandal, R. C. Budhani and R. L. Greene, *Correlation between incoherent phase fluctuations and disorder on* $Y_{1-x}Pr_xBa_2Cu_3O_{7-\delta}$ *epitaxial films from Nernst effect measurements*, Physical Review B **75**, 184509 (2007).

Pengcheng Li, K. Behnia and R. L. Greene, *Evidence for a quantum phase transition in electron-doped* $Pr_{2-x}Ce_xCuO_{4-\delta}$ *from thermopower measurements*, Physical Review B Rapid Communication, **75**, 020506 (2007).

W. Yu, B. Liang, **P. Li**, S. Fujino, T. Murakami, I. Takeuchi and R. L. Greene, *Oxygen-doped Mott-Hubbard cuprate superconductor* $La_{1.85}Y_{0.15}CuO_{4-\delta}$ *from trans-*

port measurements, Physical Review B Rapid Communication, 75, 020503 (2007).

Pengcheng Li and R. L. Greene, *Normal State Nernst effect in electron-doped* $Pr_{2-x}Ce_xCuO_{4-\delta}$*: superconducting fluctuations and two-band transport*, submitted to Phys. Rev. B (2007).

V. M. Yakovenko, **Pengcheng Li**, *Thermopower and the Wiedemann-Franz law in the presence of the fermion condensate*, in preparation.

List of Figures

1.1 Schematic for the lattice structures for the layered cuprates 6

1.2 Generic phase diagram of the cuprates 8

1.3 Electronic structure of the undoped cuprates 12

1.4 Magnetic structure of the undoped cuprates 13

1.5 Normal state Hall coefficient of $Pr_{2-x}Ce_xCuO_{4-\delta}$ films 16

1.6 Fermi surface and ARPES of $Nd_{2-x}Ce_xCuO_{4-\delta}$ 18

1.7 Antiferromagnetic phase transition in electron-doped cuprates 20

1.8 Quantum criticality in high-T_c superconductors 21

1.9 Temperature dependence of the in-plane resistivity of $Pr_{2-x}Ce_xCuO_{4-\delta}$ films in zero field and H=10 T 23

1.10 A phase diagram of electron-doped cuprates from normal state resistivity measurement 24

1.11 Doping dependence of a normal state gap in electron-doped cuprates from optical conductivity 25

2.1 Schematic diagram of thermoelectric and Nernst effects 39

3.1 Schematic of a PLD chamber 52

3.2 A typical AC susceptibility of a PCCO film 53

3.3 Doping dependence of the residual resistivity of PCCO films 54

3.4 X-ray diffraction pattern for $Pr_{1.83}Ce_{0.17}CuO_{4-\delta}$ 56

3.5 Doping dependence of the c-axis lattice parameter of $Pr_{2-x}Ce_xCuO_4$ films 57

3.6 Hall bar pattern for the high-field experiments 59

3.7 Schematics of a cryostat and a home-made probe 62

3.8 A schematic of a sample stage for the Nernst effect measurement . . . 63

3.9 Nernst effect measurement procedure 65

3.10 Nernst signal of a Pr-doped YBCO film 66

3.11 A schematic of the thermopower measurement 68

3.12 Program flow chart of the one-heater-two-thermometer thermopower and Nernst effect measurements in a temperature sweeping method . 70

3.13 A schematic of a sample stage for the thermopower measurement . . 71

3.14 Program flow chart of the two-heater-two-thermometer thermopower measurement 72

3.15 A pulsed magnetic field curve 74

4.1 Temperature dependence of the zero field thermopower in PCCO . . 79

4.2 Temperature dependence of the normal state thermopower in PCCO 81

4.3 Normal state S/T versus T and S/T (T=2 K) versus x in PCCO . . . 83

4.4 Normalized S/T and $\sigma(T)$ for x=0.11 versus T for T$\leq$40 K 86

4.5 Doping dependence of q and q' of PCCO at T= 2 K 89

5.1 Fermi surfaces calculated from a tight-binding SDW model 96

5.2 Field dependence of the Hall resistivity for underdoped PCCO films with x=0.11 and 0.13 99

5.3 Hall resistivity versus field for the PCCO films with x=0.15, 0.16, 0.17 and 0.19 101

5.4 Magnetoresistance of the PCCO films with x=0.13, 0.15 and 0.17 . . 102

5.5 A two-band fitting of the Hall resistivity and magnetoreistance for an overdoped x=0.17 PCCO film 105

5.6 A two-band fitting of the Hall resistivity in an optimally-doped x=0.15 PCCO film 106

5.7 A phase diagram for elecctron-doped cuprates 109

6.1 Temperature dependence of the in-plane resistivity of PCCO films at H= 0 T and 58 T 114

6.2 In plane resistivity versus magnetic field for H‖ab-plane in PCCO films 116

6.3 Temperature dependence of the parallel upper critical field in PCCO 117

6.4 Zero temperature parallel upper critical field as a function of doping and the superconducting gap 119

7.1 Vortex structure and Nernst effect in type II superconductor 125

7.2 Vortex Nernst effect in a conventional superconductor PbIn 128

7.3 Nernst effect in hole-doped $La_{2-x}Sr_xCuO_4$ 131

7.4 Nernst effect in an optimally-doped x=0.15 PCCO film 135

7.5 Vortex Nernst effect in an underdoped x=0.13 PCCO film 137

7.6 A phase diagram for PCCO from vortex Nernst effect measurement . 139

7.7 Off-diagonal Peltier conductivity α_{xy} of an underdoped PCCO film x=0.13 at H=1 T 140

7.8 Paraconductivity of the underdoped and optimally-doped PCCO films 144

7.9 Nernst effect of an underdoped PCCO x=0.13 at H= 2 T 149

7.10 Normal state Nernst effect in PCCO films 150

7.11 Temperature dependence of the Hall angle $tan\theta_H$ of PCCO films . . . 151

7.12 Temperature dependence of $cot\theta(T)$ of the underdoped and optimally-doped PCCO films . . . 154

7.13 Doping dependence of magnetoresistance in PCCO at 50 K . . . 159

7.14 Temperature dependence of $Stan\theta_H$ of PCCO films . . . 161

8.1 Temperature dependence of the in-plan resistivity of the $Y_{1-x}Pr_xBa_2Cu_3O_{7-\delta}$ films . . . 168

8.2 Hall angle of the $Y_{1-x}Pr_xBa_2Cu_3O_{7-\delta}$ films . . . 171

8.3 Field dependence of the Nernst signal in a $Y_{1-x}Pr_xBa_2Cu_3O_{7-\delta}$ film . 172

8.4 Temperature dependence of the Nernst signal at H=14 T for the $Y_{1-x}Pr_xBa_2Cu_3O_{7-\delta}$ films . . . 174

8.5 Doping dependence of the temperature scales deduced from the in-plane resistivity, Hall angle and Nernst effect in the $Y_{1-x}Pr_xBa_2Cu_3O_{7-\delta}$ films . . . 175

8.6 Onset temperature T_ν of the anomalous Nernst signal versus T_c for the oxygen-doped and disordered YBCO . . . 177

Chapter 1

Introduction

1.1 Overview of high temperature superconductivity

In 1908, H. Kamerlingh Onnes started the field of low-temperature physics by liquifying helium at Leiden. In 1911, he found that below 4.15 K the dc resistivity of Hg dropped to zero [1]. With that discovery, the field of superconductivity was born. Onnes later discovered that the application of a sufficient magnetic field restored the resistance to its normal state. Since then, superconductivity has been found in many metallic elements of the periodic table, alloys and intermetallic compounds.

A considerable amount of time passed before physicists became aware of the second distinguishing characteristic of a superconductor, namely, its perfect diamagnetism. In 1933 Meissner found that when a sphere was cooled below its transition temperature (T_c) in a magnetic field, it excluded the magnetic flux [2]. The report of the Meissner effect stimulated the London brothers to propose their equations [3], which explained the Meissner effect and predicted a penetration depth for how far a static external magnetic flux can penetrate into a superconductor. The next theoretical advance came in 1950 with the theory of Landau and Ginzburg [4], which described superconductivity in terms of an order parameter and provided a derivation for the London equation. Both of these theories were macroscopic in character.

In 1951, the isotope effect, whereby the transition temperature decreases when

the average isotopic mass increases, was predicted theoretically by H. Frohlich [5] and discovered experimentally by E. Maxwell [6]. This effect provided support for the importance of the electron-phonon interaction, i.e.,"phonon mediated" superconductivity. In 1957, about four decades after the monumental discovery of superconductivity, a microscopic theory of superconductivity was introduced by Bardeen, Cooper and Schrieffer (BCS) [7]. This theory involves the formation of bound electron pairs that carry the supercurrent, and an energy gap that stabilizes the superconductivity. The Landau-Ginzburg and London results fit well into the BCS formalism. Many predictions of BCS theory were proven correct by subsequent experiments.

For many years after the birth of BCS theory, it was believed that the superconducting transition temperature (T_c) could not exceed an upper limit of 30-40 K. Until 1986, a T_c of 23.4 K observed in Nb_3Ge was the highest known. In 1986, George Bednorz and Karl Alex Müller [8] made the remarkable discovery of superconductivity at T_c=35 K in a ceramic copper oxide, a discovery that brought a new class of solids to the world of superconductor physics and materials science. The new superconducting material was La_2CuO_4, in which the ions of Ba^{2+}, Sr^{2+} or Ca^{2+} were doped to partially replace La^{3+} ions and hole-carriers are introduced. This discovery was the dawn of the era of high temperature superconductivity (HTSC). Soon after this discovery, T_c was raised to 90 K (above the boiling point of liquid N_2) by synthesizing $YBa_2Cu_3O_{7-\delta}$ with a deficit in oxygen [9, 10]. Further exploration for new copper oxide superconuducting materials with higher T_c led to the discovery of Bi-Sr-Ca-Cu-O [11], Tl-Ba-Cu-O [12] and Hg-Ba-Ca-Cu-O [13] compounds

in subsequent years. This new class of copper oxide superconducting compounds is called "cuprates". At present, T_c=135 K under ambient pressure and T_c=164 K under 30 GPa observed in $HgBa_2Ca_2Cu_3O_8$ are the highest T_c values obtained [14]. In 1989, Tokura *et al.* [15] discovered the electron-doped cuprates $RE_{2-x}Ce_xCuO_{4-\delta}$ (RE=Sm, Nd, Pr, La). The electron-doped cuprates have a relatively modest maximum T_c of about 25 K.

The cuprate superconductors are characterized by their high critical temperatures and the common feature of their layered perovskite-like structures, consisting of parallel CuO_2 planes (see Structure section). It is believed that mobile charge carriers reside on the CuO_2 planes only, and they are responsible for the superconductivity. The superconductivity is achieved by doping holes or electrons into the CuO_2 planes of the insulating antiferromagnetic parent compounds. Due to the layered structure, the cuprate superconductors are highly anisotropic. The *ab*-plane (CuO_2 plane) and the *c*-axis properties are significantly different and thus these cuprates are regarded as quasi-two-dimensional (2D) systems.

Cuprate superconductors have shown many anomalous properties in both the superconducting and normal states. In the normal state, electrons are strongly correlated and many abnormal transport behaviors are observed, such as a linear temperature dependence of the resistivity observed in hole-doped cuprates [16], the temperature dependence of the Hall coefficient R_H [16], and the peculiar behavior of the infrared conductivity [17]. The small magnitude of the mean free path of charge carriers strongly suggests that some form of electron-electron scattering is dominant in the normal state high-T_c cuprates [18]. The superconducting properties of high-T_c

cuprates are also significantly different from those of the conventional BCS-type superconductors. The most dramatic difference is that the gap parameter in cuprates is strongly anisotropic and has a d-wave symmetry with gapless nodes along the (π, π) direction in the momentum space (see Ref. [19]). The unconventional d-wave pairing in hole-doped cuprates has been supported by extensive experiments (see review [20]) and is well accepted. The symmetry of the superconducting order parameter is still somewhat controversial in electron-doped cuprate superconductors. Early penetration depth measurements [21] and point contact tunnelling [22] showed the behavior expected for s-wave pairing, but more recent penetration depth measurements have found a power law temperature dependence consistent with a disordered d-wave state [23]. Recent angle resolved photoemission spectroscopy (ARPES) measurements are also consistent with d-wave symmetry [24, 25], but these experiments are near the resolution limit because of the small energy gap. Tri-crystal experiments find a half integral flux quantum in certain geometries as predicted by d-wave symmetry [26]. A d-wave symmetry was also found in recent Raman experiments [27]. Based on these recent developments, it is most likely that the pairing symmetry is d-wave in electron-doped cuprates. The d-wave symmetry in cuprate superconductors implies that the electron-phonon interaction is probably not the cause of the superconductivity and the pairing mechanism is most likely electronic or magnetic in origin.

Because of its application potential and fundamental interest, high-T_c superconductivity became an actively pursued field. With the advances in crystal chemistry and experimental techniques over the last two decades, a wealth of knowledge

has been obtained about these cuprate superconductors. Despite the intense research, however, a valid theory for high temperature superconductivity remains elusive. There is much evidence that in cuprates, unconventional superconductivity can not be reconciled with the phonon-mediated BCS theory. Moreover, the normal state properties are quite anomalous and cannot be simply explained by conventional Fermi liquid theory. Many theoretical models, such as resonant valence bond (RVB) model, $t-J$ model, marginal Fermi liquid model *etc.* have been proposed (see M. Norman [28] for a review). With limited success in explaining all the experiments, none of them has provided a generic picture for the mechanism of high temperature superconductivity. In this thesis, the goal is to study the transport properties of some high-T_c cuprates and provide useful information for the ultimate understanding of the mechanism of high-T_c superconductivity.

1.2 Lattice structure

The unit cell of the cuprate superconductors is predominantly a tetragonal layered perovskite structure with one or more CuO_2 layers. The superconductivity is believed to be associated with these planes. The layered structure of cuprates can be regarded as a conducting CuO_2 plane sandwiched by two insulating layers consisting of oxygen and the rare earth ions. These insulating layers are the so called charge carrier reservoir or charge buffer layer and superconductivity depends on the charge transferred from the reservoir layers to the conducting CuO_2 planes. Fig. 1.1(a) and (b) show the structures of some typical one layer cuprate superconductors, hole-

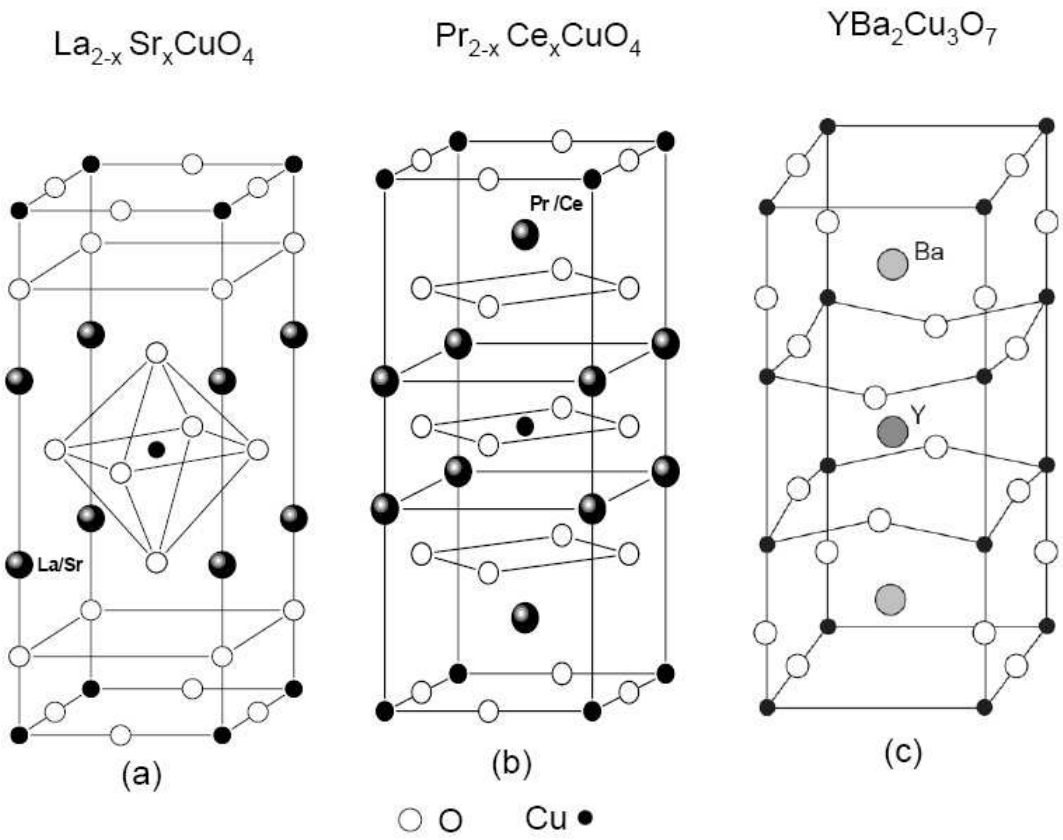

Figure 1.1: Schematic for the lattice structures for a few cuprates. (a) single layer T structure in which the Copper and Oxygen form a CuO_6 octahedra. (b) single layer T′ structure in which the Copper and Oxygen form a CuO_2 plane. (c) Double layer crystal structure of $YBa_2Cu_3O_7$.

doped $La_{2-x}Sr_xCuO_4$ (LSCO) and electron-doped $Pr_{2-x}Ce_xCuO_{4-\delta}$ (PCCO). By substituting Sr/Ce ions into La/Pr site of the parent compound La_2CuO_4/Pr_2CuO_4, extra holes/electrons will transfer into the CuO_2 planes and become charge carriers. $La_{2-x}Sr_xCuO_4$ has a tetragonal structure with the lattice parameters a=3.779 Å and c=13.226 Å. The space group is $I4/mmm$ and the locations of the atoms are: La(Sr) (0 0 0.36046); Cu (0 0 0); O(1)(planar site)(0 0.5 0); O(2)(reservoir site) (0 0 0.1824) [29]. This structure is called a T-type phase and it consists of a CuO_6 octahedral where oxygen sits directly above and below the copper sites. The electron-doped cuprate $Pr_{2-x}Ce_xCuO_{4\pm\delta}$ also has tetragonal structure and belongs to the $I4/mmm$ space group. The lattice parameters a=3.95 Å and c=12.07 Å (x=0.15). The location of the atoms are Pr(Ce) (0 0 0.3513), Cu (0 0 0), O(1) (0 0.5 0), O(2) (0 0.5 0.25) [30]. In respect to the T phase, the structure of electron-doped compound is called the T′ phase. In contrast, the T′ phase consists of squares of copper and oxygen, each successive CuO_2 plane is rotated 45^0 with respect to each other. The oxygen sites are all arranged along a line in the c direction throughout the unit cell.

The crystal structure of $YBa_2Cu_3O_7$ (YBCO) is shown in Fig. 1.1(c). The unit cell is orthorhombic with a Pmmm space group. The lattice dimensions are a=3.83 Å, b=3.88 Å, and c=11.68 Å. The locations of the atoms are Ba(0.5 0.5 0.1851); Y(0.5 0.5 0.5); Cu(1)(0 0 0); Cu(2)(0 0 0.3554); O(1)(0 0 0.159); O(2)(0.5 0 0.3767); O(3)(0 0.5 0.3782); O(4)(0 0.5 0) [31]. The CuO_2 superconducting layers are formed by Cu(2), O(2) and O(3) atoms. Along the b-axis, Cu(1) and O(1) atoms form a Cu-O-Cu chain. In the parent compound $YBa_2Cu_3O_6$, the O(1) atoms are

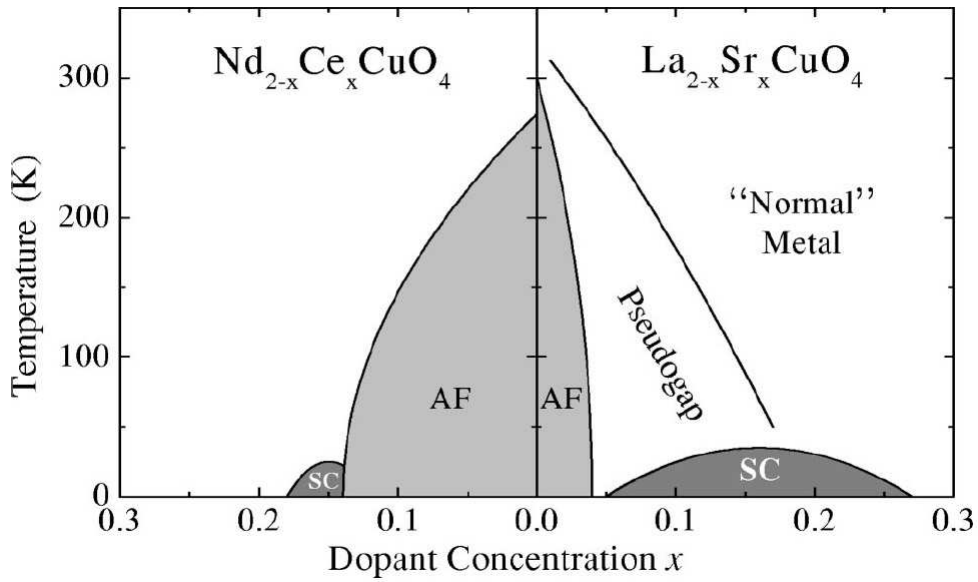

Figure 1.2: Phase diagram of electron- and hole-doped superconductors, showing superconductivity (SC), antiferromagnetic (AF), pseudogap, and normal-metal regions(adapted from Ref. [19]).

absent. Oxygen atoms are introduced onto the O(1) sites by doping. It is believed that holes are generated by oxygen on the O(1) sites, and then transferred onto the CuO_2 planes.

1.3 Phase diagram

All high T_c superconductors are obtained by doping the antiferromagnetic insulating parent compounds with holes and electrons [28]. The occurrence of an insulator-metal transition and a metal-superconductor transition appears to be a universal behavior as a function of both electron and hole doping. A general phase diagram for cuprate superconductors is shown in Fig. 1.2. On the hole-doped side,

e.g. $La_{2-x}Sr_xCuO_4$, the parent compound, La_2CuO_4, is an antiferromagnetic insulator with a Neel temperature (T_N) of 300 K. Holes are introduced into the copper oxide planes by partly replacing La^{3+} with Sr^{2+}. The antiferromagnetism (AFM) is suppressed at about 0.02 extra holes per copper atom and the material enters a spin-glass phase. With more doping with Sr^{2+}, superconductivity (SC) appears at x=0.06. Further doping increases carrier concentration and T_c with the maximum T_c obtained at x=0.15. The T_c drops with further doping and superconductivity disappears at x=0.3. The doping dependence of superconductivity has a dome-like shape and other hole-doped cuprate superconductors have a similar phase diagram.

In the phase diagram of the hole-doped cuprates, there is another important but less well understood phase: the pseudogap phase, as shown in Fig. 1.2. Upon cooling, an energy gap opens below a characteristic temperature T^*, the pseudogap temperature. Many experiments, such as ARPES, scanning tunneling microscope (STM), specific heat and NMR have revealed the opening of an energy gap in the normal state (for a review, see [32]). The nature of the pseudogap phase and its relation to the superconducting state is one of the central issues of high-T_c superconductivity research, whether it is precusor of superconductivity (pre-formed Cooper pairs or phase fluctuations) [33] or a competing order parameter (e.g. charge density wave) [34] is still under debate.

The phase diagram of the electron-doped cuprates superconductor is qualitatively similar but quantitatively different from their hole-doped counterpart. The parent compound RE_2CuO_4 (RE = Nd, Pr) is also an antiferromagnetic insulator (with a T_N of 255 K [35]). The doping of Ce^{4+} introduces electrons in the copper ox-

ide planes. In contrast to the hole-doped, antiferromagnetism persists up to a much higher doping, close to or into the superconductivity dome. Superconductivity suddenly appears when the doping is increased beyond x=0.13 and the maximum T_c occurs at x=0.15. Superconductivity vanishes for dopings above x=0.2. In general, the doping range is larger for the antiferromagnetic phase and smaller for the superconducting phase in the electron-doped cuprates compared to the corresponding doping ranges in the hole-doped. Two issues should be mentioned for the electron-doped cuprates. First, whether or not a pseudogap phase exists is under debate. Secondly, the exact doping where the long-range antiferromagnetic phase vanishes is controversial and whether the AFM phase coexists with superconductivity remains unclear [36, 37, 38]. In this thesis, we use transport measurements to attempt to clarify these important issues.

1.4 Mott insulator and antiferromagnetic state

In the parent compounds of cuprate superconductors, all copper ions in the CuO_2 planes are in the $3d^9$ (Cu^{2+}) state and there is exactly one unpaired electron per Cu site. This corresponds to a single hole in the $d_{x^2-y^2}$ orbital. Of all transition metal oxides, the cuprates are unusual in that the copper d orbital and the oxygen p orbital have energies that are nearly degenerate (Fig. 1.3) [39]. As a consequence, the dominant energy scale in the problem is the large ($\sim$6 eV) bonding-antibonding splitting between the copper $d_{x^2-y^2}$ orbital and the oxygen p_x and p_y orbitals. This leaves the highest energy band (the antibonding band) as half filled and thus the

system should be metallic. However, strong on-site Coulomb repulsion (Hubbard U) between the electrons makes double occupancy energetically unfavorable and this band splits into two, a lower Hubbard band (LHB) and an upper Hubbard band (UHB). Therefore, electron-hopping to the neighboring copper site is strongly prohibited and results in the so called Mott-Hubbard insulating state with a gap of order several eV [19]. Finite conductivity appears when extra charges are introduced into the Mott insulator. In the case of hole-doped cuprates, a small number of holes in the CuO_2 planes provide vacancies for electron hopping and metallic conductivity is restored. This doped Mott insulator retains features of the strong correlation effects in the parent compound and usually exhibits exotic physical properties.

Strong Coulomb repulsion leads to a localized electron and therefore a 1/2 spin moment on the Cu site. The superexchange interaction generated by virtual charge fluctuations between neighboring copper sites results in an antiferromagnetic correlation. The interaction strength in the CuO_2 planes is much stronger than that between the adjacent layers, indicating a two-dimensional antiferromagnetic correlation. The static 2D commensurate antiferromagmetic structure of the CuO_2 plane is shown in Fig. 1.4.

The strong on-site Coulomb interaction and antiferromagnetic interaction (J) in the parent compound of cuprates play essential roles in many proposed theories of high-T_c superconductivity. Considering all the three bands (one band from each of the three states, Cu $3d_{x^2-y^2}$, O $2p_x$, and O $2p_y$) is known as the three band Hubbard model [42, 43], while keeping just the antibonding band is known as the single band Hubbard model [44]. In these theories, the first consideration is that

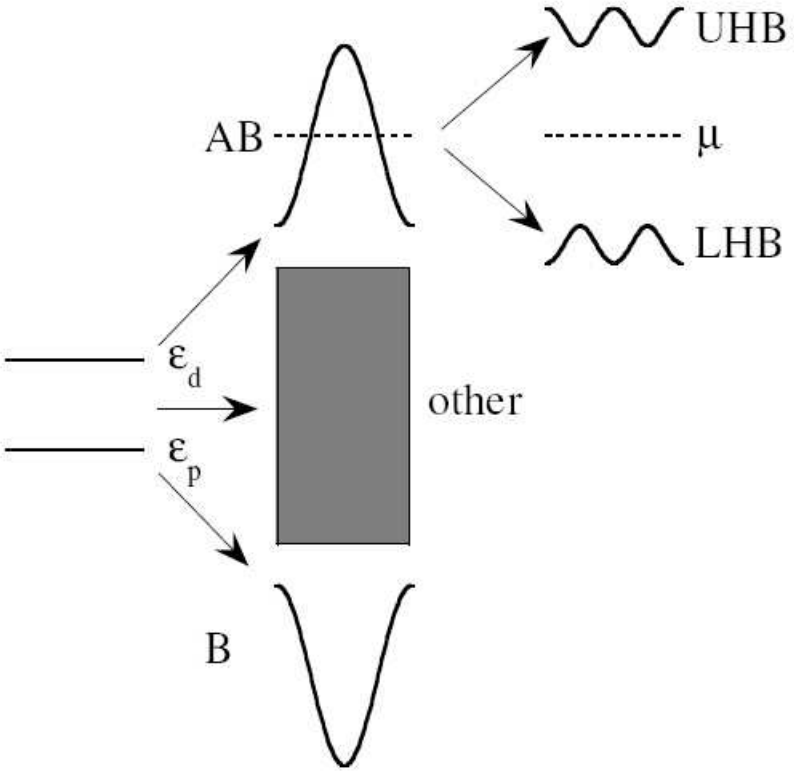

Figure 1.3: Sehematic Electronic structure of the undoped cuprates. Left panel shows the atomic Cu d and O p levels, middle panel the band structure of the solid (where B is the bonding combination of the atomic levels, AB the antibonding one), and right panel the effect of correlations (Mott-Hubbard gap) on the AB band (LHB and UHB are the lower and upper Hubbard bands [28]).

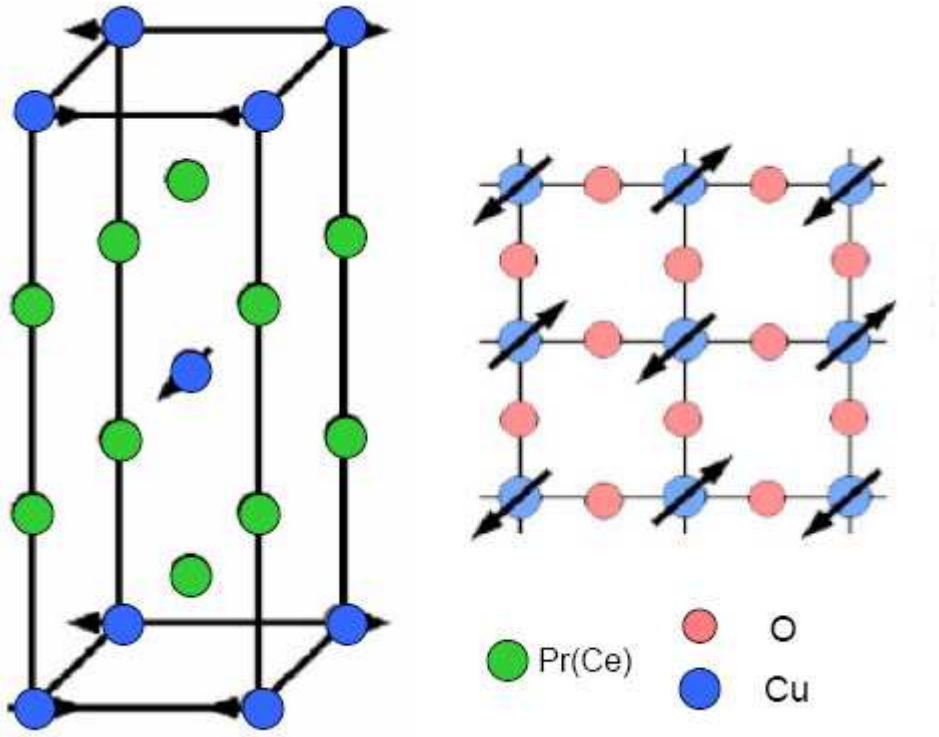

Figure 1.4: Left panel: Schematic diagram of the noncollinear spin structure of electron-doped cuprates [40]. Right panel: Alignment of the Copper spins in the antiferromagnetic state of the cuprates [41]. This is a representation of the xy plane. The Copper spins are aligned along the 45° line of the CuO_2 squares.

the important physics is occurring in the CuO_2 plane. The reason is that the bands closest to the Fermi energy (as determined by band calculations) are due to the in-plane hybridization of the copper and oxygen orbitals. The three band model incorporates all of the hybridized bands, and a competition between on-site coulomb repulsion and a hopping component between nearest neighbors. In this picture (charge-transfer scheme) doped holes enter into the oxygen p orbital, whereas doped electrons enter into the upper Hubbard band. Therefore, doped holes reside mostly on the oxygen sites and doped electrons are mostly on the copper sites. In the one band model, the holes doped onto the oxygen sites are assumed to form singlet pairs (Zhang-Rice singlets [44]) with the lone $3d^9$ hole that already resides on the copper site. Without loss of generality, one can consider the singlet state to be centered on the copper site. In this model, the copper sites are primarily considered, the oxygen bands much less so, and there is only an upper Hubbard band and a lower Hubbard band, energetically separated by an effective repulsive gap U_{eff}. Similar to the three band model, there is a competition between U_{eff} and t (t is the effective hopping integral between Cu sites). As in the three band model, electrons are doped onto the copper site, whereas doped holes are now shared between the copper and oxygen sites. In the limit of large Coulomb repulsion, U, one can then project onto the subspace which does not allow double occupation of the Cu site, leading to the $t-J$ model, where J, the superexchange interaction, is proportional to t^2/U. J prefers antiferromagnetic orientation of the copper spins. This can be seen by the fact that the Pauli exclusion principle does not allow virtual double occupation unless the two spins are anti-aligned.

1.5 Electron-doped cuprates: Fermi Surface, Antiferromagnetism and Quantum Phase Transition

Electron-doped (n-type) cuprate superconductors $RE_{2-x}Ce_xCuO_{4-\delta}$ (RE=Nd, Pr, Sm) have been studied actively since their discovery [15]. Numerous experiments have shown that the electron-doped cuprates exhibit many similarities with their hole-doped (p-type) high-T_c counterparts. Thus, any eventual explanation of high temperature superconductivity would have to treat both sides of the doping diagram in the similar manner. Some of the key phenomena realized in both types of high-T_c compounds, such as the anomalous temperature dependence of the transport coefficients, pose challenging questions for condensed matter physics. Therefore, it is very important to investigate electron-doped cuprates, which could provide useful information for understanding the mechanism of high-T_c superconductivity. The study of some novel transport properties of electron-doped cuprates is the main focus of this thesis.

Besides the similarities, electron-doped cuprates also demonstrate many distinct properties with respect to the hole-doped cuprates. One of the most prominent of these distinctions is two-band transport in the electron-doped cuprates. Prior transport measurements on n-type cuprates [45, 46, 47, 48], such as Hall effect (see Fig. 1.5 from Ref. [49]) and thermoelectric power, have shown a sign change with temperature and doping. The Hall coefficient and thermopower are negative for doping below optimally-doped (Ce $\leq$ 0.15) throughout the whole temperature range. However, in the overdoped region (Ce $>$ 0.15), they are negative at high tempera-

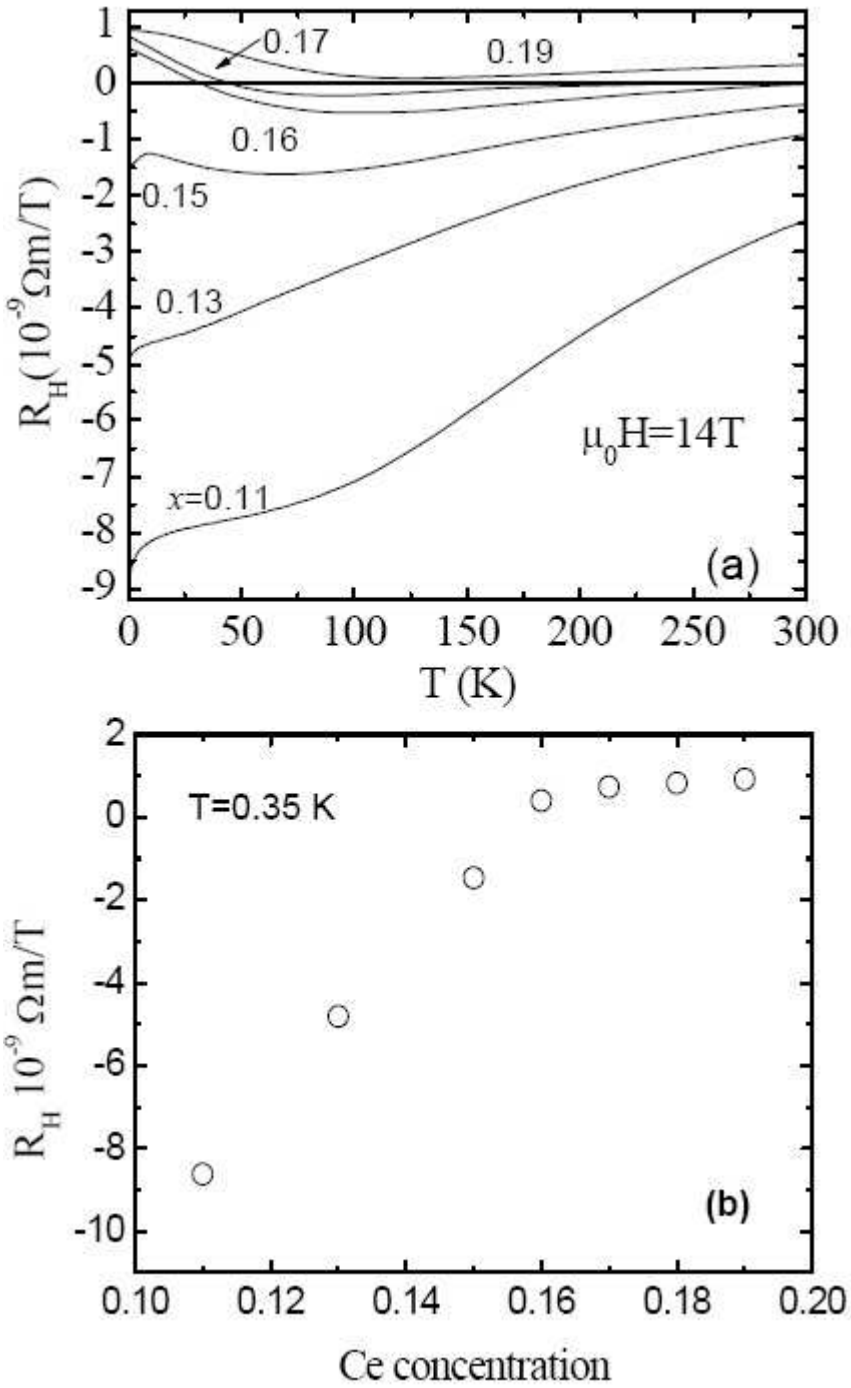

Figure 1.5: Normal state Hall coefficient of $Pr_{2-x}Ce_xCuO_{4-\delta}$ films ($H>H_{c2}$). Upper panel shows the temperature dependence of Hall coefficient for various dopings. The lower panel shows the doping dependence of the Hall coefficient at T=0.35 K [49].

ture and become positive at low temperature. The sign change of these coefficients, which are sensitive to the sign of carriers, implies that there are two electronic subsystems (i.e., hole and electron bands) coexisting and competing in this material around optimal doping. In addition, the doping dependence of the Hall coefficient at T$\sim$0 shows a kink at a doping slightly above the optimal doping [49]. This sharp change of the Hall coefficient suggests a Fermi surface rearrangement at this doping.

The two-band transport in the electron-doped cuprates has been a long-standing puzzle and it remained unsolved until a systematic study of the electronic structure at various doping was carried out. The development of ARPES along with the improvement of the quality of the single crystals have made the mapping the Fermi surface of electron-doped cuprates feasible. Typically, the cuprate superconductors have cylindrical Fermi surfaces because of their two-dimensional character. Recent ARPES measurements have revealed the Fermi surfaces evolution for electron-doped cuprates [50, 51]. The Fermi surface for $Nd_{2-x}Ce_xCuO_4$ (NCCO) with various doping is shown in Fig. 1.6. At low dopings, small electron pockets are seen at the $(\pi, 0)$ and $(0, \pi)$ portions of the Brillouin zone [Fig. 1.6(a)]. The carrier density that estimated from area of the 2D Fermi pockets at low doping are comparable to the doping level ($\simeq x$). As the doping increases to $x = 0.10$ [Fig. 1.6(b)], quasi-particle states at the Fermi energy can be seen to emerge at the $(\pi/2, \pi/2)$ region of the Brillouin zone. On increasing doping to the optimally-doped $x = 0.15$ [Fig. 1.6(c)], a well-defined hole pocket is observable at the $(\pi/2, \pi/2)$ region with an electron-like pocket near $(\pi, 0)$and $(0, \pi)$. In the figure, a theoretical Fermi surface within the tight-binding model is also shown for comparison, and the experimental con-

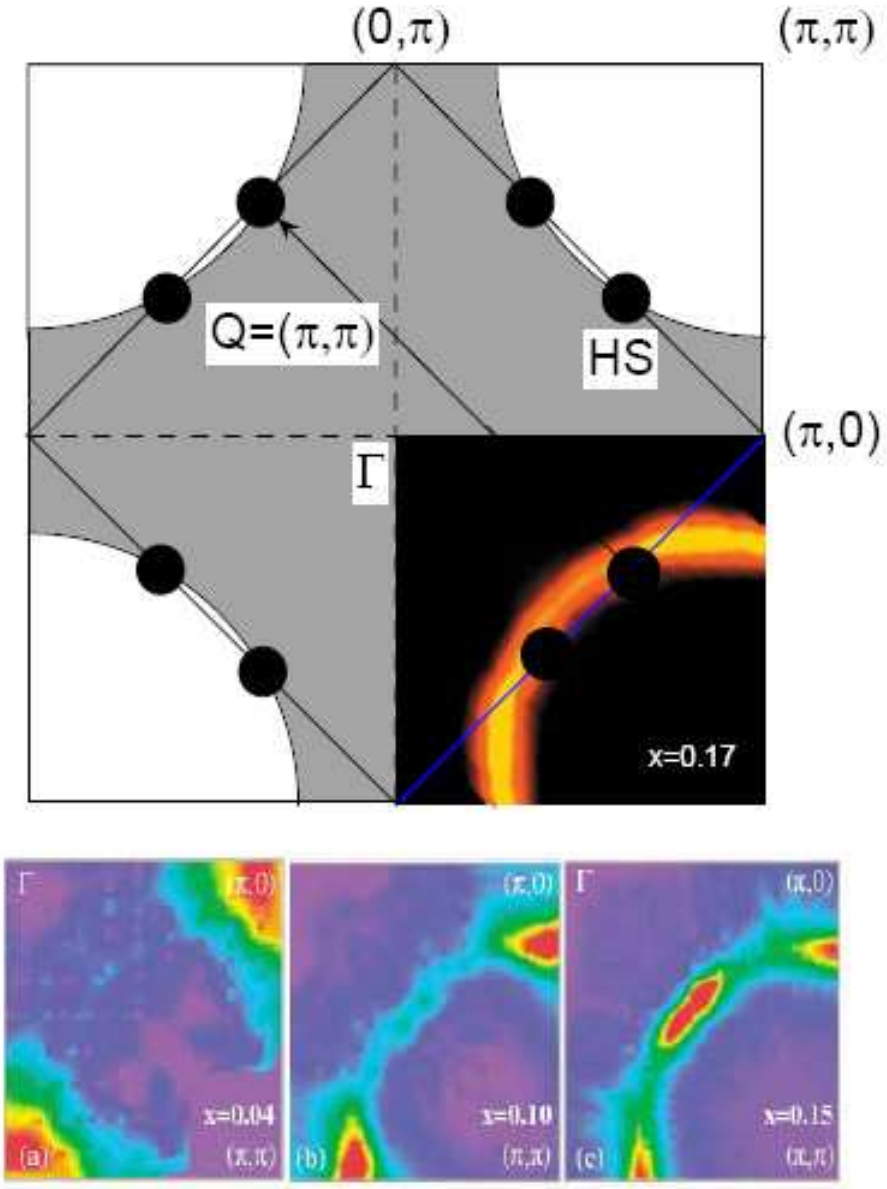

Figure 1.6: Fermi surface of electron-doped $Nd_{2-x}Ce_xCuO_{4-\delta}$ for (a) $x = 0.04$, (b) $x = 0.10$, and (c) $x = 0.15$ at T = 15 K from Ref. [50]. Top panel shows the theoretically calculated Fermi surface along with the experimental data for $x = 0.17$ [53]. Shaded region in top panel is filled by electrons. Colors in bottom panel are explained in text.

tour appears to be consistent with this simple theory. The red regions in Fig. 1.6 describe a Fermi surface with well-defined quasi-particles. The green areas between the red areas are regions where the Fermi surface is not well-defined. These regions are known as "hot spots" which occur at the intersection of the Fermi surface and the diamond-shaped antiferromagnetic Brillouin zone. We mention that the "hot spots" are regions on the Fermi surface which are separated by the antiferromagnetic wave vector $Q{=}(\pi,\pi)$ and where the antiferromagnetic interactions between quasi-particles are enhanced. Among the numerous theories of superconductivity, the one that describes pairing of the electrons via antiferromagnetic spin fluctuations has been given serious consideration [52]. This is because it predicts a directional dependence in the electronic properties of the cuprates: in particular, it predicts the $d_{x^2-y^2}$ superconducting gap symmetry that has been observed in most of the cuprates. Also, the proximity of the superconducting phase to the antiferromagnetic phase makes it a natural candidate for explaining the origin of superconductivity, since it supposes that spin fluctuations persist even after the long-range antiferromagnetic order is destroyed.

The doping evolution of Fermi surface from an electron-like pocket in the underdoped region to coexisting hole-like and electron-like pockets at optimal doping has provided a good qualitative explanation for the transport properties. From this evolution, one expects that in the overdoped region, the Fermi surface would become a large hole-like pocket centered at (π,π). In fact, recent ARPES measurements found a large single hole-like pocket in overdoped $Nd_{1.83}Ce_{0.17}CuO_4$ [53], as seen in Fig. 1.6. This strongly suggests that the Fermi surface is dramatically changing

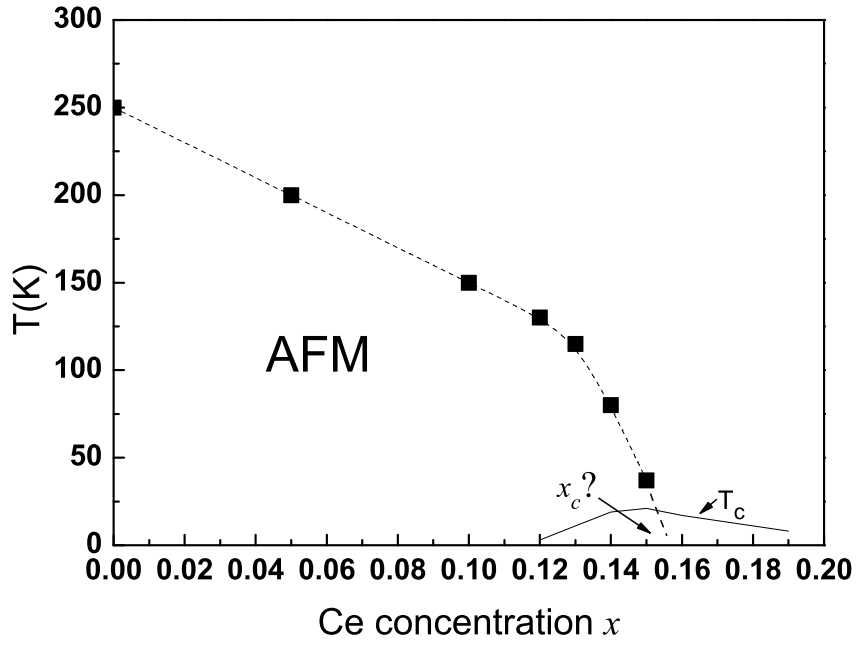

Figure 1.7: A magnetic phase diagram for electron-doped cuprates. Black squares are the antiferromagnetic (AFM) transition temperatures from Ref. [35, 37]. The solid line is T_c.

between 0.15 and 0.17 and a boundary between electron-like material and hole-like material is found in this critical doping range.

Another distinct property of electron-doped cuprates is the broad antiferromagnetic phase which extends near or into the superconductivity dome [36, 37]. The possible competition between antiferromagnetism and superconductivity has been an important but controversial issue [38]. As found in previous neutron scattering and μSR measurements [35, 36, 37], with increasing Ce doping the antiferromagnetism decreases and vanishes. The doping evolution of antiferromagnetism suggests

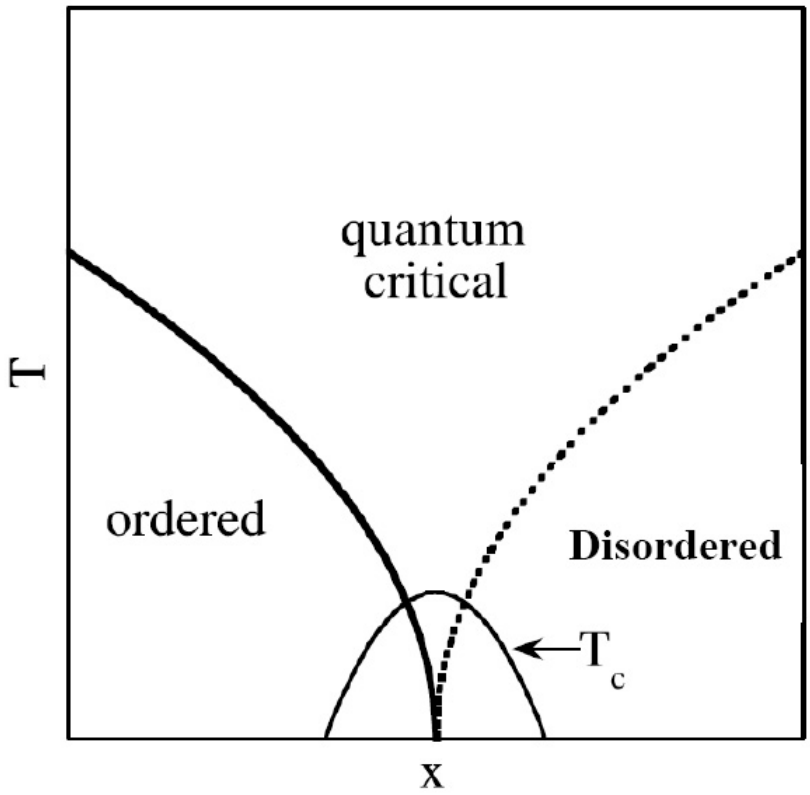

Figure 1.8: A quantum phase transition picture for high-T_c superconductors. In this picture, the ordered phase (to the left of the critical point) would correspond to the antiferromagnetic or pseudogap phase, its disordered analogue (to the right of the critical point) to the Fermi liquid phase, and the quantum critical regime (above the critical point) to the strange metal phase. The superconducting dome surrounds the critical point.

that a possible phase transition occurs at a critical doping in the zero temperature limit. The antiferromagnetic ordering is commensurate with the lattice structure in the undoped parent compounds, i.e., in rational multiples of the lattice parameters. The electron-doped cuprates show a weakening of the long-range antiferromagnetic order as doping increases from $x = 0$, consistent with a dilution of the spin structure. As a result, T_N steadily decreases with doping. The magnetic phase diagram is shown in Fig. 1.7. It is still under debate as to whether long-range antiferromagnetic order coincides with the superconducting region, or if only short-range antiferromagnetic order exits. Nevertheless, the vanishing of the antiferromagnetic phase at a certain doping (with a paramagnetic phase at higher doping) strongly suggests a magnetic phase transition at a critical doping. Concomitant with the Fermi surface rearrangement near the same doping, it was argued that a quantum phase transition occurs at this critical doping [49].

A quantum phase transition [54] is a phase transition between different phases of matter at zero temperature. Contrary to traditional temperature driven thermodynamic phase transitions, quantum phase transitions can be only be accessed by varying a physical parameter-such as magnetic field, pressure or doping - at absolute zero temperature. The transition describes an abrupt change in the ground state of a many-body system due to its quantum fluctuations. Fig. 1.8 shows a schematic of the funnel-like phase diagram for a quantum phase transition in cuprates. Two distinct phases are well separated by the quantum critical point (QCP) in the ground state. In the electron-doped cuprate case, the tuning parameter is doping and the transition from antiferromagnetic (AFM) phase to paramagnetic (PM) phase at

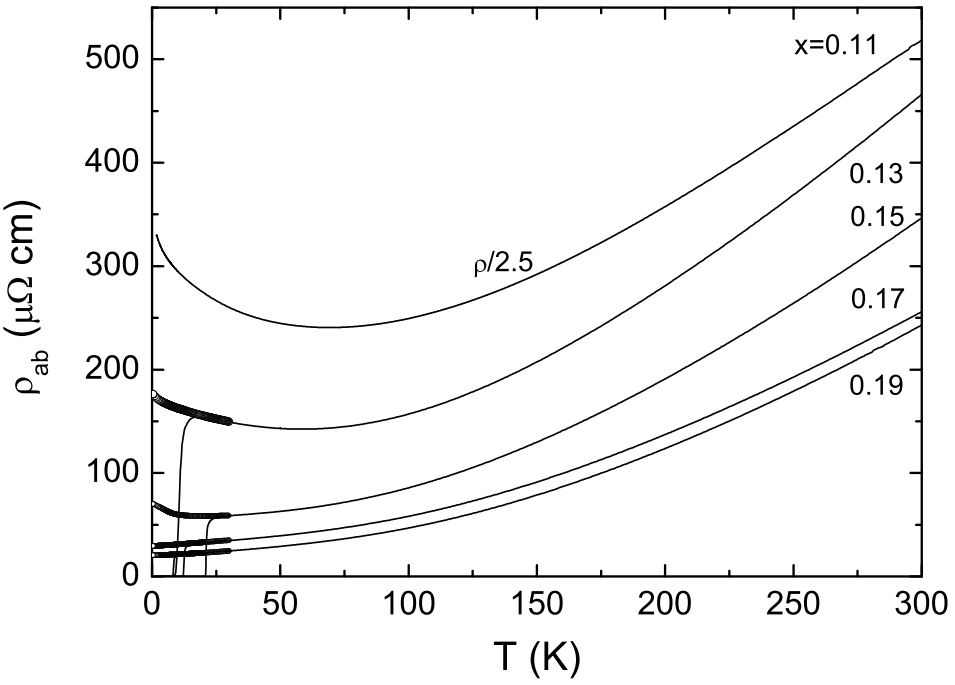

Figure 1.9: Temperature dependence of the in-plane resistivity of $Pr_{2-x}Ce_xCuO_{4-\delta}$ films in zero field (thin lines) and H=10 T (thick circles).

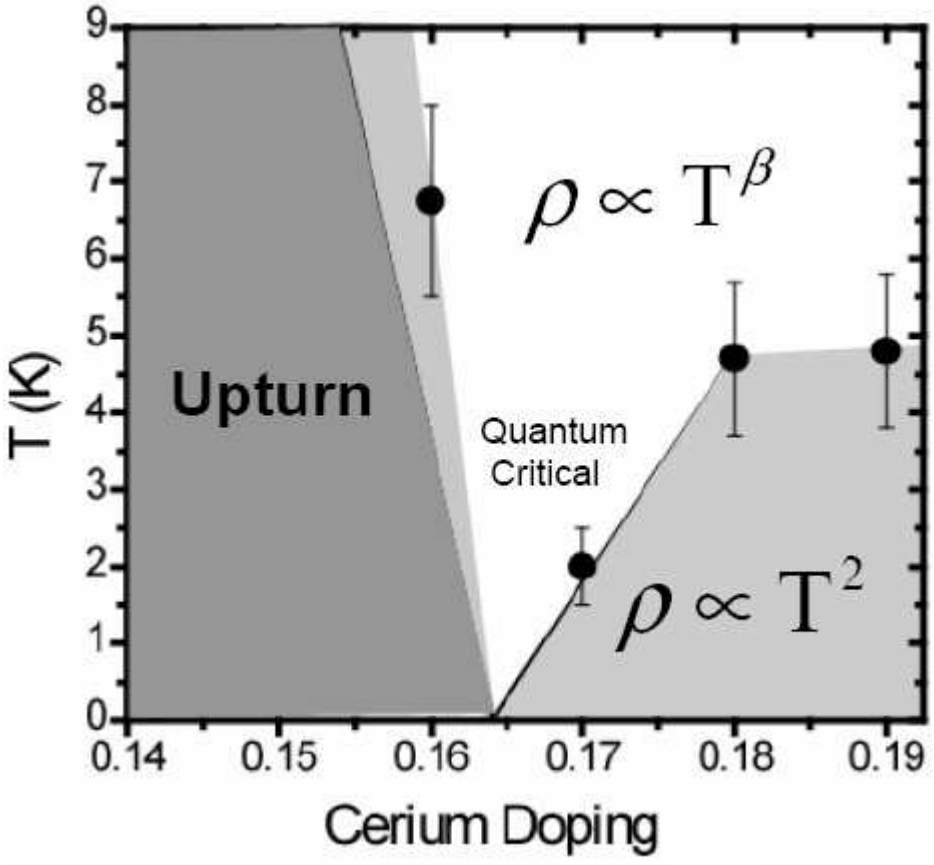

Figure 1.10: Schematic representation of the temperature dependence of the resistivity for various dopings. The data points indicate where quadratic behavior ($\rho \propto T^2$) is recovered at lower temperatures. This is reminiscent of the funnel region associated with a quantum critical point (Y. Dagan, unpublished).

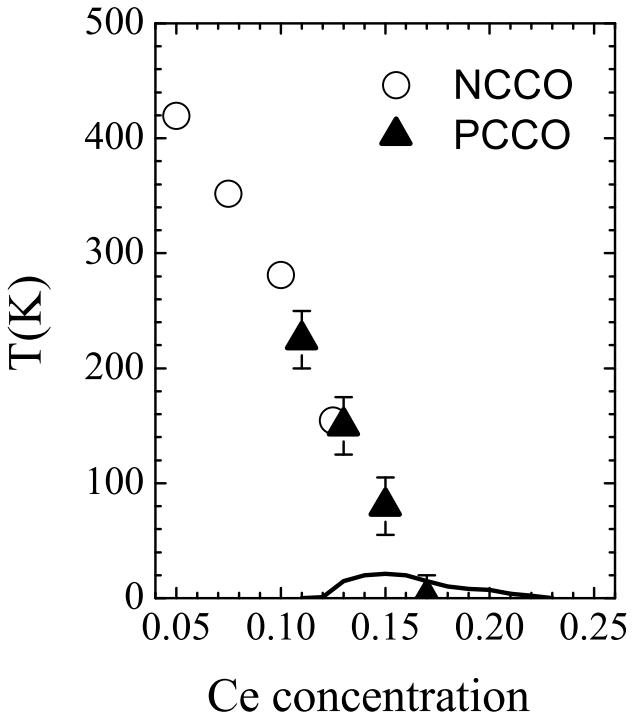

Figure 1.11: Doping dependence of a normal state gap in electron-doped cuprates from ab-plane optical conductivity [57]. Symbols show the T^* below which the optical gap appears.

T=0 can be regarded as a quantum phase transition. Besides the abrupt change in the doping dependence of Hall coefficient for T$\sim$0 [Fig. 1.5(b)], other transport data is also suggestive of a quantum phase transition in electron-doped cuprates. As shown in Fig. 1.10, the temperature dependence of the normal state resistivity in $Pr_{2-x}Ce_xCuO_4$ (PCCO) shows a dramatic contrast between the underdoped and overdoped regions. In the underdoped and optimally-doped samples, a resistivity upturn develops at low temperature when the normal state is achieved by applying a magnetic filed higher than the critical field. As found in Fig. 1.9, the resistivity upturn vanishes near a critical doping [55, 56]. Meanwhile, the normal state resistivity in the overdoped region changes from a quadratic temperature dependence (T^2) at low temperature to a less than 2 power dependence at higher temperature, suggesting a crossover from a Fermi-liquid like regime at low temperature to the fluctuation region at high temperature. Optical conductivity experiments [57] revealed the opening of a partial normal state gap below a certain temperature (T^*) in the underdoped region, with no such gap above a critical doping, as shown in Fig. 1.11. This normal state gap and the doping variation of R_H have been explained by a spin density wave (SDW) gap model [58, 59]. In this model, SDW ordering would induce a Fermi surface reconstruction and result in an evolution from an electron pocket to the coexistence of electron- and hole-like pockets with increasing doping, and eventually into a single hole-like Fermi surface. The SDW gap amplitude decreases from the underdoped side and vanishes at a critical doping. Details of the SDW model will be presented in the a subsequent chapter.

1.6 Motivation and outline

As we have shown above, electron-doped cuprate superconductors exhibit a number of interesting properties and the origin of these properties is still unknown. For example, the quadratic temperature dependence of resistivity, the low temperature resistivity upturn in the underdoped region, and the high energy gap seen in optics are not yet understood. Therefore, in order to clarify the physics of the n-type cuprates and to understand their relation to the hole-doped cuprates, it is important to investigate them in much more detail. In the next few paragraphs, we outline some of the projects undertaken in this thesis to better understand the high-T_c cuprates.

It is convenient to study the low temperature normal state properties of electron-doped cuprates because they have a low upper critical field. A few interesting observations in the normal state for temperature below T_c have been reported. The kink feature of the zero temperature Hall coefficient indicates a sudden change of band structure at a critical doping and thus suggests a quantum phase transition. To further investigate the low temperature normal state properties of electron-doped cuprates, we utilized thermoelectric power, which is also sensitive to the band structure (and scattering) as a probe of the doping dependent anomalies. In chapter 4, we investigate the field driven normal state thermoelectric power at low temperatures in $Pr_{2-x}Ce_xCuO_{4-\delta}$ films with various doping. An abrupt change of low temperature thermopower at x=0.16 is observed. The kink behavior in doping dependent thermopower and the previously reported normal state Hall coefficient

can be correlated via a simple model, strongly supporting the picture of a Fermi surface rearrangement at a critical doping. This is a further evidence for a quantum phase transition in the electron-doped cuprate superconductors.

High magnetic field is a powerful tool for revealing features in electrical transport that are not observable in low field, such as a field dependent Hall resistivity or magnetoresistance anomalies. In chapter 5, we present Hall effect and magnetoresistance measurements in pulsed magnetic field (58 T) on $Pr_{2-x}Ce_xCuO_{4-\delta}$ films. A strong non-linear field dependent Hall resistivity is found above the optimal doping in a certain temperature range, while the low field linearity persists up to 58 T in the underdoped region at all measured temperatures. Concomitant with this changes in the field dependence of longitudinal magnetoresistance are found. These results also imply that a quantum phase transition occurs under the superconductivity dome in electron-doped cuprates. A SDW model is used to explain qualitatively these high-field results.

A measurable parallel critical field is possible for electron-doped cuprates, but no such experiments have been reported. Utilizing the high pulsed magnetic field, in chapter 6, we systematically measured the resistive superconducting transition in electron-doped cuprates $Pr_{2-x}Ce_xCuO_{4-\delta}$ films for temperature down to 1.5 K and magnetic field up to 58 T applied parallel to the conducting ab-planes. We find that the zero temperature parallel critical field ($H_{c2\|ab}(0)$) exceeds 58 T for the underdoped and optimally-doped films. For the overdoped films, 58 T is sufficient to suppress the superconductivity. We also find that the Zeeman energy $\mu_B H_{c2\|ab}(0)$ reaches the superconducting gap ($\triangle_0$), i.e., $\mu_B H_{c2\|ab}(0) \simeq \triangle_0$, for all the dopings,

strongly suggesting that the parallel critical field is determined by the Pauli paramagnetic limit in electron-doped cuprates.

Prior vortex Nernst effect measurements have shown a much weaker superconducting fluctuation effect in electron-doped cuprates, compared with the hole-doped cuprates. In chapter 7, we employed a Nernst effect measurement through the entire doping and temperature ranges. A stronger superconducting fluctuation is observed in the underdoped region, but weaker than in the hole-doped cuprates. We explain this to be consistent with the incoherent phase fluctuations picture. For the normal state, the Nernst effect is also a useful probe for understanding the electronic structure. We find a large Nernst signal near optimal doping, which, as explained in prior work, is a result of two-carrier transport. Experiments and theory have suggested that the overdoped electron-doped cuprates are Fermi-liquid metals with a large hole-like Fermi surface. In this case, a small Nernst signal is expected. However, our measurements have revealed a fairly large Nernst signal at the doping extremes (highly overdoped and slightly underdoped) in the normal state, implying that the band structure is more complicated than previously believed.

As an additional work, we studied superconducting fluctuation effects in a hole-doped cuprate. The incoherent phase fluctuations observed in some hole-doped cuprates (such as LSCO) has been a topic of major significance over the past several years. In chapter 8, measurements of Nernst effect, resistivity and Hall angle on epitaxial films of $Y_{1-x}Pr_xBa_2Cu_3O_{7-\delta}$ (Pr-YBCO, $0 \leq x \leq 0.4$) are performed over a broad range of temperature and magnetic field. While the Hall and resistivity data suggest a broad pseudogap regime in accordance with earlier results, these

first measurements of the Nernst effect on Pr-YBCO show a large signal above the superconducting transition temperature T_c. This effect is attributed to vortex-like excitations in the phase incoherent condensate existing above T_c. A correlation between disorder and the width of the phase fluctuation regime has been established for the YBCO family of cuprates, which suggests a $T_c \simeq 110$ K for disorder-free $YBa_2Cu_3O_{7-\delta}$.

Chapter 2

Review of Transport Theory

In this chapter, we briefly review the semiclassical transport theories based on the Boltzmann equation. Boltzmann transport theory can be found in textbooks, such as *Condensed Matter Physics by Marder* [60], *Princples of the Theory of Solids* by Ziman [61], *Solid State Physics* by Ashcroft & Mermin [62] and *The Hall Effect in Metals and Alloys* by Hurd [63]. The theory for thermopower and Nernst effect can be found in *Thermoelectricity in metals and alloys* by Barnard[64].

2.1 The Boltzmann equation

Boltzmann theory is a semi-classical phenomenological approach to describing the motion of carriers and energy through matter. The theory deals with the evolution of the carrier distribution subjected to various fields and gradients rather than describing each carrier individually. The advantage of using distribution functions, which give the probability of a particle in a particular state, is that it allows one to describe macroscopic behavior without knowing precisely the microscopic information of each charge carrier.

The numbers of carriers in a neighborhood region around $\vec{r}$ with a wave vector $\vec{k}$ is described by the distribution function $f_{\vec{k}}(\vec{r}, t)$. The distribution function measures the local charge density function and it is subject to disturbance from

thermal diffusion, external fields, and scattering centers. Diffusion is the movement of particles in and out of a small region around $\vec{r}$ due to their diffusion velocity, $\vec{v}$. The time change of the distribution function due to diffusion is given by:

$$\frac{\partial f_{\vec{k}}}{\partial t}|_{diff} = -\frac{\partial f_{\vec{k}}}{\partial \vec{r}}\frac{\partial \vec{r}}{\partial t} = -\frac{\partial f_{\vec{k}}}{\partial \vec{r}}\vec{v} \tag{2.1}$$

External electric and magnetic fields can also change the distribution function of the particles. They change the momentum of the carriers through the Lorenz force:

$$\hbar\dot{\vec{k}} = e(\vec{E} + \vec{v}_{\vec{k}} \times \vec{B}) \tag{2.2}$$

The number of particles with a given wave vector will change due to this change in momentum by:

$$\frac{\partial f_{\vec{k}}}{\partial t}|_{diff} = -\frac{\partial f_{\vec{k}}}{\partial \vec{k}}\frac{\partial \vec{k}}{\partial t} = -\frac{e}{\hbar}\left(\vec{E} + \vec{v}_{\vec{k}} \times \vec{B}\right) \cdot \frac{\partial}{\partial \vec{k}} f_{\vec{k}\vec{r}} \tag{2.3}$$

Another effect that can change the number of carriers entering or exiting a region is scattering with impurities or with other carriers. The effect of these collisions will be represented by $\frac{\partial f_{\vec{k}}}{\partial t}|_{scatt}$.

The total change in the distribution function is:

$$\dot{f}_{\vec{k}\vec{r}} = \dot{f}_{\vec{k}\vec{r}}|_{diff} + \dot{f}_{\vec{k}\vec{r}}|_{field} + \dot{f}_{\vec{k}\vec{r}}|_{scatt} \tag{2.4}$$

where the dot denotes $\frac{\partial}{\partial t}$. In the steady state the number of particles entering a region should be equal to the number of particles exiting it, i.e., $\dot{f}_{\vec{k}\vec{r}}$=0. Usually the scattering term is the most difficult term to determine, therefore the Boltzmann equation in steady state is written as:

$$\dot{f}_{\vec{k}\vec{r}}|_{diff} + \dot{f}_{\vec{k}\vec{r}}|_{field} = -\dot{f}_{\vec{k}\vec{r}}|_{scatt} \tag{2.5}$$

or

$$\dot{f}_{\vec{k}\vec{r}}|_{scattering} = \vec{v}_{\vec{k}} \cdot \frac{\partial}{\partial \vec{r}} f_{\vec{k}\vec{r}} + \frac{e}{\hbar}\left(\vec{E} + \vec{v}_{\vec{k}} \times \vec{B}\right) \cdot \frac{\partial}{\partial \vec{k}} f_{\vec{k}\vec{r}} \tag{2.6}$$

The experimentally accessible and practically important transport properties such as conductivity, Hall coefficient and thermoelectric power can be calculated by solving for $f_{\vec{k}}$.

In the case where there are no external fields or thermal gradients, the system is in equilibrium and the scattering term, $\dot{f}^{\circ}_{\vec{k}\vec{r}}|_{scattering}$, is zero. Deviation of the distribution from the equilibrium state caused by external disturbance can be obtained by an expansion of f to first order.

$$g_{\vec{k}\vec{r}} = f_{\vec{k}\vec{r}} - f^{\circ}_{\vec{k}\vec{r}} \tag{2.7}$$

It is convenient to assume that the typical time scale for the processes described by the right hand side of Eq. 2.6 are slow compared to the time between scattering events. The small change in f then occurs over some timescale, τ, and the repeated process results in a steady state of the system. τ is called the relaxation time and it measures the time needed for the equilibrium state to recover from the last scattering. The Boltzmann equation now reads

$$\dot{f}_{\vec{k}\vec{r}}|_{scattering} \approx \frac{g_{\vec{k}\vec{r}}}{\tau} = \vec{v}_{\vec{k}} \cdot \frac{\partial}{\partial \vec{r}} f^{\circ}_{\vec{k}\vec{r}} + \frac{e}{\hbar}(\vec{E} + \vec{v}_{\vec{k}} \times \vec{B}) \cdot \frac{\partial}{\partial \vec{k}} f^{\circ}_{\vec{k}\vec{r}} \tag{2.8}$$

In the equilibrium state, the distribution is location independent, thus $\frac{\partial}{\partial \vec{r}} f^{\circ}_{\vec{k}\vec{r}}$=0. Then the Boltzmann equation can be simplified to

$$\frac{g_{\vec{k}\vec{r}}}{\tau} = \frac{e}{\hbar}(\vec{E} + \vec{v}_{\vec{k}} \times \vec{B}) \cdot \frac{\partial}{\partial \vec{k}} f^{\circ}_{\vec{k}\vec{r}} \tag{2.9}$$

Note that τ is usually considered as constant when solving Eq. 2.9. However, in a real scattering process, τ is dependent on $\vec{k}$ through the energy and disorders. Therefore, this equation is only rough approximation of general transport dependencies.

2.2 Electrical conductivity

In the presence of an electrical field $\vec{E}$ only, the induced electrical current density is given by Ohm's rule

$$\vec{j} = -ne\vec{v} = \sigma\vec{E} \tag{2.10}$$

and the carrier density contributing to current in the volume element $d\vec{k}$ is

$$n = \int \frac{g_{\vec{k}\vec{r}}}{4\pi^3} d\vec{k} \tag{2.11}$$

Since $\vec{v}$ is the group velocity of the electron wave packet, i.e. an electron in state $\vec{k}$, defined by $\frac{1}{\hbar}\frac{\partial\epsilon}{\partial\vec{k}} \equiv \vec{v}$ (here ϵ is the electron energy), then the induced current density which results from the change in the distribution function from its equilibrium value is

$$\vec{j} = -e^2 \int \frac{d\vec{k}}{4\pi^3} \vec{v}\tau \left(\vec{E}\cdot\vec{v}\right) \frac{\partial f^\circ}{\partial\epsilon} \tag{2.12}$$

where the distribution function does not depend on position (without thermal gradient) and the k-vector dependence is implied. The conductivity tensor can now be determined by using Eq. 2.10.

$$\sigma_{ij} \equiv \frac{j_i}{E_j} = -e^2 \int \frac{d\vec{k}}{4\pi^3} v_i \tau v_j \frac{\partial f^\circ}{\partial\epsilon} \tag{2.13}$$

In the isotropic (cubic symmetry) case, this expression is diagonal and reduces to the well known Drude model.

$$\sigma_{ii} = \frac{ne^2\tau}{m^*} \tag{2.14}$$

In the anisotropic case (e.g. tetragonal symmetry), the conductivity tensor is still diagonal with $\sigma_{ii} = \sigma_{jj} \neq \sigma_{kk}$. The resistivity tensor is just the inverse of the conductivity tensor and for a diagonal matrix this gives

$$\rho_{ii} = \sigma_{ii}^{-1} = \frac{m^*}{ne^2\tau} \tag{2.15}$$

2.3 Hall effect

Under the influence of an electrical field $\vec{E}$, the induced current consists of carriers parallel to $\vec{E}$. By applying a magnetic field $\vec{B}$ perpendicular to this direction the carriers will be deflected into the direction $\vec{v} \times \vec{B}$ and thus generate a transverse electrical field to balance the magnetic deflection. This transverse electrical field $\vec{E_y}$ characterizes the Hall effect. The Hall coefficient, R_H, is then defined as

$$E_y = R_H J_x B_z \tag{2.16}$$

For free electrons (Drude model), the transverse electrical field balances the magnetic deflection, therefore no current will flow along the transverse direction, that is

$$eE_y = ev_x B_z \tag{2.17}$$

with the current density $J_x = nev_x$, so that

$$E_y = \frac{1}{ne} J_x B_z \tag{2.18}$$

therefore,

$$R_H = \frac{1}{ne} \tag{2.19}$$

Obviously, the Hall field is perpendicular to both magnetic field and electric current and its direction depends on the sign of the charge carriers.

A more rigorous derivation can be obtained from Boltzmann equation. In the presence of both magnetic and electric field, the Boltzmann equation is

$$\frac{g_{\vec{k}}}{\tau} = \frac{e}{\hbar}\left(\vec{E} + \vec{v}_{\vec{k}} \times \vec{B}\right) \cdot \frac{\partial}{\partial \vec{k}} f^{\circ}_{\vec{k}} \tag{2.20}$$

Replacing $\frac{\partial f^{\circ}}{\partial \vec{k}} = \hbar \vec{v} \frac{\partial f^{\circ}}{\partial \epsilon}$, Eq. (2.20) is rewritten as

$$\frac{g(\vec{v})}{\tau} = -\vec{v} \cdot e\vec{E} \frac{\partial f^{\circ}}{\partial \epsilon} - \frac{e}{m^*} \vec{v} \cdot \left(\vec{B} \times \frac{\partial g(\vec{v})}{\partial \vec{v}}\right) \tag{2.21}$$

where $m^* \equiv 1/\frac{\partial \vec{v}}{\hbar \partial k}$ is the effective mass of carriers.

A solution for g is

$$g(\vec{v}) = -\tau e \frac{\partial f^{\circ}}{\partial \epsilon} \vec{v} \cdot \frac{[\vec{E} + \frac{e\tau}{m^*}{}^2 \vec{B}\vec{B} \cdot \vec{E} - \frac{e\tau}{m^*} \vec{B} \times \vec{E}]}{1 + \frac{e\tau}{m^*}{}^2 B^2} \tag{2.22}$$

With this equation for the change in the distribution function, we can calculate the conductivity (or resistivity) tensor according to Eq. 2.10. Taking $\vec{E}$ perpendicular to $\vec{B}$, we can rewrite Eq. 2.10 as

$$\vec{J} = \sigma_{\vec{E}} \vec{E} + \sigma_{\vec{B}} (\vec{B} \times \vec{E}) \tag{2.23}$$

the conductivity tensor then is

$$\sigma_{ij} = \begin{pmatrix} \sigma_E & -\sigma_B B \\ \sigma_B B & \sigma_E \end{pmatrix} \tag{2.24}$$

Obviously, the current is related to the electric field by a tensor whose off-diagonal part is antisymmetric and proportional to $|\vec{B}|$. The conductivity tensors are defined by

$$\sigma_{\vec{E}} = -\frac{1}{3}\int \frac{v^2 e^2 \tau(\partial f^\circ/\partial\epsilon)\mathrm{d}\vec{k}}{1+(e\tau B/m^*)^2} \tag{2.25}$$

$$\sigma_{\vec{B}} = -\frac{1}{3}\int \frac{v^2 e^2 \tau(\partial f^\circ/\partial\epsilon)(\frac{e\tau}{m^*})\mathrm{d}\vec{k}}{1+(e\tau B/m^*)^2} \tag{2.26}$$

The Hall coefficient can be obtained by inverting the tensor relation (2.24), i.e.,

$$R_H = \frac{\sigma_B}{\sigma_E^2 + B^2\sigma_B^2} = \frac{e\tau}{m^*\sigma_0} = 1/ne \tag{2.27}$$

here we used $\rho_{ii} = \frac{\sigma_E}{\sigma_E^2+\sigma_B^2 B^2}$ and Eq. 2.13.

In general, the Hall coefficient depends on the shape of the Fermi surface and the scattering time on the Fermi surface. A useful parameter, the Hall angle θ, through which the direction of the current is skewed by the magnetic field, can be defined as

$$tan\theta = \frac{B\sigma_{\vec{B}}}{\sigma_{\vec{E}}} = \frac{e\tau B}{m^*} = \omega_c\tau \tag{2.28}$$

where $\omega_c = \frac{eB}{m^*}$ is the cyclotron frequency.

2.4 Thermoelectric and Nernst effects

The thermoelectric effect arise from the interaction between electric and thermal currents. In the absence of magnetic field, when a thermal gradient is applied along the sample (x-direction), a longitudinal electric field arises between its two ends due to the charge current density $\vec{J}$ driven by the temperature gradient. This thermal gradient induces an electric field known as the thermoelectric field. When an external magnetic field is present (in z-direction) in conjunction with the temperature gradient in the longitudinal direction, the Lorentz force will deflect charge carriers along the transverse direction (y-direction) and the induced transverse voltage is known as the Nernst voltage. A schematic diagram is shown in Fig. 2.1 to illustrating the charge transport in the thermopower and Nernst effect measurements. In the following, we summarize the discussions of Nernst effect in Refs. [65, 67]

The relations between charge and heat current densities can be described as [61]:

$$\vec{J} = \hat{\sigma}\vec{E} - \hat{\alpha}\vec{\nabla}T \tag{2.29}$$

where J is charge current density, $\hat{\sigma}$ and $\hat{\alpha}$ are electric and Peltier conductivity tensors respectively, $\vec{E}$ and $\vec{\nabla}T$ are electrical field and thermal gradient. In the absence of an external electrical field and external magnetic field, from 2.29, the longitudinal current density J_x is:

$$J_x = \sigma_{xx}E_x + \alpha_{xx}(-\bigtriangledown_x T) \tag{2.30}$$

If we impose the boundary condition of J_x=0, Eq. 2.30 yields the longitudinal

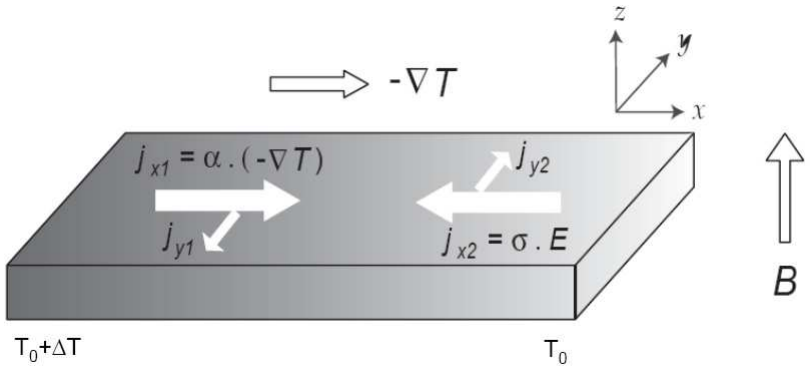

Figure 2.1: The longitudinal electrical current j_x and transverse current j_y produced by the thermal gradient $-\nabla T$ and electrical field E. With temperature gradient only, the unbalanced longitudinal current engenders the thermoelectric effect. With both temperature gradient and magnetic field, the unbalanced transverse current engenders the Nernst effect (from Ref. [68]).

electrical field (thermoelectric field)

$$E_x = -(\alpha_{xx}/\sigma_{xx})(-\bigtriangledown_x T) \tag{2.31}$$

The thermoelectric coefficient (or Seebeck coefficient) is defined by

$$S = E_x/\bigtriangledown_x T = \alpha_{xx}/\sigma_{xx} \tag{2.32}$$

In the presence of a magnetic field (B$\|z$-axis) and the same temperature gradient, a transverse voltage is developed under the boundary condition J_y=0. The components of Eq. 2.29 are

$$\begin{aligned} J_x &= \sigma_{xx}E_x + \sigma_{xy}E_y + \alpha_{xx}(\bigtriangledown_x T) + \alpha_{xy}(-\bigtriangledown_y T) \\ J_y &= \sigma_{xy}E_x + \sigma_{xx}E_y + \alpha_{xy}(-\bigtriangledown_x T) + \alpha_{xx}(-\bigtriangledown_y T) \end{aligned} \tag{2.33}$$

In the absence of electrical current, $J_x = 0$, by neglecting the transverse thermal gradient $- \bigtriangledown_y T$ and solving Eq. 2.33, we get the transverse electrical field (Nernst field)

$$E_y = \frac{\alpha_{xy}\sigma_{xx} - \alpha_{xx}\sigma_{xy}}{\sigma_{xx}^2 + \sigma_{xy}^2}(- \bigtriangledown_x T) \tag{2.34}$$

Using the small Hall angle approximation $tan\theta_H = \sigma_{xy}/\sigma_{xx} \ll 1$, we have $1/(\sigma_{xx}^2 + \sigma_{xy}^2) \sim 1/\sigma_{xx}^2$ and Eq. 2.34 is simplified as

$$E_y = \frac{\alpha_{xx}}{\sigma_{xx}} \bigtriangledown_x T(\frac{\alpha_{xy}}{\alpha_{xx}} - \frac{\sigma_{xy}}{\sigma_{xx}}) \tag{2.35}$$

Using Eq. 2.32 and we can rewrite the Nernst coefficient is written as

$$\nu = E_y/(B\nabla_x T) = S(\frac{\alpha_{xy}}{\alpha_{xx}} - \frac{\sigma_{xy}}{\sigma_{xx}})/B \tag{2.36}$$

and the Nernst signal is defined as $e_y = \nu B \equiv E_y/\nabla_x T$. This is usually linear in magnetic field for a normal metal, similar to the linear in field Hall resistivity. If we use the Hall angle $tan\theta_H \equiv \sigma_{xy}/\sigma_{xx}$, then ν is can be written as

$$\nu = (\frac{\alpha_{xy}}{\sigma_{xx}} - Stan\theta_H)/B \tag{2.37}$$

In a metal with single conduction band, the Nernst signal is usually negligible due to the so called Sondheimer cancellation. The idea of Sondheimer cancellation lies in Eq. 2.37. In a magnetic field B_z, the Peltier current $J_x^P = \alpha_{xx}(-\nabla_x T)$ spawns a Hall component $J_y^P = \alpha_{xy}(-\nabla_x T)$. On the other hand, the Hall current $J_y^S = \sigma_{xy}E_x$ generated by the counter-flow current (thermopower current $J_x^s = \sigma_{xx}E_x$) runs on the opposite direction. If they are comparable in magnitude, they cancel

each other and a very small Nernst field is needed to balance the transverse current. If we define a thermal (Peltier) Hall angle as $tan\theta_T \equiv \alpha_{xy}/\alpha_{xx}$, the Nernst coefficient can be written as

$$\nu = S(tan\theta_T - tan\theta_H)/B. \tag{2.38}$$

When θ_H and θ_T are energy independent, from Eq. 2.51 and 2.52, it is easy to see that $tan\theta_H \simeq tan\theta_T$. Hence we have a perfect cancellation along the y direction.

A more rigorous expression for thermopower and Nernst effect can be obtained within the standard Boltzmann formulation (section 2.1), Under a temperature gradient, the diffusive effect can be explicitly considered in the diffusion term of Eq. 2.8:

$$\vec{v}_{\vec{k}} \cdot \frac{\partial f_{\vec{k}}}{\partial r} = \vec{v}_{\vec{k}} \cdot \frac{\partial f_{\vec{k}}}{\partial T} \nabla T \tag{2.39}$$

Assuming that the temperature gradient is uniform throughout the sample and that at any given point the distribution function, $f_{\vec{k}}$, deviates only slightly from a local equilibrium distribution function, $f^{\circ}_{\vec{k}}(r)$, Eq. 2.39 can be simplified as:

$$\vec{v}_{\vec{k}} \cdot \frac{\partial f_{\vec{k}}}{\partial r} = \vec{v}_{\vec{k}} \cdot \frac{\partial f^{\circ}_{\vec{k}}}{\partial T} \nabla T \tag{2.40}$$

The magnetic field on the other hand has a more complicated effect. The previous approximation of substituting $f^{\circ}_{\vec{k}}$ instead of $f_{\vec{k}}$ fails since the magnetic field does not have any net effect on the equilibrium distribution. Therefore, we should use the approximation of equation Eq. 2.8 and the Boltzmann equation becomes

$$\vec{v}_{\vec{k}} \cdot \frac{\partial f^{\circ}_{\vec{k}}}{\partial T} \nabla T = -\dot{f}_{\vec{k}}|_{scatt} + \frac{e}{\hbar}(\vec{v} \times \vec{B}) \cdot \frac{\partial g}{\partial \vec{k}} \tag{2.41}$$

Since it is more convenient to measure the deviation from equilibrium in terms of

group velocity of carriers rather than the wave vector, we can make an adjustment,

$$\frac{e}{\hbar}(\vec{v}\times\vec{B})\cdot\frac{\partial g}{\partial\vec{k}}=\frac{e}{\hbar}(\vec{v}\times\vec{B})\cdot\frac{\partial\vec{v}}{\partial\vec{k}}\frac{\partial g}{\partial\vec{v}} \tag{2.42}$$

With the relaxation time approximation for the scattering term in Eq. 2.8: $\dot{f}_k|_{scatt} = -\frac{g(k)}{\tau}$, the Boltzmann equation 2.41 can be rewritten as

$$\begin{aligned}\vec{v}_{\vec{k}}\cdot\frac{\partial f^{\circ}_{\vec{k}}}{\partial T}\nabla T &= [\frac{1}{\tau}+\frac{e}{\hbar}(\vec{v}\times\vec{B})\cdot\frac{\partial\vec{v}}{\partial\vec{k}}\frac{\partial}{\partial\vec{v}}]g(\vec{v}) \\ &= [\frac{1}{\tau}+\frac{e}{m^*}(\vec{v}\times\vec{B})\cdot\frac{\partial}{\partial\vec{v}}]g(\vec{v})\end{aligned} \tag{2.43}$$

It is more practical to use the energy dependence rather than the temperature dependence and the left side of Eq. 2.43 can be written as:

$$\vec{v}_{\vec{k}}\cdot\frac{\partial f^{\circ}_{\vec{k}}}{\partial T}\nabla T=\vec{v}_{\vec{k}}\cdot\frac{\partial f^{\circ}_{\vec{k}}}{\partial\epsilon}\frac{\partial\epsilon}{\partial T}\nabla T\approx\vec{v}_{\vec{k}}\cdot\frac{\partial f^{\circ}_{\vec{k}}}{\partial\epsilon}(\frac{\epsilon-\mu}{T})\nabla T \tag{2.44}$$

where μ is the chemical potential. Now the Boltzmann Eq. 2.43 reads:

$$\vec{v}_{\vec{k}}\cdot\frac{\partial f^{\circ}_{\vec{k}}}{\partial\epsilon}(\frac{\epsilon-\mu}{T})\nabla T=(\frac{1}{\tau}+\frac{e}{\hbar}(\vec{v}\times\vec{B})\cdot\frac{\partial\vec{v}}{\partial\vec{k}}\frac{\partial}{\partial\vec{v}})g(\vec{v}) \tag{2.45}$$

In the low magnetic field limit, a solution for $g(\vec{v})$ is

$$g(\vec{v})=-(1-\frac{e\tau}{\hbar}\vec{v}\times\vec{B}\cdot\frac{\partial}{\partial\vec{k}})\tau\vec{v}_{\vec{k}}\cdot\frac{\partial f^{\circ}_{\vec{k}}}{\partial\epsilon}(\frac{\epsilon-\mu}{T})\nabla T \tag{2.46}$$

This solution is equivalent to determining $g(\vec{v})$ accurate up to successive powers of $\vec{B}$ and ∇T. The zeroth order solution which is linear in ∇T would be:

$$g^{(0)}(\vec{v})=-\tau\vec{v}_{\vec{k}}\cdot\frac{\partial f^{\circ}_{\vec{k}}}{\partial\epsilon}(\frac{\epsilon-\mu}{T})\nabla T \tag{2.47}$$

Because the magnetic field is zero and only a thermal gradient is considered in this situation, $g^{(0)}$ is the deviation of the distribution function from the equilibrium

for the diagonal component of the Peltier coefficient α_{xx}. Similarly, the first order term which is linear in ∇T and $\vec{B}$ gives the distribution function for the off-diagonal Peltier coefficient α_{xy}:

$$g^{(1)}(\vec{v}) = \frac{e\tau}{\hbar}\vec{v} \times \vec{B} \cdot \frac{\partial g^{(0)}(v)}{\partial \vec{k}} \tag{2.48}$$

Since the off-diagonal current J_y is just $eg^{(1)}v_k$ integrated over the Fermi surface, the off-diagonal conductivity is [in terms of the mean-free-path $\vec{l}(\vec{k}) \equiv \vec{v_k}\tau$)]

$$\alpha_{xy} = e^2 \int \frac{\epsilon - \mu}{T}(-\frac{\partial f^{\cdot}}{\partial \epsilon})\frac{\vec{v_k} \times \vec{B}}{\hbar} l_y \frac{\partial l_x}{\partial \vec{k}} \tag{2.49}$$

In a two-dimensional system with an arbitrary dependence of $l(\vec{k})$ on $\vec{k}$, we may use the swept area representation [66] to reduce above expression to

$$\alpha_{xy} = \frac{2e^2 B}{(2\pi)^2 T\hbar^2} \int d\epsilon(-\frac{\partial f^{\cdot}}{\partial \epsilon})(\epsilon - \mu)A_l(\epsilon) \tag{2.50}$$

where $A_l(\epsilon) = \oint dl_x l_y$ is the area swept out by $\vec{l}(\vec{k})$ as $\vec{k}$ goes around a contour at energy ϵ. As σ_{xy} is proportional to $A_l(\mu)$ [66], we find

$$\alpha_{xy} = \frac{\pi^2 k_B^2 T}{3e}\frac{\partial \sigma_{xy}}{\partial \epsilon}|_{\epsilon=\mu} \tag{2.51}$$

Similarly, the longitudinal thermoelectric conductivity is

$$\alpha_{xx} = \frac{\pi^2 k_B^2 T}{3e}\frac{\partial \sigma_{xx}}{\partial \epsilon}|_{\epsilon=\mu} \tag{2.52}$$

Insert this formulation into the expressions for thermopower in 2.32, and one finds

$$S = \frac{\pi^2 k_B^2 T}{3e}\frac{\partial ln\sigma(\epsilon)}{\partial \epsilon}|_{\mu} \tag{2.53}$$

From the Nernst effect expression (Eq. 2.36), the Nernst signal becomes

$$\begin{aligned} e_y &= \frac{\pi^2 k_B^2 T}{3e}[\frac{\alpha_{xy}}{\sigma_{xx}} - \frac{\sigma_{xy}}{\sigma_{xx}}\frac{\alpha_{xx}}{\sigma_{xx}}] \\ &= \frac{\pi^2 k_B^2 T}{3e}\frac{\sigma_{xy}}{\sigma_{xx}}[\frac{\partial \sigma_{xy}/\partial \epsilon}{\sigma_{xy}} - \frac{\partial \sigma_{xy}/\partial \epsilon}{\alpha_{xx}}] \end{aligned}$$

If we use the small Hall angle approximation, $tan\theta_H \approx \theta_H = \frac{\sigma_{xy}}{\sigma_{xx}} = \frac{e\tau B}{m}$ (this is usually true in metals), above equation becomes

$$\begin{aligned} e_y &= \frac{\pi^2 k_B^2 T}{3e}\theta_H(\frac{\partial\sigma_{xy}}{\partial\epsilon} - \frac{\partial\sigma_{xx}}{\partial\epsilon}) \\ &= \frac{\pi^2 k_B^2 T}{3e}\frac{\partial\theta_H}{\partial\epsilon}|_{\epsilon=\mu} \end{aligned} \tag{2.54}$$

Plugging in $\theta_H \approx \omega_c\tau$, one gets

$$\nu = \frac{\pi^2 k_B^2 T}{3m}\frac{\partial\tau}{\partial\epsilon}|_{\epsilon=\mu} \tag{2.55}$$

Since the Hall angle depends primarily on the scattering time, the Nernst coefficient is usually known to give information about the energy dependence of the scattering time. In normal metals the Hall angle, and hence the scattering time, is only weakly energy dependent at the Fermi energy and therefore the Nernst signal is usually very small. The thermoelectric power, however, depends on the carrier density (or inverse of Fermi energy) (see Eq. 4.6 and Ref. [64] for details) and therefore, it is usually large for a system with low carrier density.

2.5 Two-band (carrier) model

The above sections have been discussed for a single carrier system. In this section, we will focus on a two-carrier model, which contains basic assumptions that simplify the transport equations beyond the assumptions made in Boltzmann transport theory. This model, frequently used in the literature, relies on the Drude model for conductivity and so incorporates an isotropic scattering rate on a spherical

Fermi surface. In addition, the Drude model assumes a constant scattering time for each band, and it does not predict temperature dependencies. The Drude model also assumes that both scattering and carrier density are not magnetic field dependent.

2.5.1 Magnetoresistance and Hall effect

The two-band model considers two conduction bands, i.e., electrons and holes. In transport, each band behaves independently and there is no interband interaction.

In the presence of both electrical and magnetic field, the current density is described by Eq. 2.23. The resistivity tensors for a single band system can be obtained by inverting the conductivity tensor in Eq. 2.24. For simplicity, we assume $\vec{E}$ is in the xy-plane and $\vec{B}$ in the z-direction.

$$\rho_{ij} = \sigma_{ij}^{-1} = \frac{1}{\sigma_E^2 + \sigma_B^2 B^2} \begin{pmatrix} \sigma_E & \sigma_B B \\ -\sigma_B B & \sigma_E \end{pmatrix} \tag{2.56}$$

The diagonal components, which relate the current density to the electric field driving that current, are independent of field, i.e., no magnetoresistance. The off-diagonal components are antisymmetric with magnetic field and are referred as the Hall effect that we have discussed previously.

For a system with only one conducting band, for convenience, using Eq. 2.24 and Eq. 2.25, we can simplify the resistivity tensor in Eq. 2.56 in terms of $\omega_c\tau$ as following,

$$\rho_{ij} = \begin{pmatrix} \rho_{xx}(=\frac{1}{\sigma_0}) & \rho_{xy}(=-R_H B = -\frac{\omega_c\tau}{\sigma_0}) \\ \rho_{xy}(=-R_H B = -\frac{\omega_c\tau}{\sigma_0}) & \rho_{xx}(=\frac{1}{\sigma_0}) \end{pmatrix} \tag{2.57}$$

where $\sigma_0 = \frac{nq^2\tau}{m^*}$ and $\omega_c = \frac{eB}{m^*}$. Since conductivities add in series, we invert this matrix (to obtain the conductivity matrix), and add the conductivities of the two bands ($\sigma = \sigma_1 + \sigma_2$). Inverting the resulting matrix gives back the resistivity tensor for the two bands.

$$\rho_{ij} = \frac{1}{(C_1+C_2)^2 + (C_1\gamma_1 + C_2\gamma_2)^2} \begin{pmatrix} (C_1+C_2) & -(C_1\gamma_1 + C_2\gamma_2) \\ (C_1\gamma_1 + C_2\gamma_2) & (C_1+C_2) \end{pmatrix} \tag{2.58}$$

where $C_i = \frac{\sigma_i}{(1+\gamma_i^2)}$, $\gamma_i = \omega_{c,i}\tau_i$, and $\sigma_i = \sigma_0$ with i as the band index.

The diagonal components give the resistivity along the direction of the applied electric field,

$$\rho_{ii} = \frac{C_1 + C_2}{(C_1+C_2)^2 + (C_1\gamma_1 + C_2\gamma_2)^2} \tag{2.59}$$

Replacing γ_i with $R_i\sigma_i B$, we have the expression for magnetoresistance,

$$\rho_{xx}(B) = \frac{(\sigma_h + \sigma_e) + \sigma_h\sigma_e(\sigma_h R_h^2 + \sigma_e R_e^2)^2 B^2}{(\sigma_h+\sigma_e)^2 + \sigma_h^2\sigma_e^2(R_h - R_e)^2 B^2} \tag{2.60}$$

where $\sigma_h(\sigma_e)$ is the conductivity of hole (electron) band and $R_h(R_e)$ the Hall coefficient of hole (electron) band. In the low field limit (i.e. $\gamma_i \ll 1$), the expression for magnetoreistance can be reduced to

$$\frac{\triangle\rho}{\rho} = \frac{\sigma_h\sigma_e(\sigma_h R_h - \sigma_e R_e)^2 B^2}{(\sigma_h+\sigma_e)^2} \tag{2.61}$$

This is the frequently observed B^2 dependence of magnetoresistance in metals.

The Hall coefficient can be obtained from the off-diagonal components

$$R_H = \frac{\rho_{ij}}{B} = \frac{1}{B}\frac{(C_1\gamma_1 + C_2\gamma_2)}{(C_1+C_2)^2 + (C_1\gamma_1 + C_2\gamma_2)^2} \tag{2.62}$$

An equivalent expression for Hall resistivity as a function of magnetic field then is

$$\rho_{xy}(B) = \frac{\sigma_h^2 R_h - \sigma_e^2 R_e - \sigma_h^2\sigma_e^2 R_h R_e (R_h - R_e) B^2}{(\sigma_e+\sigma_h)^2 + \sigma_e^2\sigma_h^2(R_h - R_e)^2 B^2} B \tag{2.63}$$

In the low field limit, the Hall coefficient expression simplifies to

$$R_H = \frac{R_h\sigma_h^2 + R_e\sigma_e^2}{\sigma^2} \tag{2.64}$$

From this, we see that the Hall coefficient is a balance between a negative contribution from the electron-like carriers and a positive contribution from the hole-like carriers. In the high field limit, it can be shown [63] that the Hall coefficient is $R_H = \frac{1}{e(n_e - n_h)}$ for an uncompensated metal ($n_h \neq n_e$) and it is zero for compensated metal ($n_h = n_e$).

2.5.2 Thermoelectric power and Nernst effect

In a two-band system, the counter-flowing of two types of charge carriers with opposite signs will contribute to both thermopower and Nernst effect.

Considering a material with two conduction bands, electron and hole, the total conductivity can be written as $\sigma_{xx} = \sigma_{xx}^h + \sigma_{xx}^e$ (h, e denote hole and electron), and similarly, the Peltier conductivity is $\alpha_{xx} = \alpha_{xx}^h + \alpha_{xx}^e$. From the definition of thermopower (Eq. 2.32), one finds [67]

$$S = \frac{\alpha_{xx}^h + \alpha_{xx}^e}{\sigma_{xx}^h + \sigma_{xx}^e} \tag{2.65}$$

Usually, the thermopower is small for a two band system since α_{xx} has an opposite sign for the two conduction bands.

Since Eq. 2.35 is written in terms of electrical and thermoelectric conductivities, by replacing the single band conductivity with the addition of the conductivities

from the two bands, we can get the Nernst effect

$$e_y = S(\frac{\alpha^h_{xy} + \alpha^e_{xy}}{\alpha^h_{xx} + \alpha^e_{xx}} - \frac{\sigma^h_{xy} + \sigma^e_{xy}}{\sigma^h_{xx} + \sigma^e_{xx}}) \tag{2.66}$$

In this case, the Nernst effect can be quite large depending on the relative Peltier and electrical conductivities of the two bands. Even in the case of compensated bands, $\sigma^h_{xy} = -\sigma^e_{xy}$, only the second term on the right hand side of Eq. 2.66 vanishes. The first term does not vanish since α_{xy} has the same sign for both bands.

Chapter 3

Samples and Experimental Setup

In this chapter, the growth and characterization procedures of films of the electron-doped cuprates are described briefly. Experimental setups including Hall effect, Nernst effect and thermoelectric effect and measurement procedures will be shown in detail.

3.1 Film fabrication and characterization

Thin films of $Pr_{2-x}Ce_xCuO_{4-\delta}$ ($0.05 \leq x \leq 0.19$) were grown with a pulsed laser deposition (PLD) technique. This technique consists of directing a high energy density laser beam onto a stoichiometric target inside of a vacuum chamber with a controlled gas environment. The interaction between the laser and the target creates a plasma which impinges on a crystalline oriented substrate held at high temperatures. The plasma maintains the elemental proportions of the target and deposits onto the single crystalline substrate. Under the right conditions, the deposition results in an epitaxial thin film with the same composition as the target.

The target used for depositions was prepared with a solid state process. High purity powders of Pr_6O_{11}, CuO and CeO_2, were dried and weighed out to ensure an accurate proportion of powders. The powders were then mixed thoroughly using an agate pestle and mortar. After the even mixing, the mixture was heated for 24

hours at 900°C in a furnace with an air environment. After that, the mixture was cooled down to room temperature and then ground again. To ensure a thorough solid reaction, this process has to be repeated for 2 or 3 times. After the reheating, the mixture is again ground into powder and the powder is compressed into a pellet which is sintered at high temperature of 1050°C for 24 hours. This procedure results in a polycrystalline, non-superconducting pellet sample which is used a target in the film deposition.

A schematic of the chamber used for the pulsed laser deposition is shown in Fig. 3.1. The films were grown on (100) oriented $SrTiO_3$ (STO) substrates. These substrates have a close lattice match with the in-plane lattice parameters of PCCO and the films turn out to be c-axis oriented. The vacuum chamber used for depositions is prepared by cleaning the substrate heater and the target before every deposition. The substrates were carefully cleaned with organic liquid solvents(acetone, methanol, and isopropanol) in a sonic washer before the deposition. The cleaned substrates then were affixed on the heater with silver paste. The chamber was evacuated until the pressure reached 1×10^{-5} Torr. A preablation procedure is needed to clean the surface of the target. The conditions for the preablation are identical to the deposition conditions except for the duration (3-5 minutes), the temperature of the substrate, T_s ($T_s \leq 100$°C), and a shutter is used to prevent any deposition onto the substrate. The gas environment used is 230 mTorr N_2O at a flow rate of 100 standard cubic centimeters per minute (sccm). The frequency of the laser is 10 Hz (repetition frequnecy). After the preablation, N_2O gas flow is stopped and the chamber is re-evacuated. Note that before the heater is restarted to ramp up

the temperature, the shutter should be flipped up, otherwise, the substrate would be contaminated at high temperature. Before deposition, the temperature of the substrate is raised to 800°C at a rate of 50°C/minute in vacuum. At temperature, the N_2O environment is reintroduced at the same level as the preablation pressure. The deposition conditions vary somewhat depending on the Ce doping and film thickness. The thickness of films was controlled by deposition time and laser energy density. For the films used in this thesis, the thickness is about 3000Å, the deposition time is 15 minutes and the laser energy density is about 1.8 J/cm^2 (for a detailed description, see Refs. [69, 70]).

After deposition, the film is annealed in order to remove oxygen. The substrate temperature is lowered to 720°C at the natural rate of the heater ($\simeq$ 30 seconds), while the N_2O pressure is maintained at 230 mTorr. At temperature, the pressure is reduced to below 10^{-4} torr. The starting time of the annealing is monitored once this pressure is reached. During the annealing, to avoid film decomposition, the annealing pressure is controlled above 3×10^{-5} torr. The optimized annealing time determined by T_c and decomposition depends on the Ce doping (with same thickness) and it increases approximately linearly with doping. For the underdoped x=0.13 (3000 Å), the annealing time is about 12-13 minutes and it is about 18-19 minutes for the highly overdoped x=0.19 film. After the annealing, the heater was turned off but the vacuum was kept at the same pressure until the temperature dropd below 300 °C. Once the temperature is close to room temperature, the film is ready to remove.

The films were characterized with the following standard techniques. For a

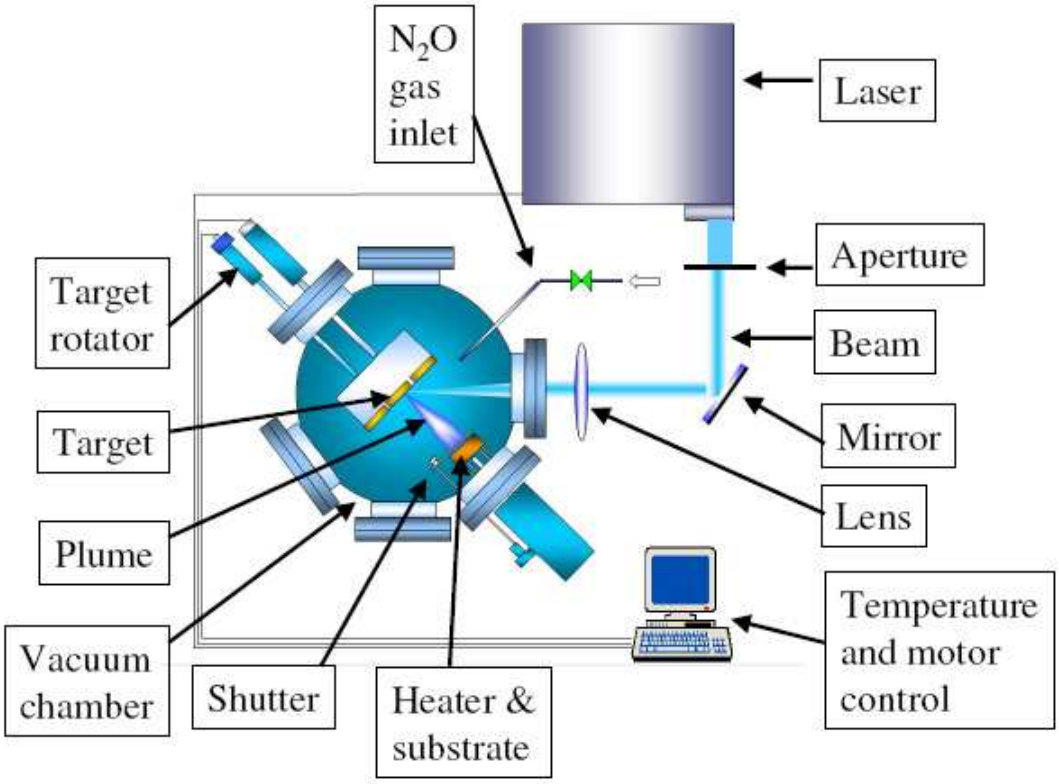

Figure 3.1: Schematic for PLD film growth. The frequently adjusted/maintained components are labeled.

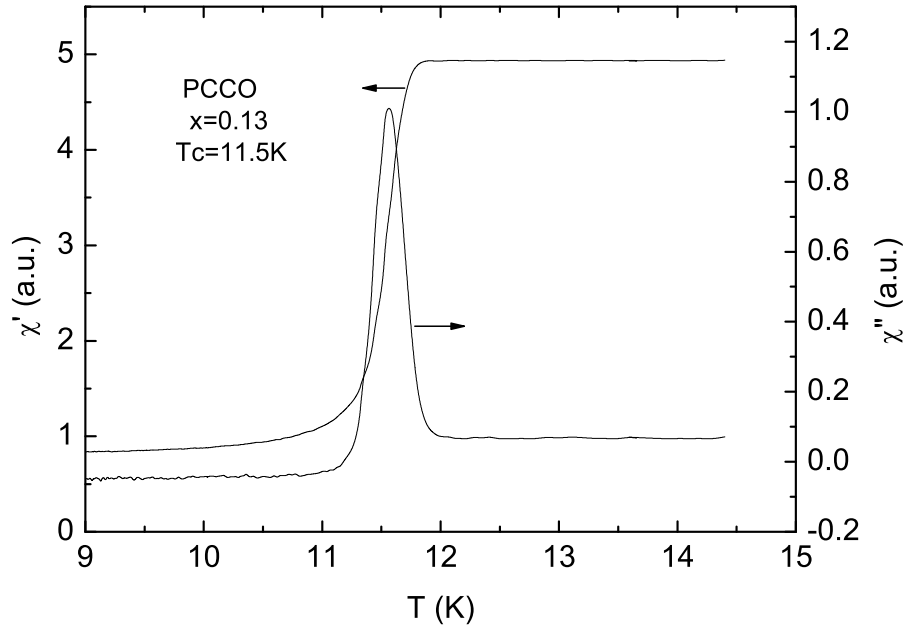

Figure 3.2: AC susceptibility of an underdoped PCCO x=0.13 film. The T_c is determined from the peak in χ'' and the transition width ΔT_c is determined from the full width at half maximum in χ''.

fresh film, optical microscopy was used to check for decomposition or pinholes due to the high temperature annealing process. For good films, we require less than 6-10 of any feature within a 200 μm field of view. Pinholes of about 1 μm size in the film form from dust on the substrate during deposition. Decomposition, black dots typically surrounding transparent "holes", arise from the chemical deterioration of the film during the growth/annealing process. This primarily occurs in the optimal and overdoped films and it can be reduced by ensuring a clean substrate and minimizing the duration time at high temperatures.

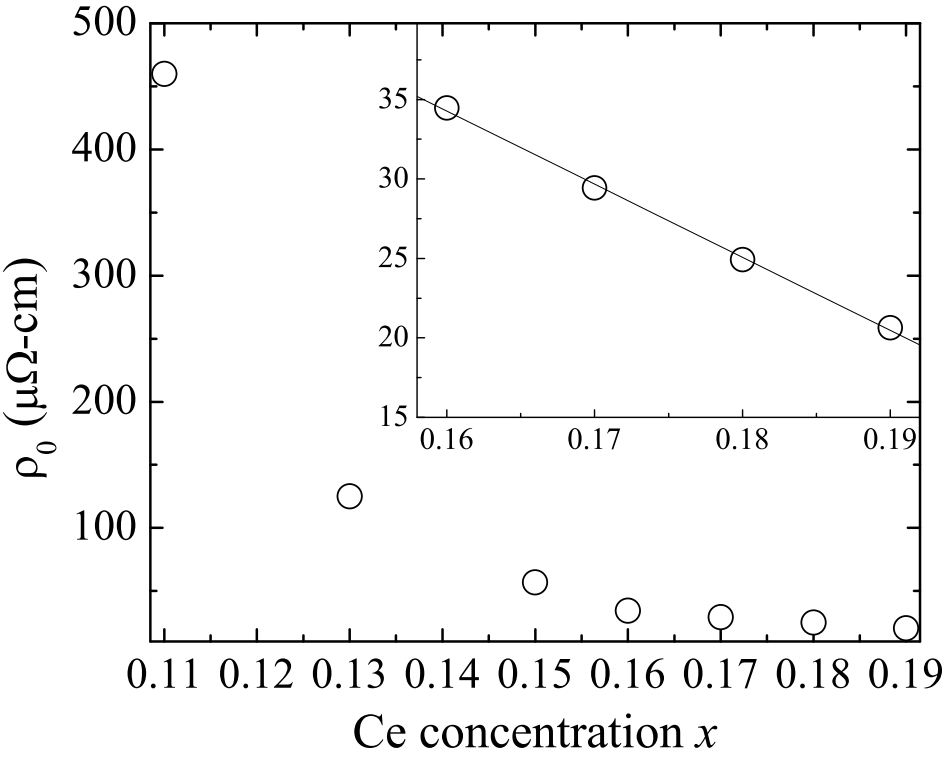

Figure 3.3: Doping dependence of the residual resistivity of PCCO films. Inset shows the data for the overdoped films.

An AC susceptibility probe was used to determinate the T_c of the films. Fig. 3.2 shows a typical AC susceptibility measurement and T_c is determined by the temperature at which the imaginary part of the susceptibility has a peak. For a film with reasonable T_c (i.e., less than 1 K from the highest T_c that has been obtained at that doping), a resistivity measurement was performed on a patterned film to check the normal state residual resistivity (normal state resistivity was shown in Fig. 1.9 for $H>H_{c2}$). The magnitude of the residual resistivity is a measure of the relative disorder in the film and hence its quality. Fig. 3.3 shows the Ce doping dependence of the zero temperature residual resistivity of the films under optimized growth condition. For the underdoped films, because of the low temperature resistivity upturn, the zero temperature residual resistivity is determined by extrapolating the high temperature quadratic curve to T=0. The thickness of the films was usually determined by a Rutherford back scattering (RBS) method. The channelling in RBS is also an indication of the quality of the films. Better films usually have higher channelling, indicating fewer defects and less disorder. For the films that we used for the experiments, the RBS results give a 10-20% backscattering fraction, suggesting the films were of high quality.

X-ray diffraction (XRD) was performed on films grown with new targets. A typical XRD pattern is given in Fig. 3.4. Fig. 3.4 shows that the film is dominantly c-axis oriented (c-axis peaks are labelled) single phase. Note that additional peaks are frequently observed, which are labeled (110) and (220). These peaks are attributed to misaligned PCCO grains in the film and occur during non-optimal growth. They are attributed to these grains rather than an impurity phase of $(Pr,Ce)_2O_{3.5}$ because

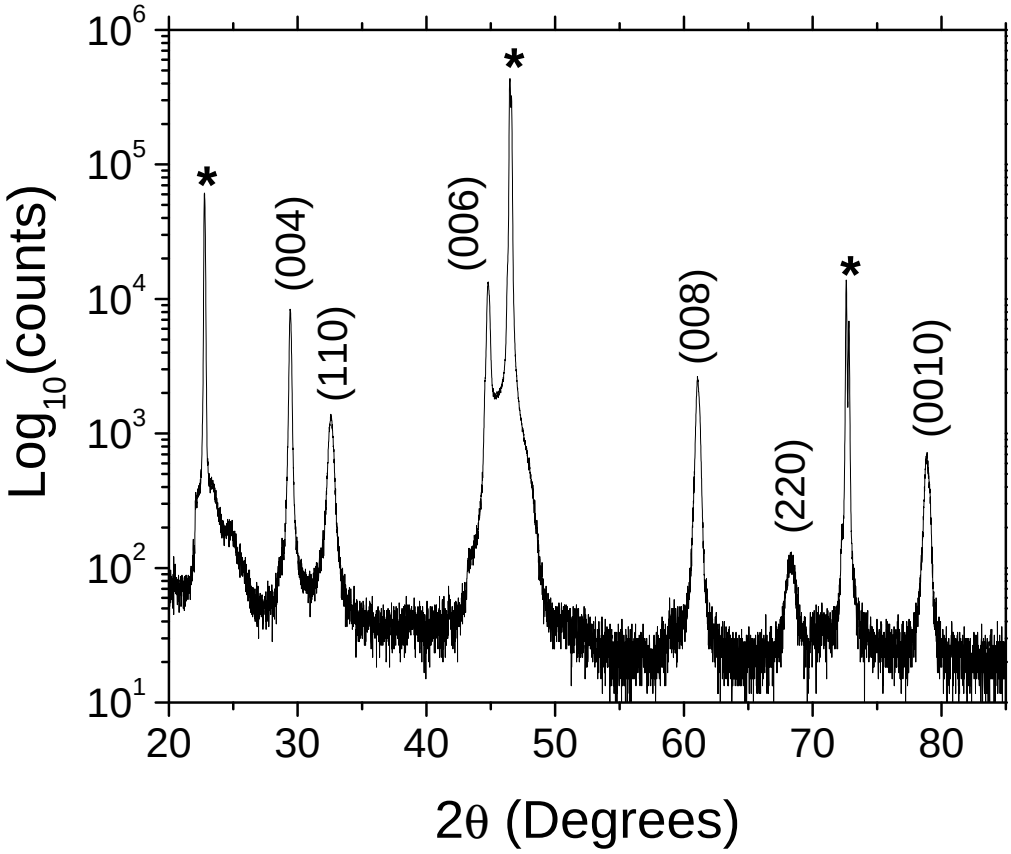

Figure 3.4: X-ray diffraction pattern for an $x = 0.17$ PCCO thin film deposited on an $SrTiO_3$ substrate. The substrate peaks are identified by an asterisk ($\star$). The other peaks are from the PCCO thin film and indicate a c-axis orientation. The anomalous peaks labeled (110) and (220) are discussed in the text.

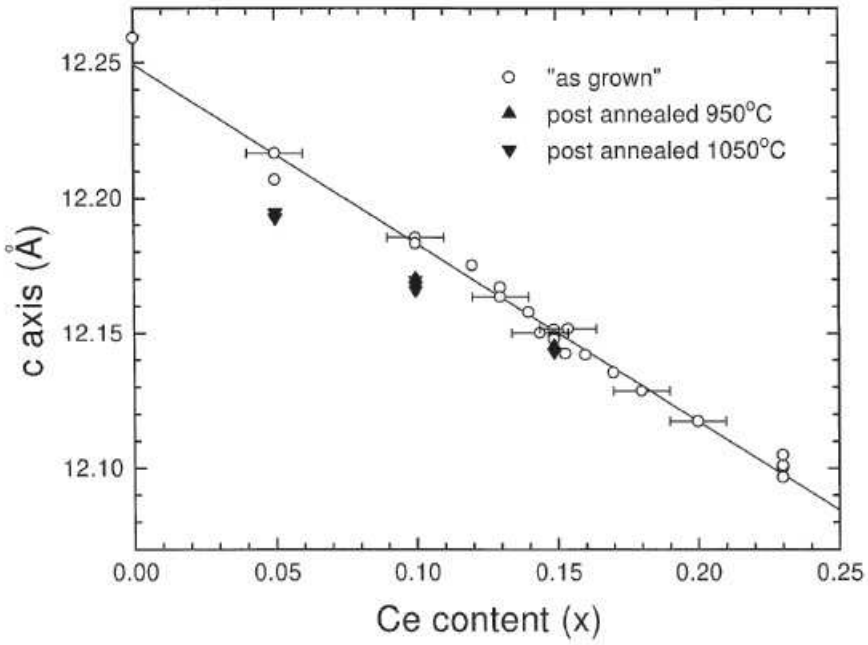

Figure 3.5: c-axis lattice parameter of $Pr_{2-x}Ce_xCuO_4$ films before and after post-deposition annealing (from Ref. [69]).

the latter phase does not form under normal solid state reaction conditions and the peaks are also observed in undoped PCO. Recent neutron scattering and X-ray measurements [71] found some small angle peaks from an impurity phase which develops with annealing in an electron-doped $Pr_{0.88}LaCe_{0.12}CuO_4$ crystal. It was argued that with annealing the Cu ions move to the ∼1% vacancies at Cu site in the CuO_2 planes and as a result an impurity phase of RE_2O_3 forms. We note that in our films, we did not observe any impurity peaks at low angle (<20°) in either as grown or oxygen-reduced films.

Lattice parameters can be obtained from XRD and the c-axis lattice parameter decreases linearly with Ce content, as shown in Fig. 3.5. The magnitude of the c-axis

lattice parameter as often used to determine the actual Ce content in the film.

3.2 Film patterning

For measurements of the Hall effect and resistivity, the thin films are patterned into Hall bar geometries (e.g. see Fig. 3.6). Mechanical masks and ion-mill techniques were used to pattern large size (10×5 mm^2) films. A stainless steel mechanical mask was used to cover the parts of the film (i.e. the Hall bar) and the high-energy ions in the ion-mill etch away the parts of the film which are exposed to the beam.

For films of smaller size that are required in experiments with limited sample space, such as electrical transport measurements in pulsed magnetic field, a photolithography technique is adapted to pattern them into a standard Hall bar. In the photolithography process, an organic photoresist (S1813) covers the films and functions as a mask. First, the photoresist was evenly distributed on a PCCO film using a high-speed spinner. The thickness of the photoresist is controlled by the rotating speed of the spinner. It is about 1 μm at the speed of 5000 rpm. Once the film is covered evenly with photoresist, it is baked on a small furnace at 90 °C for one minute to enhance the hardness of the photoresist. After the baking, the film is aligned under a specially designed mask (a chromium Hall bar pattern on a piece of glass) for UV light exposure. The photoresist in the area that is not covered by the mask will be exposed to the UV light, and the UV light breaks the chemical bonds of the photoresist compound. The exposure time is about 12 seconds and then the

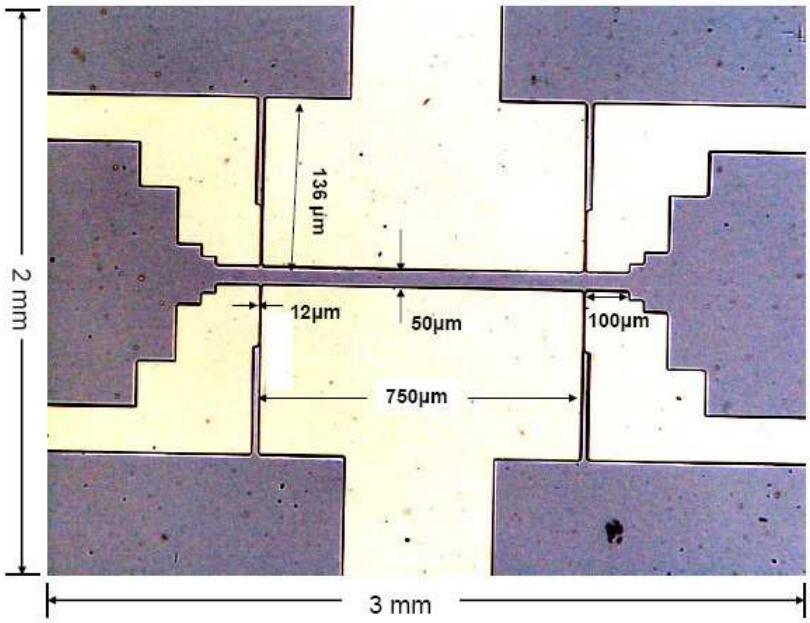

Figure 3.6: A photograph of a standard six-probe Hall bar pattern. Darker area is film.

films is ready for development to remove the exposed photoresist. The development is performed in certain solvent (CD 30) for about 7-10 seconds. The photoresist of the exposed area will be dissolved and protected parts leave a Hall bar pattern on the film. After the photolithography process, an Ion-mill is used to etch away the parts of the film without photoresist. A picture of a patterned film used for the high-field experiments in the National High Magnetic Lab (NHMFL) at Los Alamos is shown in Fig. 3.6. The size of the patterned film is 2×3 mm^2.

For the electrical transport experiments on the films, thin gold wires (diameter of 2 mil for the regular films and 1 mil for the small size films used in high-field experiments) are soldered with Ag-In mixture (1:8) on the contact pads. The use of low melting point Ag-In mixture is necessary to protect the films from heat

damage. The contact resistance of the electrodes and PCCO is small (about a few Ohms at 300 K), and evaporating gold on the PCCO films is not necessary in general. However, for the Nernst effect measurements presented in this thesis, gold was evaporated on the contact pads of the films before the Ag-In soldering is used, since this method reduces the contact resistance significantly (less than 1 Ohm).

3.3 Experimental setups

Two systems were used for the experiments reported in this thesis: an Oxford Research cryostat with a home-made probe and related electronics and a Quantum Design Physical Property Measurement System (PPMS). The Oxford cryostat has a 9 T superconducting magnet, as shown schematically in the left panel of Fig. 3.7, in which the magnetic field could be increased up to 11 T by pumping on the lambda plate. Cooling below 4.2K is achieved by collecting liquid helium into the variable temperature insert and reducing the pressure above it by pumping with a mechanical pump.

The probe for the Oxford cryostat system is a home-made apparatus with changeable sample stages for multiple measurements. Fig. 3.7 shows a schematic probe head. Several sample stages were designed for different transport experiments [resistivity (Hall effect), thermopower and Nernst effect]. For each of these experiments, the sample stage can be replaced with a stage designed for the particular experiment (details will be discussed later). The sample stage is attached to the probe head by two multipin connectors and is tightened by two screws to ensure

good thermal contact (N-grease is also used). The probe temperature is achieved by a resistive heater that wound on the probe head. The system temperature is controlled by a Lakeshore temperature controller (model 93-CA or 340) and is monitored by a Lakeshore Cernox thermometer (cx-1050)that mounted on the probe head. Electronics such as Keithley 2182 nanovoltmeter and 2001 multimeter (with a 1801 preamplifier), and Keithley 224 current source are utilized for the various experiments performed in this system. For each different experiment a Labview program was designed to control the magnet, temperature and electronic devices (programming charts will be shown next). Experimental data was simultaneously collected and recorded into the computer.

The other system we used is the Quantum Design Physical Property Measurement System (PPMS). This system has a self-contained microprocessor-controlled device (Module 6000) which integrates temperature controlling, measurements operation, data collection and magnetic field control. The integrated measurement applications include electrical transport (resistivity and Hall effect), heat capacity and magnetometry (AC susceptibility, torque magnetometer). Each measurement option has a removable sample puck, which goes into the sample space and is electrically connected with multipin connectors at the bottom of a sample space insert tube.

For the Nernst effect and thermopower measurements, which are not options of the PPMS system, blank sample pucks were modified and external electronics were utilized. Temperature and magnetic field were controlled through the PPMS electronics and experimental data was collected via external instruments. Labview

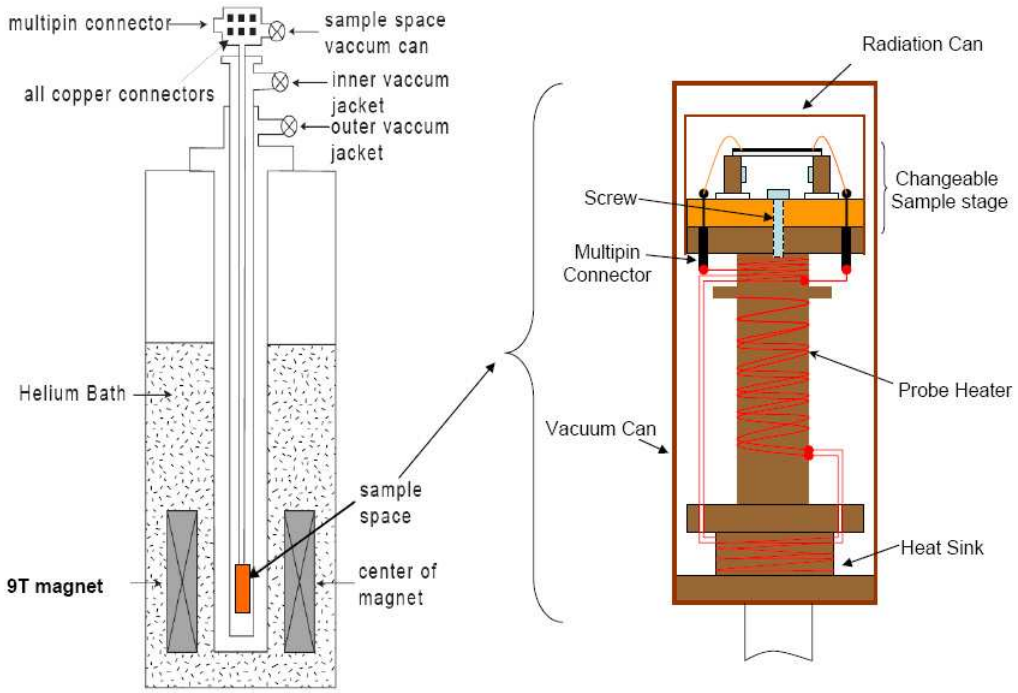

Figure 3.7: Schematics of a cryostat with a superconducting magnet (left) and a home-made probe-head (right).

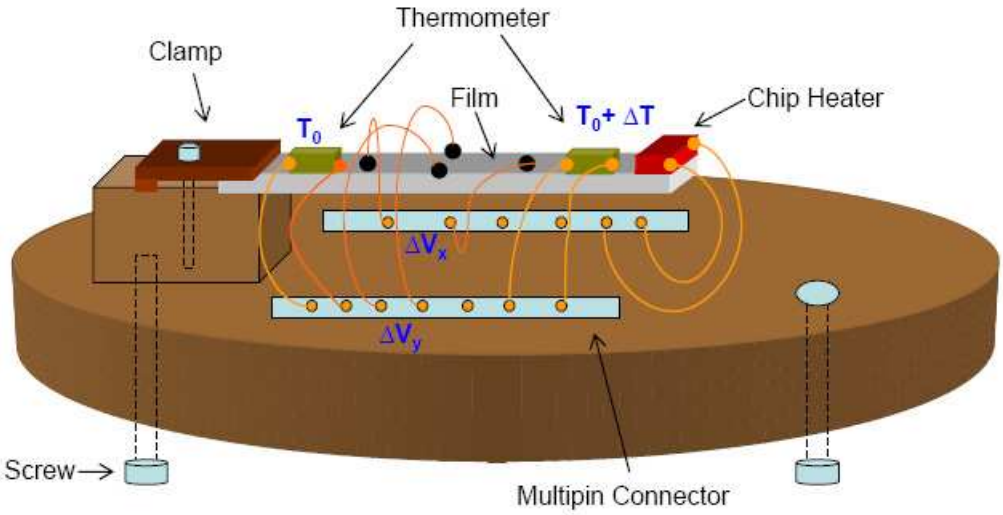

Figure 3.8: A schematic of a sample stage for the Nernst effect measurement.

program were designed to control the PPMS system (temperature and magnetic field) and external devices.

3.3.1 Nernst effect measurement

For the Nernst effect measurements performed in the Oxford cryostat and PPMS the sample stages are similar. The Nernst sample stage for the home-made probe is shown in Fig. 3.8. The stage was mounted on the probe head and it was tightened by two brass screws and N-grease was used to ensure the thermal contact. A radiation can was used to cover the stage to reduce temperature fluctuation from thermal radiation (see Fig. 3.7). The stage for the PPMS system takes advantage of the electrodes on the Quantum Design blank pucks, therefore, no multipin connector is needed.

The Nernst effect measurement can be done in two ways: magnetic field sweep

at fixed temperature or temperature sweep at a constant magnetic field. The former method was considered more accurate, since in the temperature sweep measurement the thermal relaxation time of the temperature gradient is usually large. However, this temperature response problem can be solved if we begin the data collection after the system temperature and temperature gradient are stable. This steady state measurement procedure, however, takes a much longer time than sweeping the temperature.

The Nernst effect measurement procedure for the field sweep method is rather straightforward. As seen in Fig. 3.8, the sample is affixed on the copper block (heat sink) with a mechanical clamp to ensure good thermal contact between the sample and the heat sink (a small amount of N-grease was also used). This is crucial for measurements on thin films with a large substrate, which is a good thermal conductor. The temperature gradient is difficult to obtain without the mechanical clamp. A small chip resistor (about 5 KΩ) is used as a heater attached with GE vanish on the free end of the film. Heating is achieved by applying a constant current to the resistor.

The measurement was automated by a computer with a Labview program. The programming flow procedure for the field sweep Nernst effect measurement is shown in Fig. 3.9. Before setting a temperature, the magnetic field is set at the highest field. The system temperature is then well stabilized by a Lakeshore temperature controller using the thermometer attached on the probe. With the system temperature set, a gradually increasing current is applied to the chip heater and the temperature gradient is monitored simultaneously. Once the desired gradient

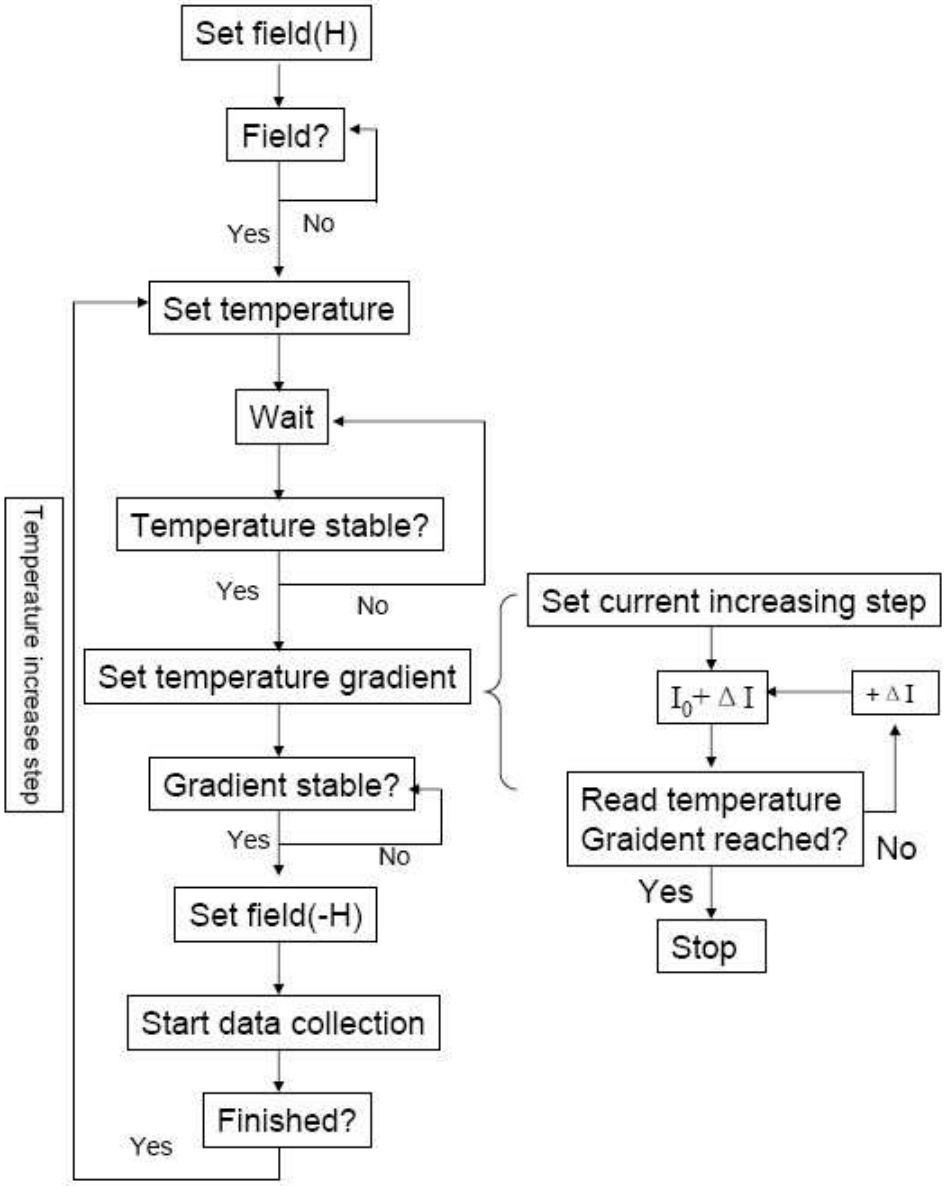

Figure 3.9: A Nernst effect measurement programming procedure.

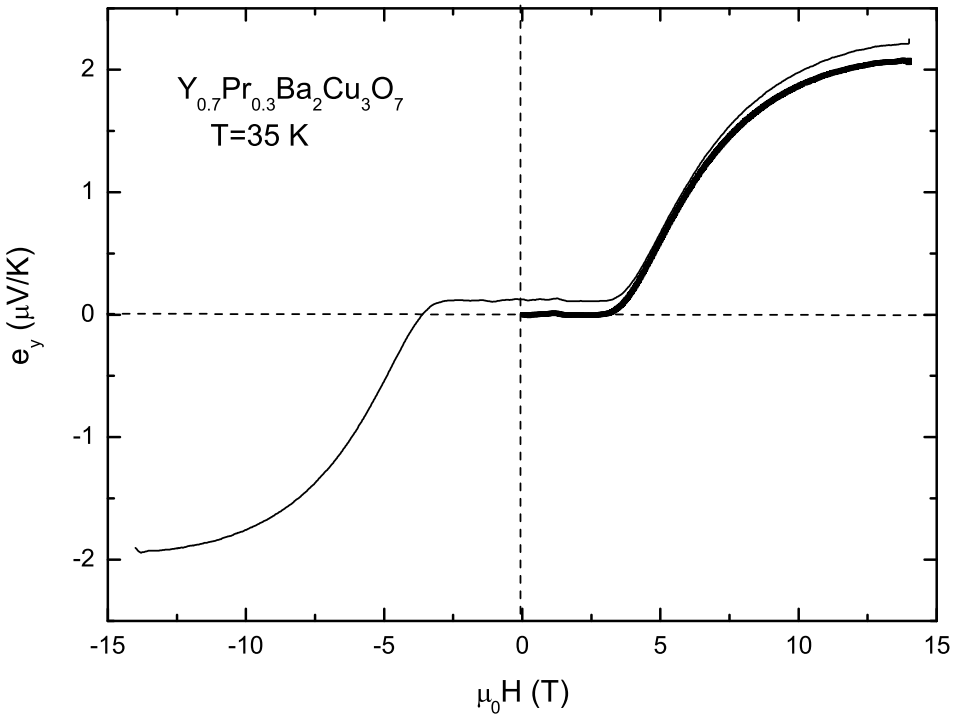

Figure 3.10: Nernst signal of a Pr-doped YBCO film ($T_c \sim 70$ K) at T=35 K. The thin line is the raw data and the thick line is the Nernst signal after subtraction.

is reached, the current stops increasing and is set at a constant value. A short time (several minutes) is needed for the equilibrium of the entire system. After that, the magnetic field sweep is started from the highest field at a slow rate (30 oe/s). During the field sweep, the Nernst signal and magnetic field are recorded on the computer and the temperature gradient is monitored with two tiny bare chip Cernox thermometer and also recorded for later data analysis. The Nernst voltage is read during the field sweep from one polarity to another by a Keithley 2001 multimeter with a 1801 preamplifier. The net Nernst voltage $\triangle V_y$ then is obtained by subtracting the negative field data from the positive field data, i.e., $\triangle V_y = [V_y(H^+) - V_y(H^-)]/2$, to reduce any possible thermopower contribution. The Nernst signal e_y then is $\triangle V_y / \triangle T$. In Fig. 3.10, a Nernst curve for a Pr-doped YBCO film is shown to illustrate this procedure. The thick line in the figure is the net Nernst signal after subtraction.

For the temperature sweep method, the procedure is similar to the thermopower experiment performed on this one-heater-two-thermometer setup as shown in Fig. 3.8. The detailed description of this method will be discussed next.

3.3.2 Thermoelectric power measurement

The thermopower experiment is straightforward but not trivial. Fig. 3.11 is a schematic of the measurement. With a temperature gradient, the longitudinal thermoelectric voltage is induced and the overall thermopower is given by $S = \triangle V_x / \triangle T$, which includes the contributions from both sample and electrode wire.

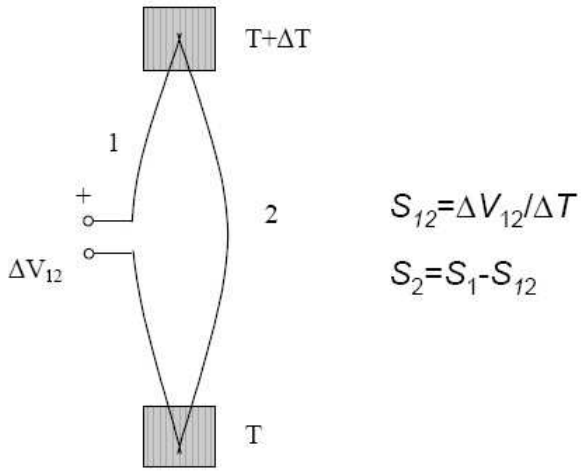

Figure 3.11: A schematic of the thermopower measurement. S_{12} is the overall thermopower, S_1 and S_2 are thermopowers of the lead wire and sample respectively.

To get the thermopower of the sample, one has to subtract the absolute thermopower of the contact wire, which can be obtained by measuring the thermopower of a circuit with the wire of Pb (absolute S known) or a superconductor (S=0 for T<T_c).

There are several ways to do the measurement. One popular way is the so called one-heater-two thermometer method. The experimental scheme is similar to the Nernst effect measurement as described before. One simply builds up a steady temperature gradient and measures the longitudinal voltage along the sample at each average temperature. The disadvantage of this steady method is that since the thermopower measurement is a two-probe measurement, the contact potential between the voltage wires and the electrodes on the sample is not cancellable, i.e., the offset voltage at zero temperature gradient remains when the temperature gradient is set. This contact potential can be reduced if one can make the contact resistance

smaller. For materials with large thermopower this contact contribution is negligible. However, for materials with a small thermopower, such as the overdoped electron-doped cuprates, it is quite important to eliminate the contact contribution. To solve this problem without changing the experimental setup, we adopted a method of slowly increasing the temperature gradient and measuring the thermoelectric voltage at each gradient. The thermopower of the sample is taken as the the slope of the thermoelectric voltage versus temperature gradient curve (see Fig. 3.12). In this way, the background signal which appears as an offset in the thermoelectric voltage-gradient curve will not be important.

A program flow chart of this measurement procedure is shown in Fig. 3.12. As mentioned before, this procedure can also be applied to the Nernst effect measurement. This is the slow temperature sweep method mentioned in Section 3.3.1. For this temperature sweep Nernst effect measurement it is also necessary to perform the measurement in two field polarities to eliminate any thermopower contribution from possible misalignment of the Nernst electrodes.

Another method often used to accurately measure the thermopower is the two-heater-two-thermometer method. The setup consists of two copper blocks with two chip resistor heaters attached. As shown in Fig. 3.13, the sample is mounted on top of the copper blocks and GE vanish is used to ensure good thermal contact. Two bare chip Cernox thermometers are mounted on top of the two ends of the sample. The measurement procedure is analogous to the four probe resistivity measurement, where the heat flow generated by the temperature gradient acts as an electric current. To cancel out the contact potential, the heat flow direction is switched by turning off

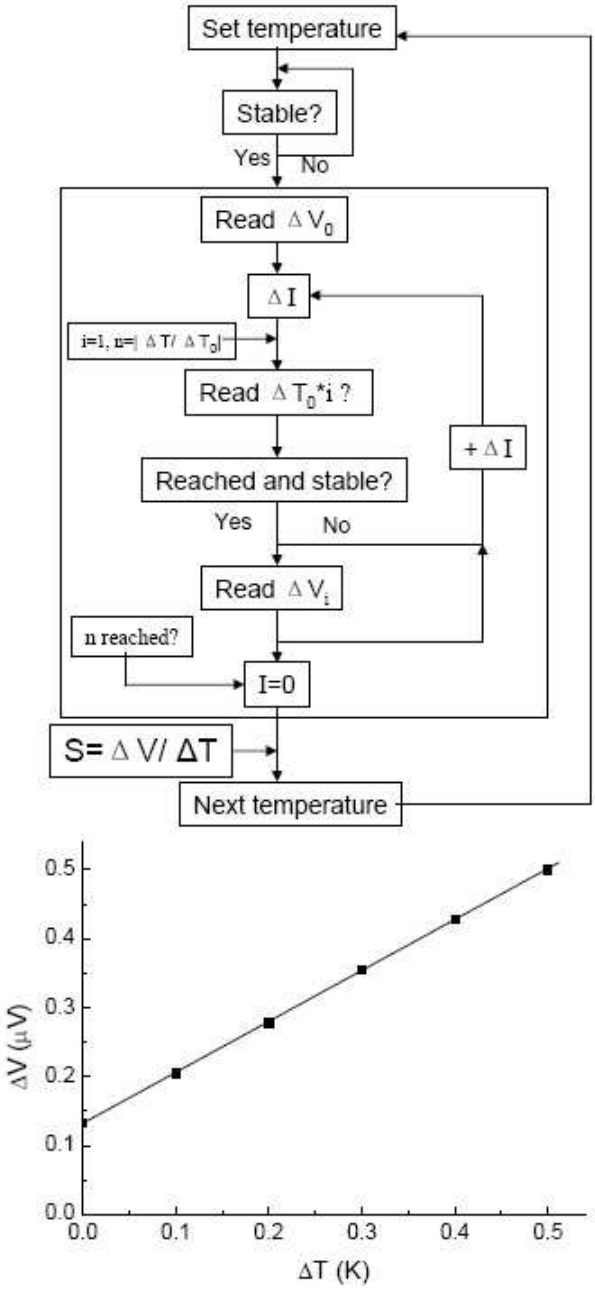

Figure 3.12: Program flow chart of the one-heater-two-thermometer thermopower and Nernst effect measurements in a temperature sweeping method. $\triangle V_0$ is the zero temperature gradient offset voltage. $\triangle I$ is the current increasing step. $\triangle T_0$ is the temperature gradient step.

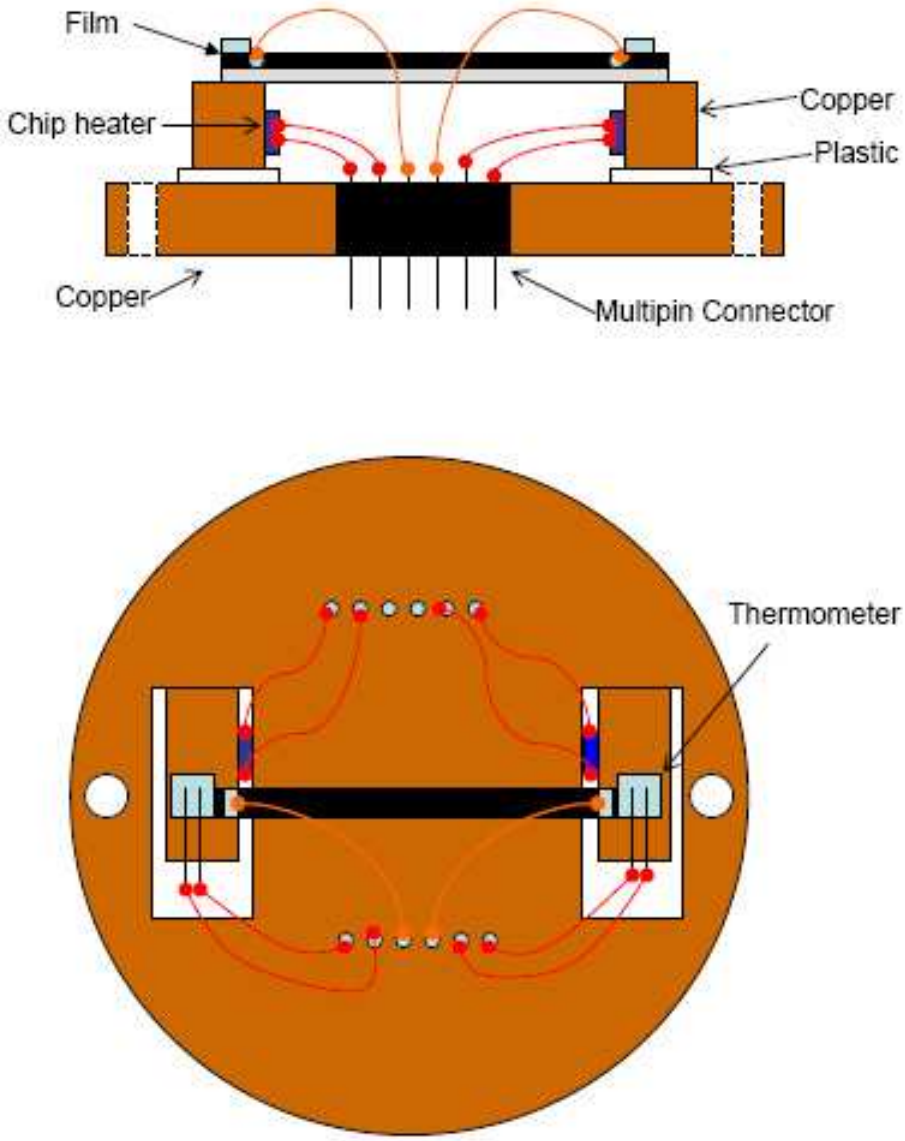

Figure 3.13: A schematic of a sample stage for the thermopower measurement by switching the direction of the temperature gradient.

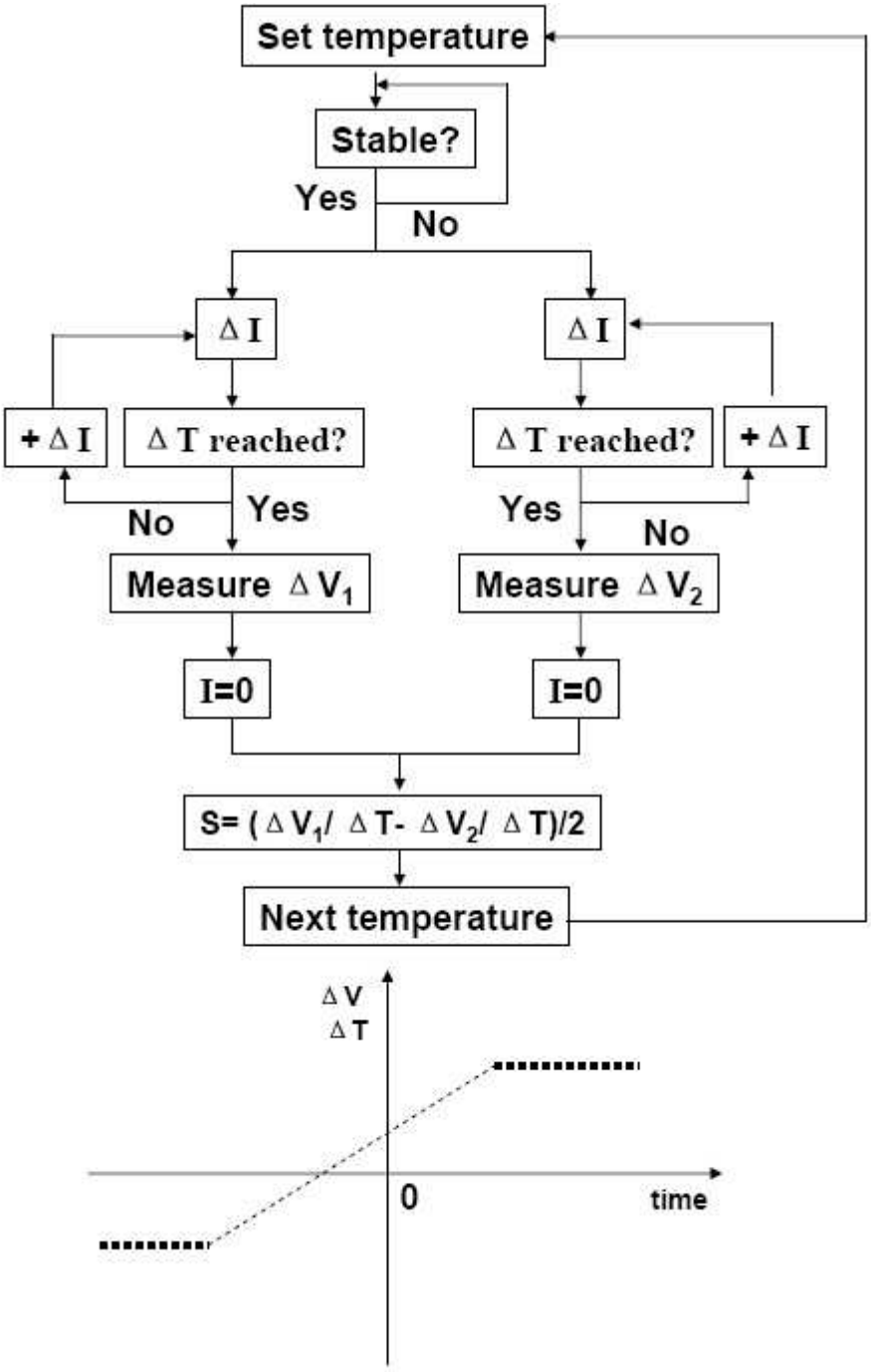

Figure 3.14: Program flow chart of the two-heater-two-thermometer thermopower measurement.

the heater on one copper block and turning on the heater on the opposite side. Since the thermopower switches sign if the temperature gradient direction is reversed, the net thermopower then is taken by subtracting one from another and divided by 2, i.e., $S = [S(+\triangle T) - S(-\triangle T)]/2$. To reduce systemic errors, the thermoelectric voltage is read many times and an average is taken for each temperature gradient direction. A computer program flow chart for this switching temperature gradient procedure is shown in Fig. 3.14. The thermopower experiments on PCCO films presented in this thesis were performed with this method.

As we have shown before, to obtain the absolute thermopower of the sample, one has to subtract the thermopower contribution from the lead wire. In the thermopower experiments on PCCO films, we used phosphor bronze wires as the voltage leads. These wires have an extremely small thermopower (less than 30 nV/K) even at high magnetic field [72].

3.3.3 Resistivity and Hall effect measurements in pulsed magnetic field

The high-field resistivity and Hall effect experiments on PCCO films were carried out in the National High Magnetic Field Laboratory (NHMFL) at Los Alamos National Laboratory (LANL). The 60 T pulsed magnetic field is generated by a capacitor driven magnet. The duration of the field is about 100 ms. The field versus time profile is shown in Fig. 3.15. Due to the extremely short pulse of the magnetic field, transport experiments can be done only with a high-frequency (about 100

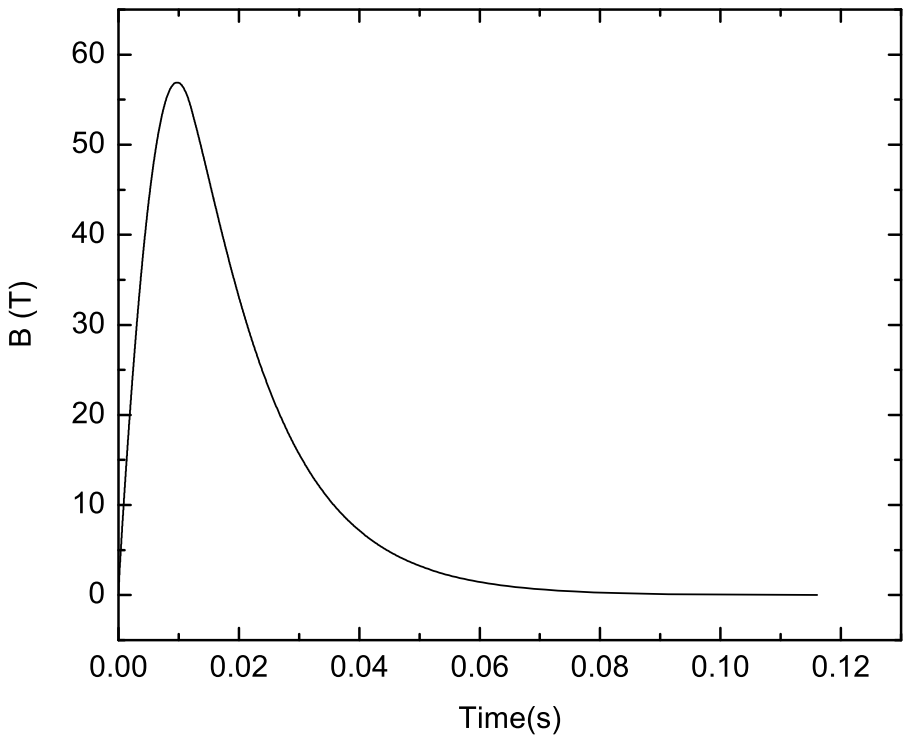

Figure 3.15: A pulsed magnetic field curve.

KHz) AC method [73]. Resistance and Hall voltages were recorded simultaneously by a computer with a home-made lock-in designed by NHMFL. The data was collected during the entire field cycle shown in Fig. 3.15. To obtain the Hall resistivity, the Hall voltage has to be measured again in the reversed field orientation.

Due to the large EMF generated by the pulsed field, a small sample is required to reduce eddy current heating. The PCCO films measured in the 60 T pulsed magnetic field were patterned into standard six-probe Hall bar and cut from a larger size film (10×5 mm^2). The size of patterned film is about 2×3 mm^2 as shown in Fig. 3.6. The lead wires for the high-field experiments are gold wires with 1 μm diameter. The wires were soldered on the contact pads of the films with Ag-In under a microscope. The system temperature is controlled by a Lakeshore 340 controller.

Patterned thin films, compared to single crystals, have advantages for the high-field experiments due to their larger resistance. Therefore, a smaller AC current is needed to achieve good measurement signal. This is helpful to avoid the heating effect from the large current. To check the eddy current heating effect, the data with the field ramping up and down are compared. If the two curves overlap on each other, then the eddy heating is negligible.

The parallel critical field experiments on PCCO films were performed on a stage with a perpendicular block attached on the horizontal surface of the probe, and the films were glued on the perpendicular block. To ensure that the field is parallel to the ab-plane, the entire procedure was done under a microscope and several measurements in field were recorded to determine the optimal orientation.

Chapter 4

Normal State Thermopower in $Pr_{2-x}Ce_xCuO_{4-\delta}$

4.1 Introduction

The existence of a quantum phase transition at a doping under the superconducting dome in high-T_c superconductors is still controversial. Evidence for a quantum critical point has been given for hole-doped cuprates [74, 75, 76] but the T=0 normal state is difficult to access because of the large critical field (H_{c2}). Electron-doped cuprates have a relatively low H_{c2} and several studies have suggested that a quantum phase transition exists in those cuprates. As we have shown in Chapter 1, electrical transport [49] on electron-doped $Pr_{2-x}Ce_xCuO_{4-\delta}$(PCCO) shows a dramatic change of Hall coefficient around doping x_c=0.16 (see Fig. 1.5), which indicates a Fermi surface rearrangement at this critical doping. Optical conductivity experiments [57] revealed that a density-wave-like gap exists at finite temperatures below the critical doping x_c and vanishes when $x \geq x_c$. Neutron scattering experiments [35, 37] on $Nd_{2-x}Ce_xCuO_{4-\delta}$ (NCCO) found antiferromagnetism as the ground state below the critical doping while no long range magnetic order was observed above x_c. Other suggestive evidence [56] comes from the observation of a low temperature normal state insulator to metal crossover as a function of doping, and the disappearance of negative spin magnetoresistance at a critical doping [55]. All these experiments strongly suggest that an antiferromagnetic (AFM) to paramag-

netic quantum phase transition (QPT) occurs under the superconducting dome in the electron-doped cuprates.

The quantum phase transition in electron-doped cuprates is believed to be associated with a spin density wave (SDW) induced Fermi surface reconstruction [see chapter 5 and Ref. [58, 59] for details]. ARPES experiments [50] on NCCO reveal a small electron-like pocket at $(\pi, 0)$ in the underdoped region and both electron- and hole-like Fermi pockets near optimal doping. This interesting feature is thought to arise as a result of the SDW instability that fractures the conduction band into two different parts [58] (Fig. 5.1 in chapter 5). If one continues to increase the doping (above x_c), the weakening of the spin density wave leads to a large hole-like Fermi pocket centered at (π, π) in the overdoped region [51, 58].

Nevertheless, the presence of a quantum critical point (QCP) under the superconducting dome in electron-doped cuprates is still quite controversial [38]. Other experimental probes of the critical region are needed. In this chapter, we present a systematic study of the magnetic field driven normal state thermopower on PCCO films. We find a doping dependence similar to that seen in the low temperature normal state Hall effect measurements [49]. From a simple free electron model comparison of these two quantities, we find a strikingly similar behavior of the effective number of carriers. This strongly suggests that a quantum phase transition takes place near x=0.16 in PCCO.

4.2 Experiments and results

High quality PCCO films with thickness about 2500-3000Å were fabricated by pulsed laser deposition on $SrTiO_3$ substrates (10×5 mm^2). Detailed information can be found in chapter 2 and Ref. [69, 70]. The films were characterized by AC susceptibility, resistivity measurements and Rutherford Back Scattering (RBS). The minimum-channeling yield obtained was 10% to 20% indicating a good epitaxial growth. A sharp transition ($\triangle T_c$ <1 K) indicates that our films are of high quality. We note that since the oxygen content has an influence on both the superconducting and normal state properties of the material [46], we optimized the annealing process for each Ce concentration as in Ref. [49]. The sharp transition, low residual resistivity and the Hall coefficient are exactly the same as the previous report [49]. Since the exact content of oxygen cannot be determined in films, we use the low temperature values of the Hall coefficient and Ce content to determine the temperature versus doping phase diagram.

High resolution thermopower is measured using a steady state method by switching the temperature gradient as described in chapter 3. Due to the lower upper critical field (H_{c2}) of electron-doped cuprates, a magnetic field of 9 T (H$\|$c) is enough to suppress the superconductivity for all the dopings. This enables us to investigate the low temperature normal state thermopower in PCCO. A low temperature resistivity upturn is observed for doping below x=0.16 (Fig. 1.9), which suggests a possible insulator to metal crossover as a function of doping [47].

Low temperature thermopower measurements were performed on the PCCO

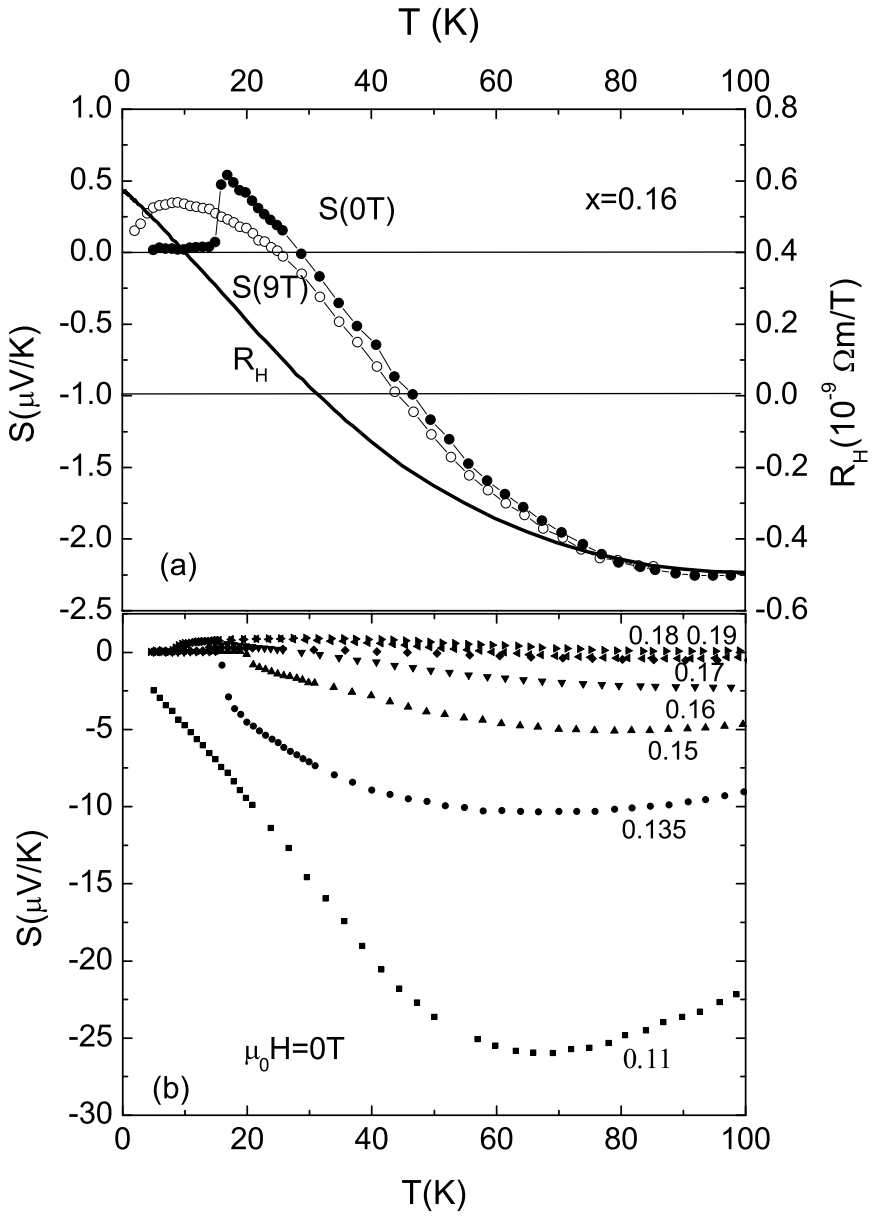

Figure 4.1: (a) Temperature dependence of the zero-field thermopower of an over-doped x=0.16 film (solid blue circle) and the normal state themopower measured at μ_0H=9 T (open circle). The temperature dependence of the normal state Hall coefficient of this film is shown as solid line. (b) Zero-field thermopower as a function of temperature (T<100 K) for all the doped PCCO films.

films doped from x=0.11 to 0.19. For the superconducting films in zero field, a sharp superconducting transition is clearly seen in the thermopower. Shown in Fig. 4.1(a) is the thermopower (S) of an overdoped x=0.16 film (T_c=16.5 K) as a function of temperature. Our high resolution thermopower setup enables us to observe small changes of signal. As the sample is cooling down to the superconducting state, S=0, a small change of $\triangle$S=0.5 μV/K is easily detectable. This indicates a better sensitivity than the previous one-heater-two-thermometer setup [77]. Fig. 4.1(b) shows the zero-field thermopower for all the doped films. The superconducting transition is clearly seen in the superconducting films. The normal state S (T>T_c) is negative in the underdoped region. It becomes positive in the overdoped region at low temperature (to be shown later). The magnitude of S in the underdoped region is large as expected for a system with smaller charge carrier density while it is much smaller in the overdoped region. Previous zero field thermopower measurements on NCCO crystals [78] are qualitatively similar to our data.

When a magnetic field of H=9 T is applied along the c-axis, the superconducting films are driven to the normal state for T<T_c. Fig. 4.1(a) shows the normal state thermopower of the x=0.16 film when the superconductivity is destroyed. The temperature dependence of the normal state Hall coefficient R_H at H=9 T of this film is also shown in the figure. A sign change from negative to positive for T<30 K is observed in both thermopower and R_H. The excellent agreement between the Hall effect and thermopower is not surprising since both thermopower and Hall coefficient are sensitive to the sign of charge carriers.

In Fig. 4.2, the normal state thermopower for all the doped films is presented.

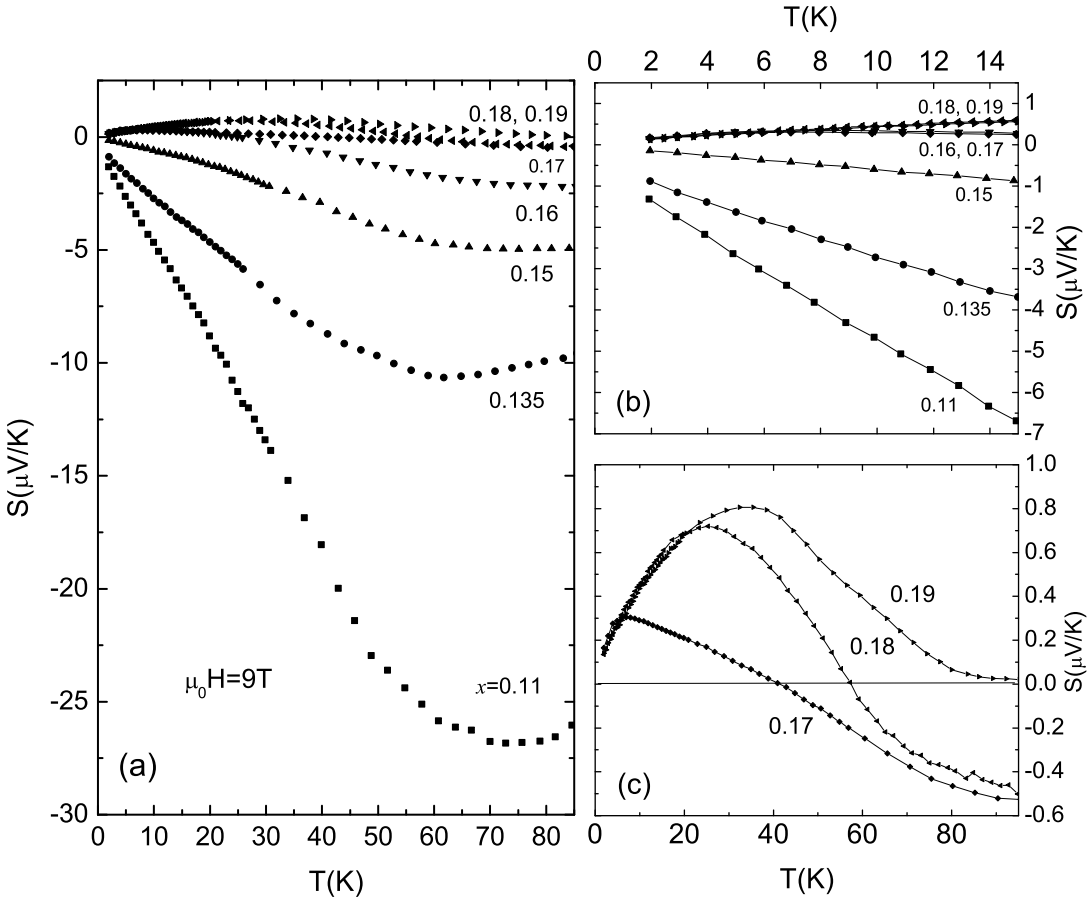

Figure 4.2: (a) The normal state thermopower S (μ_0H=9 T> $\mu_0 H_{c2}$) of all the doped films versus temperature. (b) shows the low temperature (T<15 K) data and (c) shows the low temperature thermopower of the overdoped films.

In the underdoped and optimally-doped films, the thermopower is large and negative. It decrease linearly with temperature, as seen from the low temperature (T<15 K) normal state thermopower shown in Fig. 4.2(b). In the overdoped films x=0.17 and 0.18, a sign change of thermopower for temperature below 45 K and 60 K is also observed. At low temperature, the normal state thermopower of the overdoped films increases towards a larger positive value as temperature decreases. It reaches a maximum value and then decreases towards zero as T→0. In the highly overdoped x=0.19 film, the thermopower is always positive, similar to the the Hall coefficient. From Fig. 4.2(b) and (c), we see that the low temperature thermopower in the overdoped films ($x \geq 0.16$) overlaps for T<10 K. The dramatic decrease of the low temperature thermopower from large negative for $x \leq 0.15$ to a doping independent positive value in the overdoped regime suggests a sudden Fermi surface rearrangement around the critical doping x=0.16, as suggested in the doping dependence of low temperature normal state Hall coefficient. In the next section, we will show a striking correlation between thermopower and Hall coefficient in PCCO.

4.3 Discussion

In the Boltzmann picture, thermopower and electrical conductivity are related through the expression in Eq. 2.53 [64]:

$$S = \frac{-\pi^2 k_B^2 T}{3e} \frac{\partial ln\sigma(\epsilon)}{\partial \epsilon}|_{\epsilon_F} \tag{4.1}$$

From Eq. 2.13, we know that the conductivity at the Fermi level is given by:

$$\sigma_{xx} = -e^2 \int \frac{d\vec{k}}{4\pi^3} v(\vec{k}) \tau(\epsilon) v(\vec{k}) \delta(\epsilon - \epsilon(\vec{k})) \tag{4.2}$$

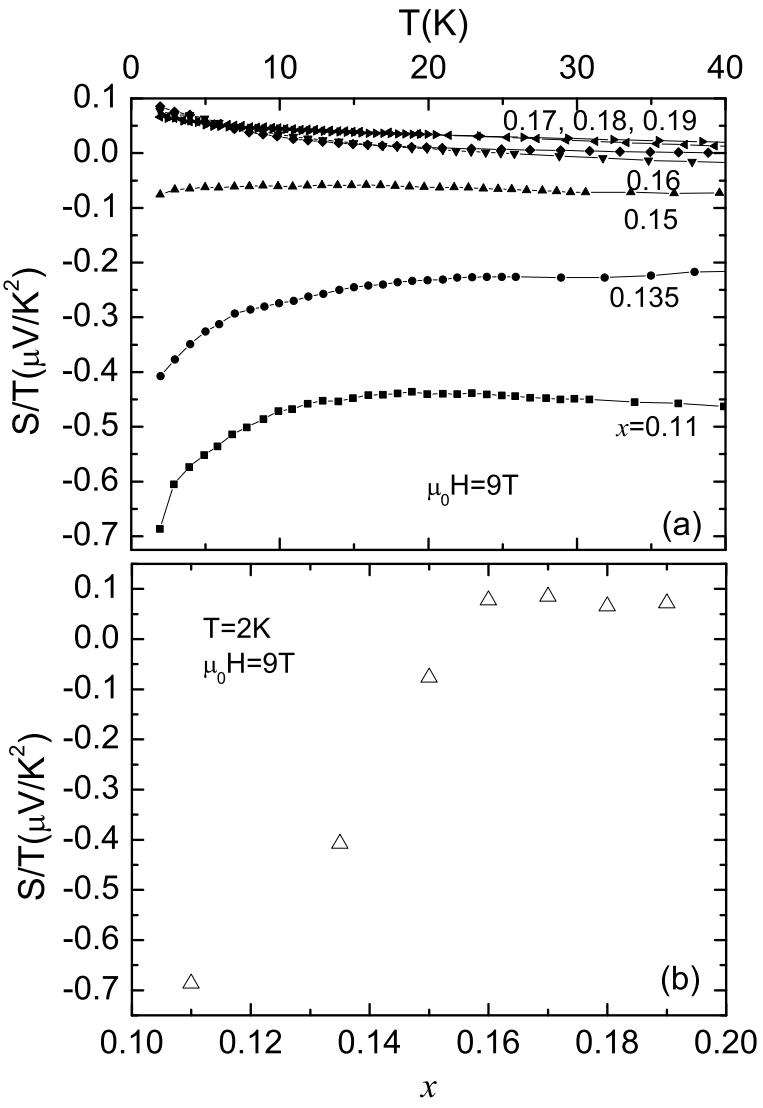

Figure 4.3: (a) S/T versus temperature (T<40 K and μ_0H=9 T) for all the films. (b) S/T(T=2 K and μ_0H=9 T) as a function of doping x.

Inserting Eq. 4.2 to 4.1 yields

$$S = -\frac{\pi^2 k_B^2 T}{3e}[(\frac{\partial ln\tau(\epsilon)}{\partial \epsilon})_{\epsilon_F} + \frac{\int d\vec{k}\delta(\epsilon_F - \epsilon(\vec{k}))m^{-1}(\vec{k})}{\int d\vec{k}\delta(\epsilon_F - \epsilon(\vec{k}))v^2(\vec{k})}] \tag{4.3}$$

where m^{-1} is the inverse of the effective mass tensor. In the case of a free electron gas, the second term of Eq. 4.3 is $\frac{3}{2\epsilon_F}$. The energy dependence of the scattering time can be expressed as:

$$\tau(\epsilon) = \tau_0 \epsilon^{\zeta} \tag{4.4}$$

which yields $(\frac{\partial ln\tau(\epsilon)}{\partial \epsilon})_{\epsilon_F} = \zeta/\epsilon_F$. This leads to a simple expression for the thermopower of a free electron gas:

$$S = \frac{-\pi^2 k_B^2 T}{3e\epsilon_F}(\frac{3}{2} + \zeta) \tag{4.5}$$

This indicates that the thermpower is expected to increase if the Fermi energy is lowered. The Fermi energy is related to the carrier density n and to the density of states, $N(\epsilon_F)$. For free electrons, $\epsilon_F = 3n/2N(\epsilon_F)$ and we then have

$$\begin{aligned} S/T &= \frac{-\pi^2 k_B^2}{3e}\frac{N(\epsilon_F)}{n}(1 + \frac{2\zeta}{3}) \\ &\simeq \frac{-\pi^2 k_B^2}{3e}\frac{N(\epsilon_F)}{n} \end{aligned} \tag{4.6}$$

Thus, if we neglect the small scattering term, then S/T is proportional to the ratio of $N(\epsilon_F)/n$. In real metals, from Eq. 4.3, the thermopower is proportional to $(\frac{\partial \ln \tau(\epsilon)}{\partial \epsilon})_{\epsilon=\epsilon_f}$. Therefore, the energy-dependence of the scattering time at the Fermi level also affects the thermopower. However, in the zero-temperature limit, it has been shown that this term also becomes proportional to $\frac{N(\epsilon_F)}{n}$ when impurity scattering dominates [79]. In electron-doped cuprates, there is strong evidence [49]

for impurity scattering at low temperatures. The residual resistivity is about 50 $\mu\Omega$-cm for an optimally-doped film, which is quite large compared to clean metals, and the temperature dependence of the resistivity becomes almost constant below 20 K. This is all suggestive of strong impurity scattering. The scattering most likely comes from Ce and oxygen disorder and one would expect a similar disorder at all dopings, although this is hidden by the anomalous (and unexplained) resistivity upturn for the lower dopings. Therefore, we expect that the thermopower being proportional to $N(\epsilon_F)/n$ will be a good approximation for our electron-doped PCCO films. This theory thus provides a solid theoretical basis for an experimental observation: in a wide variety of correlated metals, there is an experimental correlation between the magnitude of the thermopower and the electronic specific heat ($C_{el} \propto N(\epsilon_F)$) in the zero-temperature limit [80].

Now let us examine our thermopower data with this picture in mind. Fig. 4.3(a) presents S/T as a function of temperature below 40 K for all the doped films. As seen in the figure, there is a dramatic difference between the underdoped and the overdoped films. For underdoped, S/T displays a strong temperature dependence below 20 K, which is reminiscent of the low temperature upturn in resistivity and Hall effect [49, 56]. One possible explanation for this feature would be charge localization [81]. If all, or some of, the itinerant carriers localize at very low temperatures, then the decrease in conductivity is expected to be concomitant with an increase in the entropy per itinerant carrier (which is the quantity roughly measured by S/T). We find this to be qualitatively true as shown in Fig. 4.4, which displays S/T and conductivity for x=0.11 in a semilog plot. Below 10 K, both quantities are

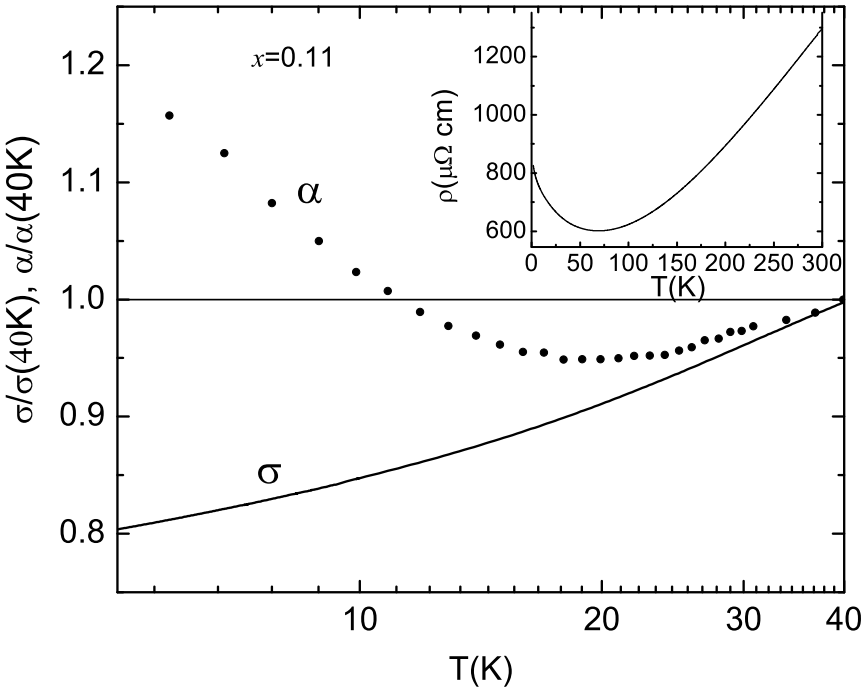

Figure 4.4: Normalized $\alpha = S/T$ and $\sigma(T)$ for x=0.11 versus temperature for T$\leq$40 K. Inset shows the temperature dependence of in plane resistivity $\rho(T)$ for the same film.

linear functions of logT. Note that for the resistivity, it has been shown [56] that the logarithmic divergence saturates below 1 K. Therefore, further thermopower measurements below 2 K would be very useful.

In contrast to the underdoped films, the temperature dependence of S/T in the overdoped region is weaker and there is clearly a finite S/T even at zero temperature. Taking the magnitude of S/T at 2 K as our reference, we can examine the doping dependence of the ratio $\frac{N(\epsilon_F)}{n}$ for itinerant carriers at this temperature. Fig. 4.3(b) presents the doping dependence of S/T at 2 K. A strong doping dependence for $x \leq 0.16$, a sharp kink around x=0.16 and a saturation in the overdoped region are visible. The dramatic change of S/T at low temperatures from the underdoped to overdoped regions is similar to the Hall effect [49] at 0.35 K, in which a sharp kink was observed around x=0.16 (Fig. 1.5). Both S/T and R_H change from negative in the underdoped region to a positive value above x=0.16.

The similarity of the doping dependence of S/T and R_H implies a common physical origin. To explore the relation between S/T and R_H, let us assume a simple free electron model, where thermopower displays a very simple correlation with the electronic specific heat,

$$C_{el} = \frac{\pi^2 k_B^2 T}{3} N(\epsilon_F) \tag{4.7}$$

Following the analysis of Ref. [80], a dimensionless quantity

$$q = \frac{S}{T} \frac{N_{Av} e}{\gamma} \tag{4.8}$$

can be defined (N_{Av} is Avogadro's number and $\gamma = C_{el}/T$), using Eqs.4.6, 4.7 and 4.8, one gets $q = N_{Av}/n$. For a simple metal, $R_H = V/ne$ (V is the total volume).

If we define

$$q' = R_H e/V_m \tag{4.9}$$

where V_m is unit cell volume, then q' is also equal to N_{Av}/n. By this simple argument, we can compare S and R_H directly. Because we do not have data for γ except at optimal doping, we assume that it does not change much with doping. With the γ value ($4mJ/K^2mole$) [82] for x=0.15 and S/T and R_H at 2 K, we can plot both q and q' together, as shown in Fig. 4.5. We find a remarkable similarity in the doping dependence of these two dimensionless quantities, both in trend and in magnitude. Note that no dramatic changes in either q or q' are observed near x=0.13, where it is claimed that AFM long range order vanishes [38] from recent inelastic neutron scattering measurements. We should mention that assuming a constant γ as a function of doping in our range of investigation (x=0.11 to 0.19) is, of course, subject to caution due to a lack of experimental data. However, it has been found [82] that the specific heat coefficient γ is the same for an as-grown crystal and a superconducting $Pr_{1.85}Ce_{0.15}CuO_4$ crystal. Neutron scattering studies have shown that an as-grown x=0.15 crystal is equivalent to an annealed $Pr_{1.88}Ce_{0.12}CuO_4$ crystal [83]. This strongly suggests that γ will not change much with Ce doping at least in the critical range around optimal doping. Therefore, no significant change in the doping dependence of q due to this correction is expected.

We believe that the saturation of S/T in the overdoped region is a result of the Fermi surface rearrangement due to the vanishing of antiferromagnetism above a critical doping. To our knowledge, there is no theoretical prediction for the doping

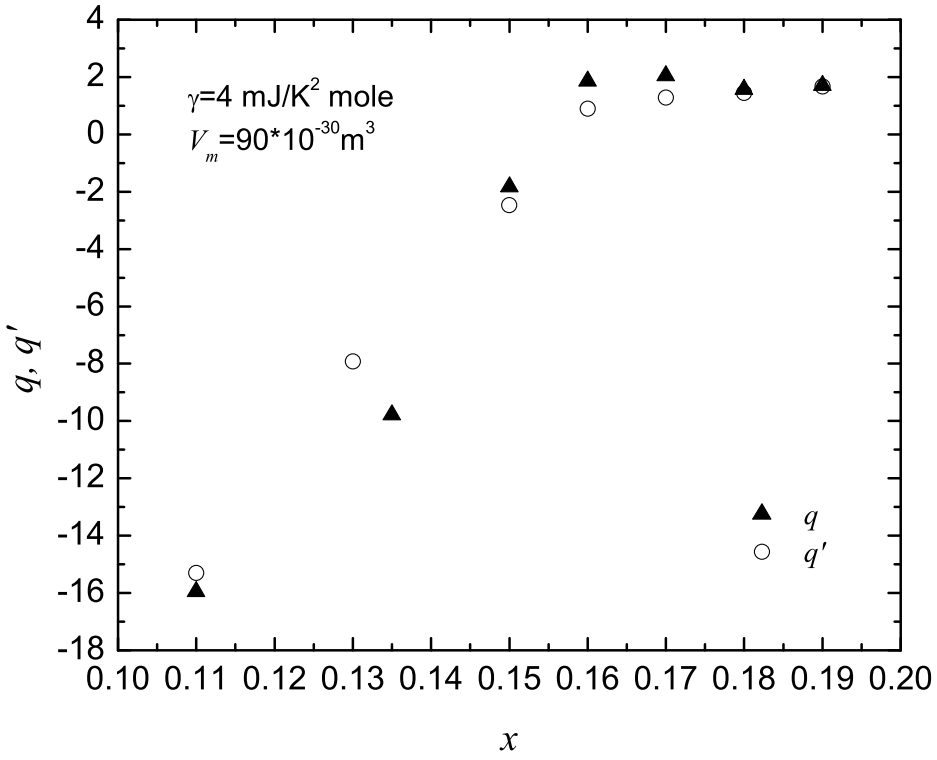

Figure 4.5: Doping dependence of q(2 K) and q'(2 K) of PCCO films (q and q' are defined by Eq. 4.8 and 4.9 in the text).

dependence of the thermopower in an antiferromagnetic quantum critical system. Although the temperature dependence of thermopower near zero temperature is given by Paul *et al.* [84] for such a system near critical doping, we are not yet able to access the very low temperature region (T<2 K) to test these predictions in PCCO. Nevertheless, an amazing agreement between thermopower and Hall effect measurements is shown in our simple free electron model. This model is certainly oversimplified since there is strong evidence for two types of carriers near optimal doping [46, 47, 48]. But, much of this transport data [46, 47, 48] implies that one type of carrier dominates at low temperature. Thus a simple model may be reasonable. However, to better understand this striking result a more detailed theoretical analysis will be needed.

Interestingly, the number q in overdoped PCCO is close to 1. It was shown that when q is close to unity, a Fermi liquid behavior is found in many strongly correlated materials [80]. This suggests that overdoped PCCO is more like a Fermi liquid metal than underdoped PCCO. When x is above the critical doping x=0.16, q and q' are close to $1/(1-x)$, which suggests that the hole-like Fermi surface is recovered in accordance with local density approximation band calculations and the Luttinger theorem.

In the underdoped region for $x \leq 0.15$, from Fig. 4.2(b), it appears that the thermopower decreases linearly with temperature and a finite value of thermopower exists at T=0. Therefore, the temperature dependence of thermopower S at low

temperature can be expressed as,

$$S = a + bT \tag{4.10}$$

where a and b are constants. This non-vanishing zero temperature thermopower is not expected from the Boltzmann expression (Eq. 4.1) and it is the reason for the low temperature divergence of S/T in the underdoped region. Recently, Yakovenko has developed a theory to explain this non-zero offset [85]. We outline this speculative idea in the following.

From Eq. 4.7. we have

$$c_{el} = C_{el}/n = \frac{\pi^2 k_B^2 T}{3} \frac{N(\epsilon_F)}{n} \sim \frac{k_B^2 T}{\epsilon_F} \tag{4.11}$$

and from Eq. 4.5, we have

$$S \sim \frac{c_{el}}{e} \sim \frac{k_B^2 T}{e\epsilon_F}. \tag{4.12}$$

By replacing $\epsilon_F = v_F P_F$, Eq. 4.8 can be written as

$$S \sim \frac{k_B^2 T}{e v_F p_F} \tag{4.13}$$

where v_F is the Fermi velocity and p_F is the Fermi momentum. Since the value of p_F is fixed by the number of carriers, it is roughly constant with temperature.

In the fermion condensate state [86], the Fermi velocity is not constant, but is proportional to temperature

$$v_F \sim \frac{T}{p_2 - p_1} \tag{4.14}$$

where $[p_1, p_2]$ is the region in the momentum space occupied by the fermion condensate. Substituting 4.10 to 4.9, we find

$$S \sim \frac{p_2 - p_1}{e p_F} \propto \quad constant(T) \tag{4.15}$$

Thus, for the fermion condensate the thermopower of 4.11 is temperature independent, unlike for the conventional Fermi liquid in Eq. 4.8. For a weakly developed fermion condensate, $eS \leq 1$, since generally $(p_2 - p_1) \leq p_F$.

In the electron-doped cuprate case as we observed, there is a finite T=0 intercept which is consistent with this theory. However, since we do not have the access to very low temperature (T <2 K), it is still not clear that the non-zero offset of thermopower is still there at zero temperature. Further ultra-low temperature normal state thermopower measurements in electron-doped cuprate are needed to confirm this. This could be very difficult to do since the thermopower signal will be extremely small.

4.4 Conclusion

In summary, we performed high resolution measurements to investigate the low temperature normal state thermopower of electron-doped cuprates $Pr_{2-x}Ce_xCuO_{4-\delta}$. We find a strong correlation between S/T and the Hall coefficient (R_H) at 2 K as a function of doping. Using a simple free electron model, which relates thermopower to the electronic specific heat, we conclude that our observations support the view that a quantum phase transition occurs near x=0.16 in the PCCO system.

Chapter 5

High-field Hall Effect and Magnetoresistance in $Pr_{2-x}Ce_xCuO_{4-\delta}$

5.1 Introduction

In chapter 1, we introduced that electron-doped cuprate superconductor behaves similarly in many ways as their hole-doped counterparts. Therefore, investigation of electron-doped cuprates should shed light on the mechanism of high-T_c superconductivity. On the other hand, electron-doped cuprates have exhibited many distinct properties, such as the competition between antiferromagnetism (AFM) and superconductivity and the existence of two electronic systems as revealed by ARPES experiments [50, 51, 53]. As shown in Fig. 1.6, a small electron-like Fermi surface (FS) pocket centers at $(\pi, 0)$ in the underdoped region with the simultaneous presence of both electron- and hole-like regions near optimal doping. This clarifies the long-standing puzzle that transport in these materials exhibits unambiguous n-type carrier behavior at low-doping and two-carrier transport near optimal doping [45, 46, 47, 48].

More recently, as discussed in chapter 4, a possible quantum phase transition is suggested by low temperature normal state transport experiments [49] in electron-doped $Pr_{2-x}Ce_xCuO_{4-\delta}$(PCCO). The sharp kink of the Hall coefficient at a critical doping x=0.16 is also observed in our thermopower measurements. The partial normal state gap observed in optical conductivity experiments [57] vanishes

above this critical doping. The critical doping exhibited in the transport properties is exactly same as the doping that the long range order AFM vanishes, as shown in early μSR measurements [35]. The extension of the AFM phase into the superconductivity dome is further supported by a later neutron scattering experiment [37], where the AFM phase is still robust in the field-driven normal state in a n-doped cuprate at optimal doping. The coincidence of the critical doping from transport and magnetic properties suggests that it is an antiferromagnetic to paramagnetic quantum critical point (QCP). However, as mentioned before, the exact location of the QCP is still under considerable debate. Motoyama *et al.* [38] claimed that the long range ordered AFM vanishes near the superconductivity dome boundary, x=0.13 and superconductivity does not coexist with AFM. Whether the QCP is inside the SC dome or not is important to clarify since the competition or coexistence of AFM and superconductivity may be essential for understanding the mechanism of superconductivity in cuprates.

Recently, a spin density wave (SDW) model was proposed to qualitatively explain the anomalous transport behavior in electron-doped cuprates [58, 59]. In this chapter, we review this model and present electrical transport experiments in PCCO in a high magnetic field. We show that our high-field result is also compatible with the SDW model. We performed Hall resistivity and ab-plane resistivity measurements on PCCO films from underdoped (x=0.11) to overdoped (x=0.19) for temperature down to T=1.5 K and magnetic field up to 58 T. We find that both the Hall resistivity and the magnetoresistance (MR) show a dramatic change near optimally-doped x=0.15. A surprising non-linear field dependence of Hall resistivity

for doping above the optimal doping is observed, while linearity of the Hall resistivity persists up to 58 T in the underdoped region. The field dependence of the MR changes from quadratic at low field to linear at high field in the overdoped region, as predicted by a recent theory on the magnetotransport near a metallic QCP [87]. Our results can be explained by the vanishing of the SDW gap at a critical doping and further suggest that the QPT occurs around optimal doping in the n-doped cuprates.

5.1.1 Spin density wave model

A spin-density wave (SDW) is a low-energy ordered state of solids that occurs primarily in low-dimensional materials that have high electronic density at the Fermi level. The transition to the SDW state is driven by the condensation energy, which is approximately $(N(E_F)\triangle_{SDW})$ where $\triangle_{SDW}$ is the magnitude of an energy gap opened by the transition at the Fermi surface. The SDW involves the development of a periodic modulation in the density of electronic spins with a characteristic spatial frequency Q that does not transform according to the lattice symmetry group. The periodicity Q is related to a nesting vector at certain high density of states regions of the Fermi surface (see a review of density waves in Ref. [88, 89]).

In the electron-doped cuprates, antiferromagnetism is found in the underdoped region. Muon spin rotation [35] and neutron scattering measurements [90] have shown the AFM is commensurate with the lattice in contrast to the hole-doped cuprates where incommensurate magnetism is found [91, 92]. The occurrence of the

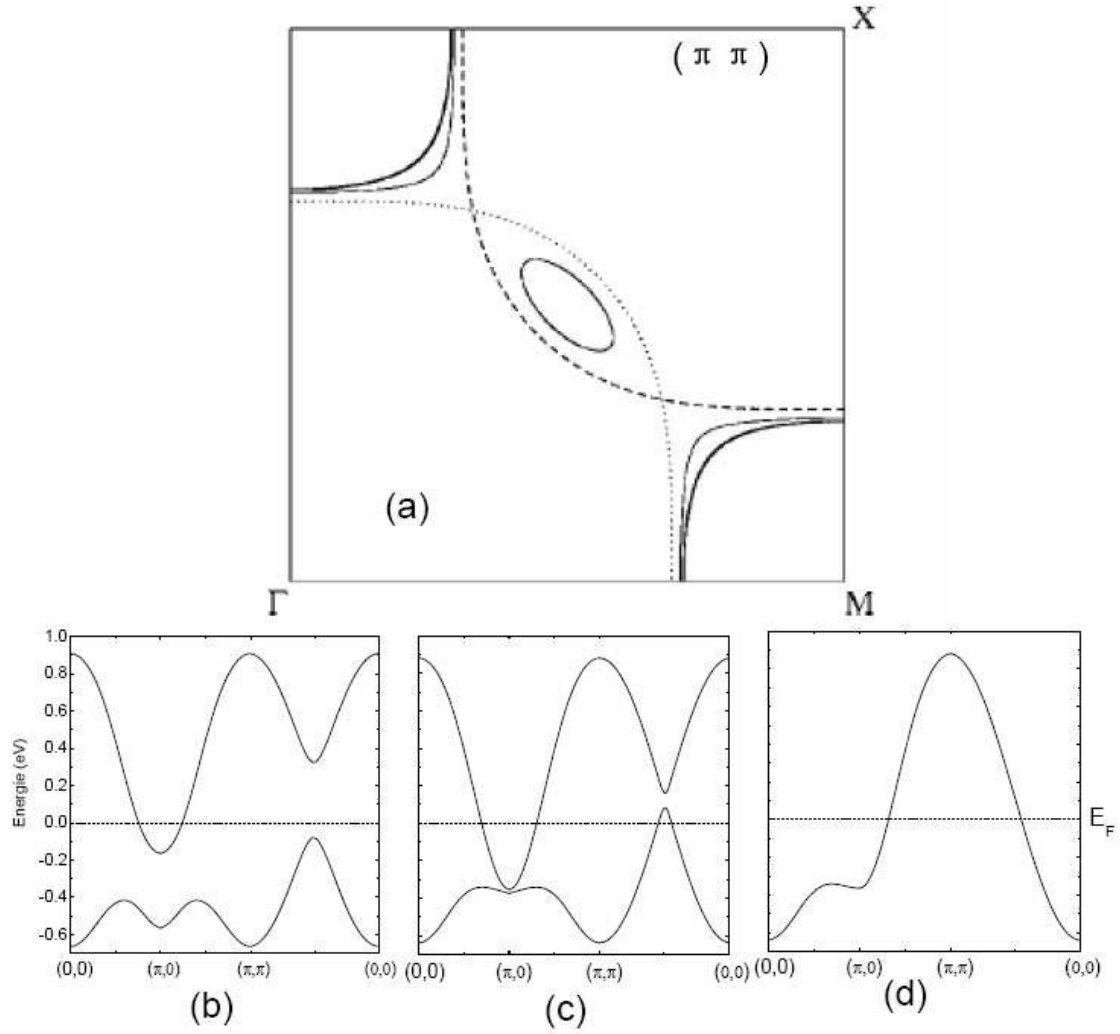

Figure 5.1: (a) Fermi surfaces calculated from Eq. 5.1 for x=0.15, band parameters t_1=0.38 eV, t_2=0.32t_1, t_3=0.5t_2 and backscattering (gap) values $\triangle$=0 (dashed line), $\triangle$=0.2 eV (light solid line), and $\triangle$=0.4 eV (heavy solid line). The dotted line is given by $\epsilon_{p+Q} = \mu(\triangle{=}0)$. (b)-(d), the corresponding dispersion curves for the different $\triangle$ values of 0.4 eV, 0.2 eV and 0 eV respectively.

SDW order with an energy gap would rearrange the Fermi surface and thus affect all the transport behavior. Lin and Millis [58] have proposed a 2D mean field SDW model to explain the low temperature Hall effect in electron-doped cuprates and also the optical properties [57, 59]. They consider electrons moving in a square lattice with dispersion

$$\epsilon_p = -2t_1(cosp_x + cosp_y) + 4t_2 cosp_x cosp_y - 2t_3(cos2p_x + cos2p_y). \tag{5.1}$$

$p_i(i = x, y)$ is the electron momentum component, $t_{1,2,3}$ are the 1st, 2nd and 3rd neighbor hopping band parameters , whose values are generally taken as t_1=0.38 eV, t_2=0.32t_1, and $t_3 = 0.5t_2$ [93].

When a commensurate SDW ordering occurs, the electrons are subject to a coherent backscattering of amplitude $\triangle_{SDW}$ and wave vector $\vec{Q} = (\pi, \pi)$ which doubles the unit cell, and the dispersion becomes

$$E_p^{\pm} = \frac{1}{2}[\epsilon_p + \epsilon_{p+Q} \pm \sqrt{(\epsilon_p - \epsilon_{p+Q})^2 + 4\triangle_{SDW}^2}]. \tag{5.2}$$

The Fermi surface shape depends on the gap amplitude. If $\triangle_{SDW} = 0$ then the Fermi surface consists of one large hole surface centered at (π, π) [dashed line in Fig. 5.1(a)]. The details of the Fermi surface reconstruction when $\triangle_{SDW} \neq 0$ depend on the band filling and the magnitude of $\triangle_{SDW}$. If the chemical potential μ is such that $\triangle_{SDW} < \triangle^*(\mu) = \epsilon_{(\pi/2,\pi/2)} - \mu = 4t_3 - \mu$ (μ=0.26 eV) then both bands cross the Fermi level and the Fermi surface involves two symmetry-inequivalent hole pockets centered at $(\pi/2, \pm\pi/2)$ and one electron pocket centered at $(0, \pi)$. One of the hole pockets and two portions of the electron pocket are shown as the light solid lines in Fig. 5.1(a). However, if $\triangle_{SDW} > \triangle^*(\mu)$, the lower band is completely filled

and only the electron pocket remains, as shown as the heavy solid line in the figure. The calculated corresponding dispersion plots for different $\triangle_{SDW}$ values are shown in Fig. 5.1(b)-(d), where one can clearly see the evolution of the band structure. This simple tight-binding model with the inclusion of a SDW gap appears plausible for interpreting the two-band like Hall effect and the normal state gap in optics [59]. In the next sections, we will find that our high field transport measurements are also consistent with this model.

5.2 Experiments and results

Six PCCO c-axis oriented films with various Ce concentrations (x=0.11 to 0.19) were fabricated by pulsed laser deposition on (100) oriented $SrTiO_3$ substrates (see chapters 3 and 4 and Ref. [69, 70]). Photolithography and ion mill techniques are used to pattern the films into a standard six-probe Hall bar. Resistivity and Hall effect measurements were carried out in a 60 T pulsed magnetic field at the NHMFL. The magnetic field is aligned perpendicular to the ab-plane of the films. Possible eddy current heating was carefully considered and reduced (see chapter 3 for details).

In the low field Hall effect experiments, the normal state Hall resistivity $\rho_{xy}(H)$ is linear up to a 14 T field at all doping and temperatures. R_H is determined from the slope of $\rho_{xy}(H)$. The temperature dependence of R_H was shown in Fig. 1.5. In a high magnetic field, a non-linear $\rho_{xy}(H)$ is observed at certain dopings and temperatures. This is in striking contrast to the linear $\rho_{xy}(H)$ found up to 60 T in

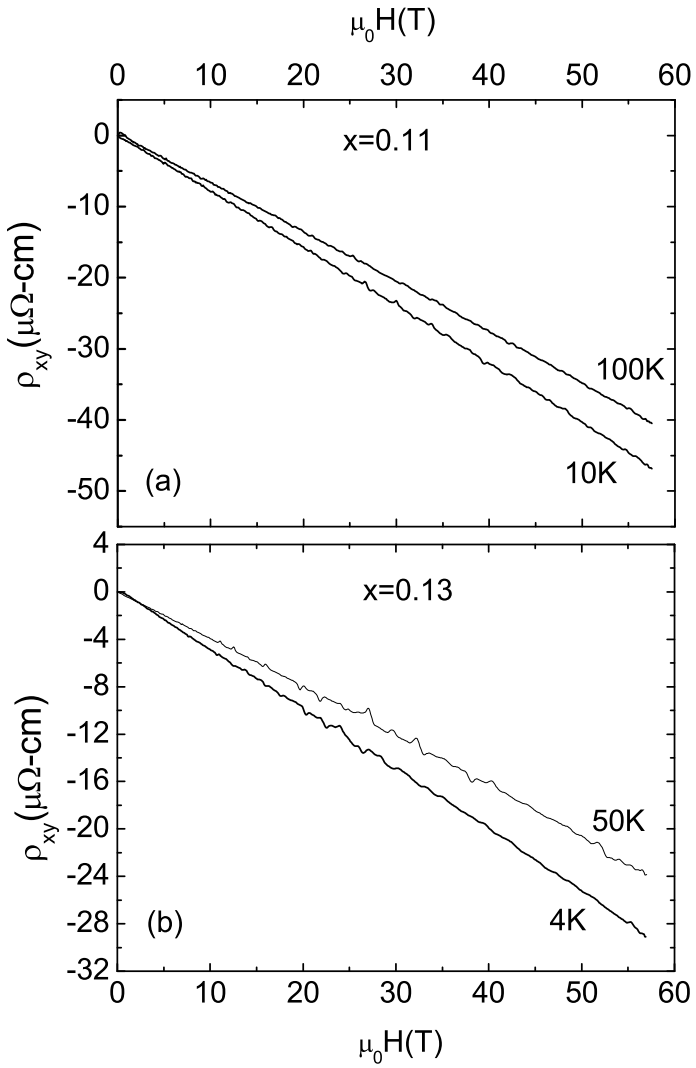

Figure 5.2: Hall resistivity ρ_{xy} versus magnetic field H for the underdoped PCCO films (a) x=0.11 and (b) x=0.13.

p-doped $Bi_2Sr_{2-x}La_xO_{6+\delta}$ at all dopings and temperatures [94].

For the underdoped PCCO films, the linear $\rho_{xy}(H)$ as seen in low field persists up to 58 T at temperatures below 100 K (the limit of our present data). Fig. 5.2(b) shows the $\rho_{xy}(H)$ data for an underdoped x=0.13 film(T_c=11 K). For the non-superconducting x=0.11, a similar behavior is observed [Fig. 5.2(a)]. The negative slope of $\rho_{xy}(H)$ indicates an electron-like behavior in the underdoped region at all fields. In contrast, as x approaches the optimal doping (x=0.15), the field dependence of $\rho_{xy}(H)$ behaves differently. As shown in Fig. 5.3(a), at low temperature (T<50 K) $\rho_{xy}(H)$ is negative and linear up to about 30 T but then starts curving towards positive slopes. This nonlinearity begins at higher fields as the temperature is increased and it appears that $\rho_{xy}(H)$ will become linear above 50 K, but we were not able to obtain data above 50 K on this sample. For the overdoped film x=0.16, the low temperature $\rho_{xy}(H)$ is positive and slightly non-linear at high field. The nonlinearity becomes more prominent near the temperature where R_H changes sign (about 25 K), but then a negative linearity of $\rho_{xy}(H)$ is found at higher temperatures. The positive slope of $\rho_{xy}(H)$ at high field for T$\leq$75 K indicates a hole-like contribution. A similar behavior was observed for the x=0.17 film as shown in Fig. 5.3(c). For a highly overdoped film, x=0.19, in which R_H is always positive but with a minimum around 120 K [Fig. 1.5(a)], a strong field dependence of $\rho_{xy}(H)$ is observed above 30 K, while $\rho_{xy}(H)$ is linear at low temperatures.

In high fields, the behavior of magnetoresistance (MR) in PCCO is different with doping x. As found previously [55], a large negative MR (nMR) is observed in the underdoped films at low temperatures. For x=0.11 below 100 K, this nMR

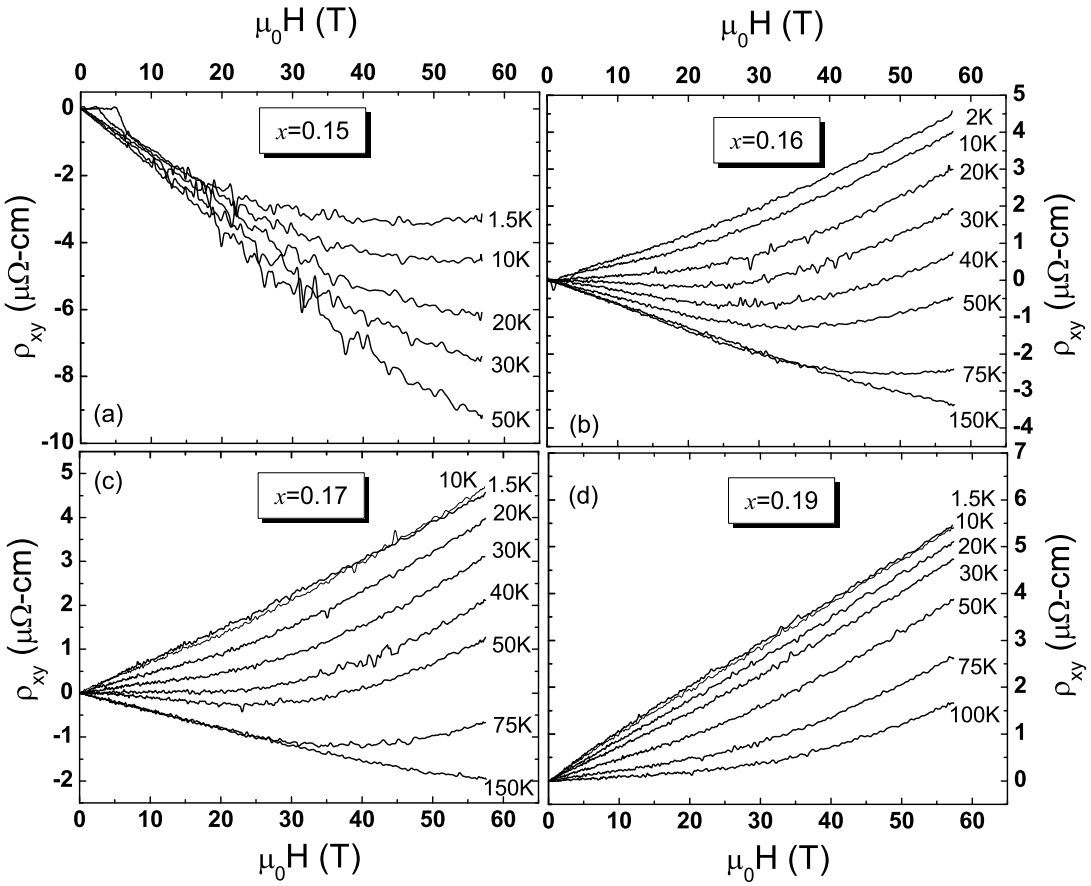

Figure 5.3: Hall resistivity ρ_{xy} versus magnetic field H for the optimally-doped and overdoped PCCO films (a) x=0.15, (b) x=0.16, (c) x=0.17, (d) x=0.19.

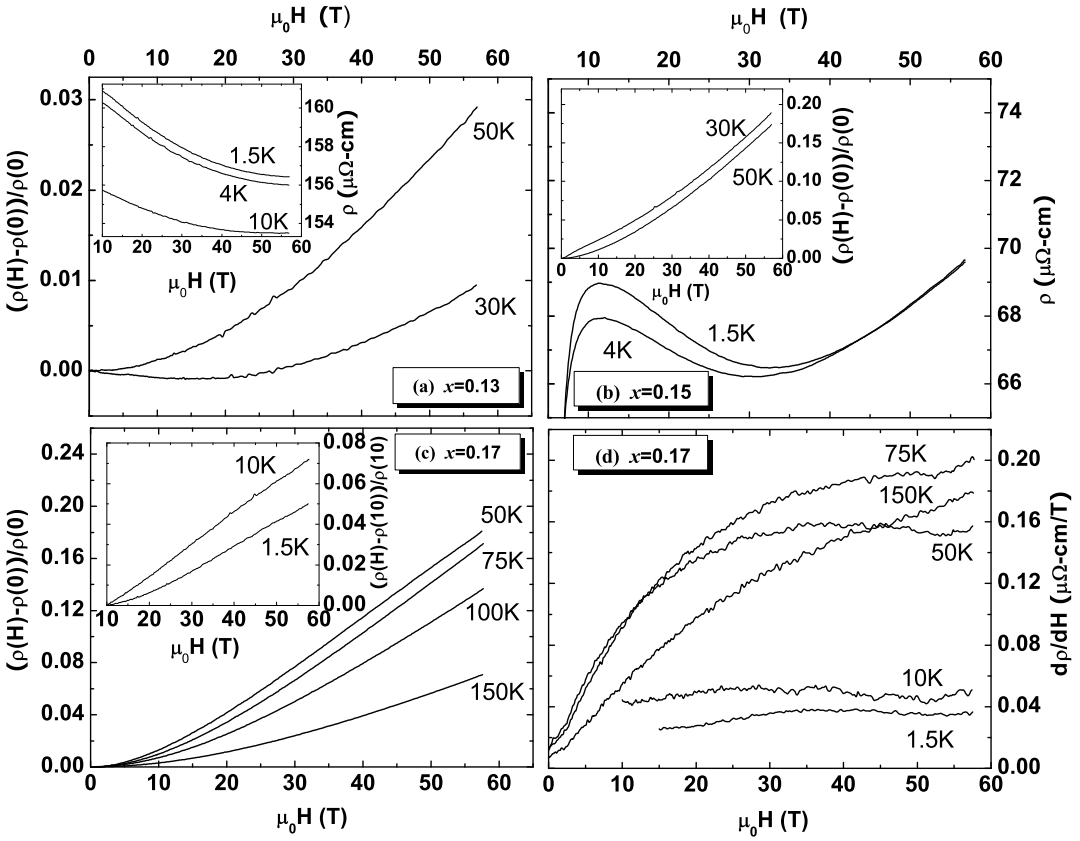

Figure 5.4: In-plane resistivity versus H (H$\perp$ *ab*) for the PCCO films. (a) x=0.13, (b) 0.15, (c) 0.17, and (d) first derivative plots of MR for x=0.17. Insets show the MR in a different temperature range from the main panels.

persists up to 58 T, while for x=0.13 for T<30 K, the nMR tends to saturate at high field, as shown in the inset of Fig. 5.4(a). A positive MR is recovered at higher T above 50 K, and it follows a quadratic field (H^2) dependence. For the optimally-doped x=0.15, the low temperature nMR reverses to a positive MR at about 30 T [1.5 K and 4 K data in Fig. 5.4(b)]. For T>20 K, the positive MR also obeys H^2. In the overdoped films, a positive MR is found in the normal state, but the field dependence of the MR is surprisingly different as the temperature is increased. Fig. 5.4(c) and (d) show the MR along with the the first field derivative of MR ($d\rho_{xx}(H)/dH$) for the x=0.17. At low temperatures (T<20 K), a nearly linear MR for H>H_{c2} is found, as seen from the roughly constant behavior of $d\rho_{xx}(H)/dH$. However, in the intermediate temperature range where the non-linear $\rho_{xy}(H)$ is prominent, we find that $d\rho_{xx}(H)/dH$ increases monotonically at lower field and then saturates to a nearly constant value at higher field. The low field linear increase of $d\rho_{xx}(H)/dH$ indicates a quadratic MR and the high field saturation indicates a linear MR. A similar linear MR is also observed in the x=0.16 and 0.19 films at low temperatures where the linear $\rho_{xy}(H)$ is in present. At higher temperatures, MR changes from quadratic at low field to linear at high field.

5.3 Discussion

5.3.1 Two-band model

The non-linear behavior of $\rho_{xy}(H)$ displayed on Fig. 5.3 can be simulated within the framework of a conventional two-band Drude model. The Drude model

assumes field-independent carrier density and relaxation time, in which case $\rho(H)$ can be written as [62] (see also chapter 2):

$$\rho_{xy}(H) = \frac{\sigma_h^2 R_h - \sigma_e^2 R_e - \sigma_h^2 \sigma_e^2 R_h R_e (R_h - R_e) H^2}{(\sigma_e + \sigma_h)^2 + \sigma_e^2 \sigma_h^2 (R_h - R_e)^2 H^2} H \tag{5.3}$$

and

$$\rho_{xx}(H) = \frac{(\sigma_h + \sigma_e) + \sigma_h \sigma_e (\sigma_h R_h^2 + \sigma_e R_e^2) H^2}{(\sigma_h + \sigma_e)^2 + \sigma_h^2 \sigma_e^2 (R_h - R_e)^2 H^2} \tag{5.4}$$

where $\sigma_{e(h)}$ and $R_{e(h)}$ are electrical conductivity and Hall coefficient of the electron (hole) band. Using the relation of $\sigma_0 = \sigma_h + \sigma_e$ (σ_0 is the zero field normal state conductivity), one parameter is eliminated. We attempted to fit the $\rho_{xy}(H)$ and $\rho_{xx}(H)$ data, but we could not fit both of them with the same fitting parameters for any of the films. As seen in Fig. 5.5, the parameters R_h and R_e that are obtained from the best fits of $\rho_{xy}(H)$ and $\rho_{xx}(H)$ to Eqs. 5.3 and 5.4 at T=30 K are quite different.

We also find that the parameters found by fitting $\rho_{xy}(H)$ alone are in conflict with the ARPES results. From a fit of the $\rho_{xy}(H)$ data of the x=0.15 film at T=10 K, as seen in Fig. 5.6, we get the hole and electron densities $n_h = \frac{1}{R_h|e|} = 6.0 \times 10^{20}/cm^3$ and $n_e = 3.5 \times 10^{20}/cm^3$. These numbers disagree with $n_h = 3.6 \times 10^{20}/cm^3$ and $n_e = 1.8 \times 10^{21}/cm^3$, the estimate from the areas of the hole and electron pockets in ARPES [i.e., $n = A/2\pi^2$, A is the the area of the electron (hole) pocket] [50]. The departure of our fits from the experimental data is most likely due to the simple assumption of a field-independent charge density and scattering in the Drude model. This is unlikely to be valid for the n-doped cuprates with their complex FS. It is likely that there is a strong anisotropic scattering, as found in p-doped cuprates [95].

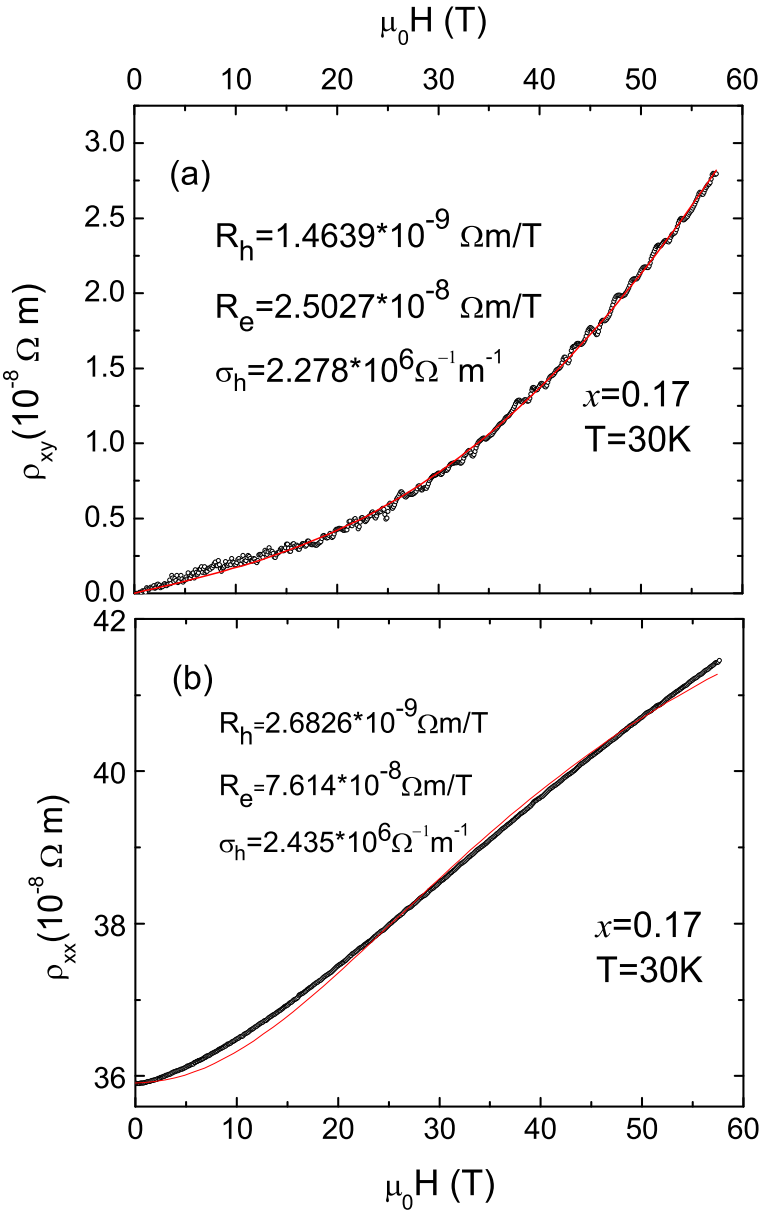

Figure 5.5: A two-band fitting to the Hall resistivity $\rho_{xy}(H)$ and magnetoresistance $\rho_{xx}(H)$ in an overdoped x=0.17 PCCO film at T=30 K. Red lines are fits to Eq. 5.3 and 5.4. The fitting parameters R_h, R_e and σ_h are shown in the figures [$\sigma_0 = 2.784 * 10^6/(\Omega m)$].

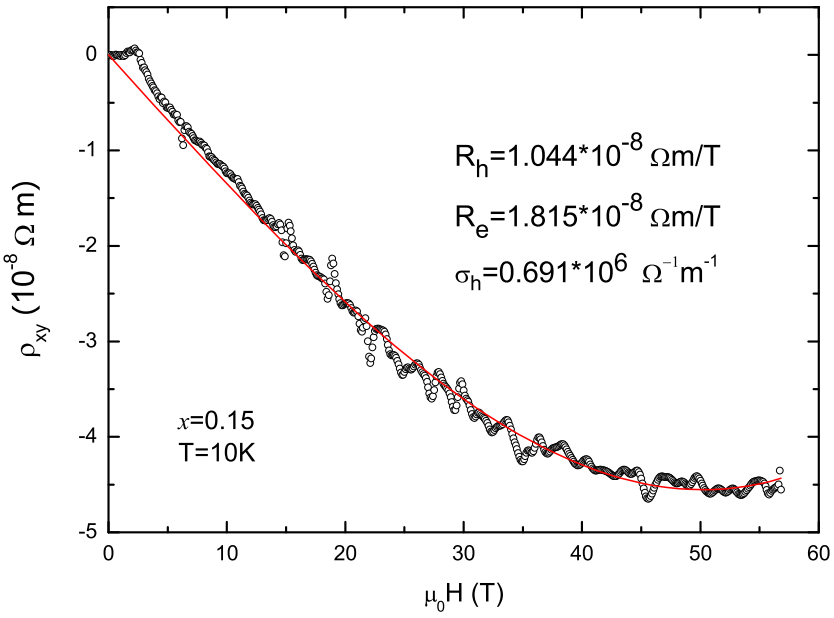

Figure 5.6: A two-band fitting to the Hall resistivity $\rho_{xy}(H)$ in an optimally-doped x=0.15 PCCO film at T=10 K. Red line is the fitting to Eq. 5.4.

Therefore, the simple two-band Drude model is not sufficient to explain the high-field magnetotransport in PCCO. A modified model with consideration of field dependent charge density or scattering might explain our data, however, this is beyond our present knowledge and the scope of this thesis.

5.3.2 A spin-density wave explanation

We now discuss a qualitative explanation for our data based on the SDW model discussed before. As seen from the phase diagram of n-doped cuprates (see Fig. 5.7), the long range ordered AFM phase persists up to a critical doping of

x_c (exact location is under debate). In the underdoped region, a large SDW gap ($\triangle_{SDW}$ of order of 100 T) opens at certain temperatures [57]. In a magnetic field comparable to the gap (i.e. $\mu_B B \sim \triangle_{SDW}$), one expects a suppression of $\triangle_{SDW}$ by the field and a consequent change of the FS. Since $\rho_{xy}(H)$ is sensitive to the shape of the FS, a non-linear ρ_{xy} in high field might emerge. Applying this picture to our data, let us start from the lowest temperature (1.5 K). In the underdoped x=0.11 and 0.13, we find that the linear $\rho_{xy}(H)$ persists up to 58 T [Fig. 5.2], suggesting that the field is not sufficient to destroy the large SDW gap. Therefore, the electron-like pocket still survives to high field for all the temperatures measured (up to 100 K). As the doping approaches the critical doping, $\triangle_{SDW}$ decreases rapidly. When the magnetic field is strong enough to suppress the smaller gap, the hole-like pocket emerges and will contribute to $\rho_{xy}(H)$. The positive slope of $\rho_{xy}(H)$ at high field in the optimally-doped film x=0.15 suggests the suppression of the SDW gap and a contribution from the hole band.

In the overdoped region for $x \geq 0.16$, the linear positive $\rho_{xy}(H)$ at the lowest temperature strongly suggests the absence of the SDW gap and a hole-like behavior. The nonlinearity of $\rho_{xy}(H)$ appears at higher temperatures for larger x, as seen in Fig. 5.3. Notice that a slightly non-linear ρ_{xy}(H) is found for x=0.16 even at the lowest temperature 2 K, while in x=0.17 and 0.19, this nonlinearity starts to appear at temperatures above 10 K and 30 K, respectively, as indicated with triangles in Fig. 5.7.

The observed nonlinearity in $\rho_{xy}(H)$ in the overdoped region in the intermediate temperature range suggests a competition between electron and hole bands.

This unusual nonlinearity of $\rho_{xy}(H)$ might arise from spin fluctuations of SDW order in a quantum critical region associated with the QCP at x_c. As shown in Fig. 5.7, thermally activated spin fluctuations (gap-like) in the overdoped region at finite temperature could result in a mix of electron and hole contributions to $\rho_{xy}(H)$. This could be responsible for the sign change of the $R_H(T)$ [Fig. 5.2(a)] and the positive upturn of the $\rho_{xy}(H)$ at high fields. In the critical region, an external perturbation, such as temperature or magnetic field, could change the relative impact of the two bands. The onset temperature of the high field non-linear $\rho_{xy}(H)$ shifts towards a higher temperature as x increases, which strongly suggests the system is further away from the critical region at higher doping.

Interestingly, we notice that our MR is also qualitatively consistent with the SDW model. In the underdoped region, the low temperature nMR persists and saturates in high field [Fig. 5.4(a)], suggesting that the nMR is related to spin scattering [55]. At optimal doping, a positive MR is recovered at a field where $\rho_{xy}(H)$ changes slope. The complete suppression of the nMR suggests the reduction of the spin contribution. For the overdoped films ($x \geq 0.16$), we find that the crossover in the field dependence of the MR is consistent with a recent theory by Fenton and Schofield [87]. They have shown that near a metallic QCP, a quadratic MR ($\frac{\triangle\rho}{\rho} \sim H^2$) is expected for a system with a SDW gap and a linear MR without a gap. As shown in Fig 5.4(c) and (d), in the intermediate temperature range, the MR changes from quadratic to linear as the field increases while it is always linear at low temperature. This suggests the absence of the SDW gap at low temperature. In the spin fluctuation region, the field suppressed spin contribution could be responsible

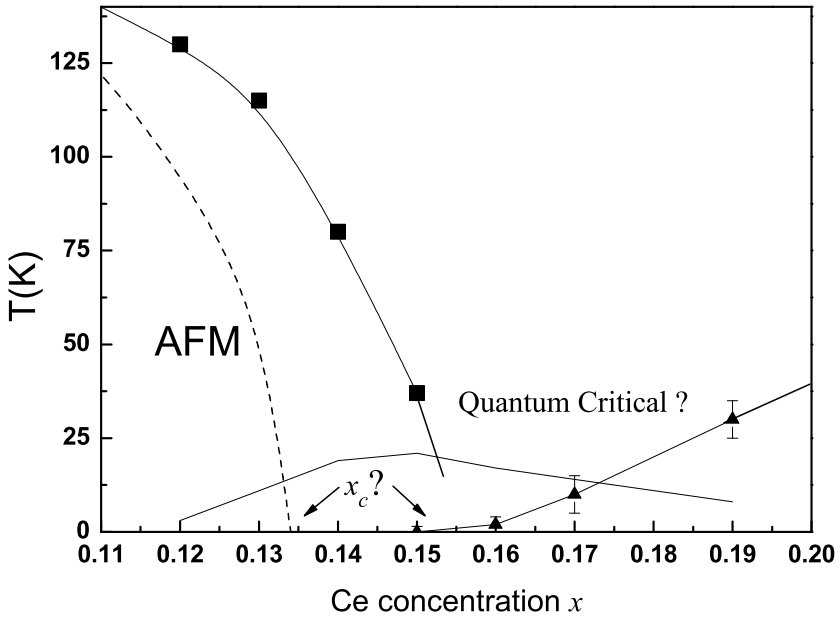

Figure 5.7: A phase diagram for n-doped cuprates. Black squares and dotted line are the controversial AFM transition temperature from Ref. [35, 37] and Ref. [38] respectively. The solid line is T_c. The triangles mark the temperature above which the non-linear ρ_{xy} appears for each doping.

for the recovery of the linear MR at high field. At much higher temperatures (above 150 K), the quadratic MR is restored.

We have shown that our $\rho_{xy}(H)$ and $\rho_{xx}(H)$ are qualitatively consistent with the SDW model, suggesting that the QPT occurs near or just above the optimal doping. However, the SDW gap closing field (about 30-40 T for x=0.15) obtained from the nonlinear $\rho_{xy}(H)$ is much smaller than the value of 100 T [k_BT(=70 K)/μ_B] from the optics measurements [57]. Further quantitative theoretical work is needed to resolve this issue and to explain in detail the $\rho_{xy}(T,H)$ and $\rho_{xx}(T,H)$ results that we report here.

5.4 Conclusion

In summary, we performed high-field resistivity and Hall effect measurements in the n-doped cuprate $Pr_{2-x}Ce_xCuO_{4-\delta}$. We find an anomalous non-linear Hall resistivity at high field above optimal doping at certain temperatures. We also observed a crossover of the field dependence of magnetoresistance at high field in the overdoped region. Our results are qualitatively consistent with the spin density wave gap induced Fermi surface rearrangement model [58], and also support the view that a quantum phase transition occurs under the superconducting dome in electron-doped cuprate superconductors.

Chapter 6

Upper Critical Field of $Pr_{2-x}Ce_xCuO_{4-\delta}$ in Parallel Magnetic Fields

6.1 Introduction

The upper critical field H_{c2} is a crucial parameter for high-T_c superconductors. It provides important information about the superconducting parameters, such as coherence length, and superconducting gap [4]. In past years, numerous transport experiments[96, 97] on high-T_c cuprates in the H$\perp$ *ab* configuration have been reported and the H_{c2}-T diagrams have been established. A positive curvature in both cases was observed from the resistivity measurements, which is in contradiction to the expected low temperature saturation in the Werthamer-Helfand-Hohenberg (WHH) theory [98]. The most likely reason for this is that the complicated H-T phase diagram of high-T_c superconductors includes a broad region of a vortex liquid state and strong superconducting fluctuations [65, 99]. These properties are detrimental to the determination of H_{c2} from resistivity measurements. Recent high-field Nernst effect measurements [99] in hole-doped cuprates revealed a different H-T diagram when H_{c2} is determined by a loss of vorticity. A significant increase of H_{c2} and an extrapolation of H_{c2}(T) to well above T_c were found. This observation was explained by the existence of a non-vanishing pairing amplitude well above T_c, while long range phase coherence emerges only at T_c. H_{c2} could then be a measure of the onset of pairing amplitude.

Most of the H_{c2} results obtained so far on the cuprate superconductors are in the H⊥ab configuration. The strong anisotropy, which would result in a much higher H_{c2} for magnetic field parallel to the conducting plane (ab-plane), and the limitation of laboratory accessible magnetic fields makes the $H_{c2\|ab}$ determination impossible for most of the cuprates. Nevertheless, a few $H_{c2\|ab}$ data have been reported [100, 101, 102, 103]. An early work [104] that predicted $H_{c2\|ab}(T = 0)$ for $YBa_2Cu_3O_{7-\delta}$ based the initial slope, $-dH_{c2}/dT$ near T_c, was shown to be an overestimation by recent measurements [100, 101]. The reason for this is that WHH theory only accounts for the orbital pair breaking, but in the H‖ab orientation, the Pauli spin pair breaking effect could also be important. In fact, a recent measurement [105] on an underdoped $Bi_2Sr_2CuO_{6+\delta}$ in a pulsed magnetic field up to 52 T found that the Pauli paramagnetic limit could explain the H_{c2} for field parallel to the conducting layers.

Compared to the hole-doped cuprates, the electron-doped are distinctive for having a much lower $H_{c2\perp ab}$ [97]. This implies a larger in-plane coherence length, and thus a smaller orbital critical field for H parallel to CuO_2 planes is expected. In addition, Nernst effect measurements have shown that electron-doped cuprates have much weaker superconducting fluctuations [106] compared to the hole-doped. In this chapter, we present systematic parallel critical field measurements in the electron-doped $Pr_{2-x}Ce_xCuO_{4-\delta}$ (PCCO) for doping (x) throughout the SC region and establish the $H_{c2\|ab}$-T phase diagram. We find that the low temperature parallel critical field is large (above 58 T at 4 K) for the underdoped and optimally doped films, while it is below 58 T for the overdoped films. We also find that the Zeeman

splitting energy $\mu_B H_{c2\|ab}$ approaches the SC gap. Therefore, we conclude that the paramagnetic limit is the cause of the suppression of superconductivity in the H$\|$ab configuration.

6.2 Experiments and results

Five PCCO films with different doping(x=0.13, 0.15, 0.16, 0.17, 0.19) with thickness about 2500 Å, were fabricated by pulsed laser deposition on $SrTiO_3$ substrates. Details of film growth and characterization can be found in chapter 3 and 4 [70, 69]. Photolithography and ion-mill techniques were used to pattern the films into a standard six-probe Hall bar. The size of our films after patterning is 2×3 mm^2. Parallel field resistivity measurements were carried out using a 60 T pulsed magnetic field at the National High Magnetic Field Laboratory (NHMFL) in Los Alamos. The duration of magnetic field pulse is 100 ms. Resistivity data traces were recorded on a computer using a high-resolution low-noise synchronous lock-in technique developed at NHMFL. The films were carefully aligned to ensure a parallel field (within $\pm 1^0$ with respect to the ab-plane) and we found no signs of eddy current heating in the data (see chapter 3 for details).

Fig. 7.4 shows the in-plane resistivity (ρ_{ab}) versus temperature in zero field and in 58 T for H$\|$ab for all the films. The zero field transition temperatures are 10.8 K, 21.3 K, 16.9 K, 14 K, and 10.4 K for x=0.13, 0.15, 0.16, 0.17 and 0.19 respectively. In the H$\perp$ab field orientation, a field of order H$\leq$10 T is enough to suppress the superconductivity, similar to previously work [97]. However, when the

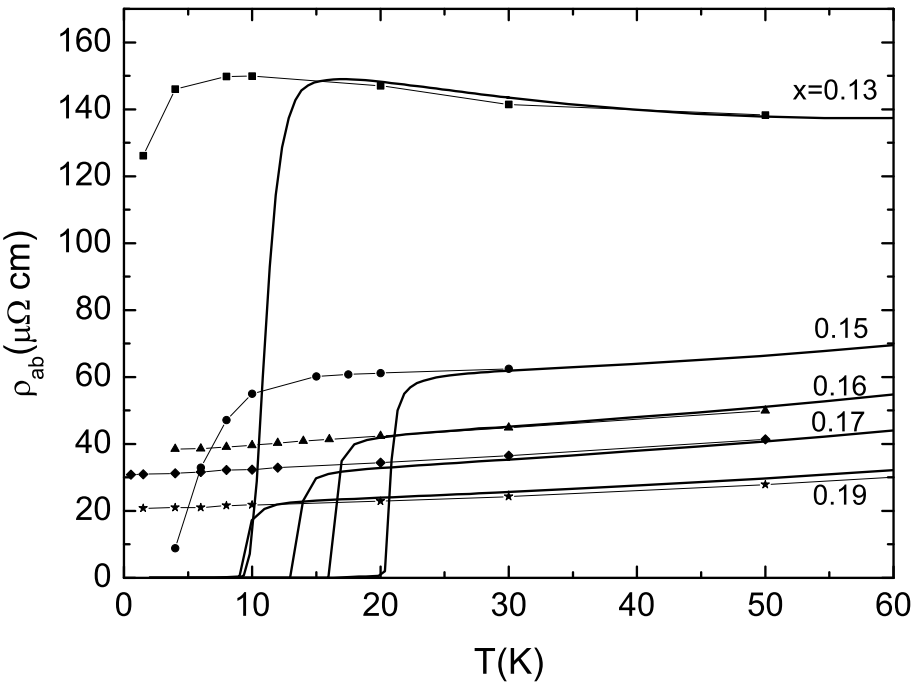

Figure 6.1: In-plane resistivity versus temperature in zero field (solid lines) and 58 T for H‖ab (filled symbols) configuration for all the films (x=0.13, 0.15, 0.16, 0.17 and 0.19).

field is aligned in the ab-plane, the superconductivity is not completely destroyed in the underdoped x=0.13 and optimally doped x=0.15 films even at 58 T, as seen in Fig. 7.4. In Fig. 7.10 we show ρ_{ab}(H) for H parallel to the ab-plane for the films x=0.15 and 0.16. Apparently, the normal state can not be completely recovered in the optimally doped x=0.15 for T$\leq$10 K. However, for the overdoped film $x \geq$0.16, 58 T is sufficient to destroy the superconductivity even at the lowest temperature (1.5 K) measured. Compared to the H$\perp$ab geometry [97], a broader transition in $\rho_{ab}(H)$ is observed for the parallel field orientation. A similar behavior was found for the other dopings (not shown).

From the $\rho_{ab}(H)$ traces in Fig. 7.10, we can determine the resistive parallel critical field. However, the choice of a criterion remains arbitrary, mainly because of the curvature of the high-field flux-flow resistivity typical of all high-T_c superconductors. Following the schemes in prior work [96, 97], we can determine the characteristic fields corresponding approximately to the onset of flux flow (H_{onset}) and a higher field corresponding to the complete recovery of the normal state (H_{100}). In Fig. 6.3(a), we show H_{onset} and H_{100} as a function of the reduced temperature (T/T_c) for x=0.16. The larger uncertainty of H_{100} is marked with larger error bars. In this figure, we also show the extracted value (H_{ext}) at the extrapolation point of the flux-flow region and the normal state asymptote. We find that H_{ext} lies between H_{onset} and H_{100} and it is close to the field value determined from 90% of the normal state resistivity. We note that the H_{ext} criterion has been regularly used as representing an acceptable determination of H_{c2} and we will adopt H_{ext} values as our estimate of $H_{c2\|ab}$.

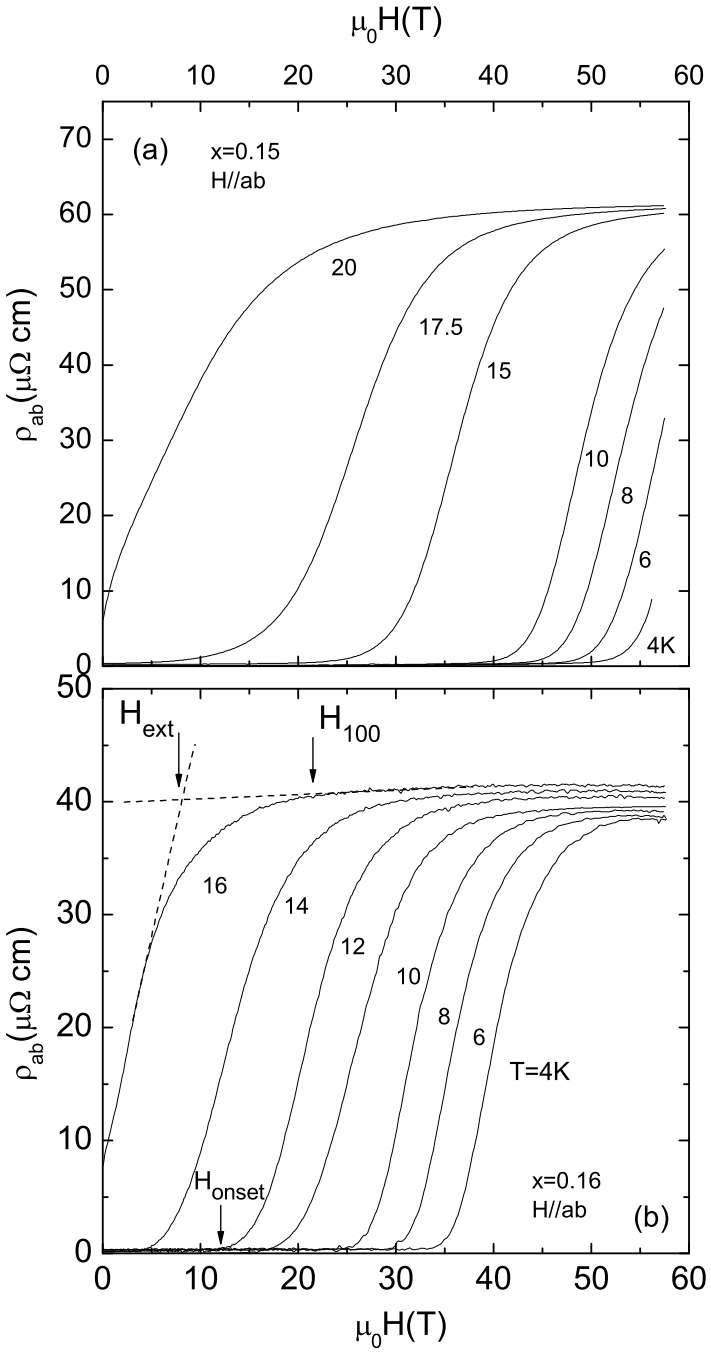

Figure 6.2: In plane resistivity ρ_{ab} versus magnetic field for H||ab-plane for (a) x=0.15 (T_c=21.3 K from resistivity) and (b) x=0.16 (T_c=16.9 K).

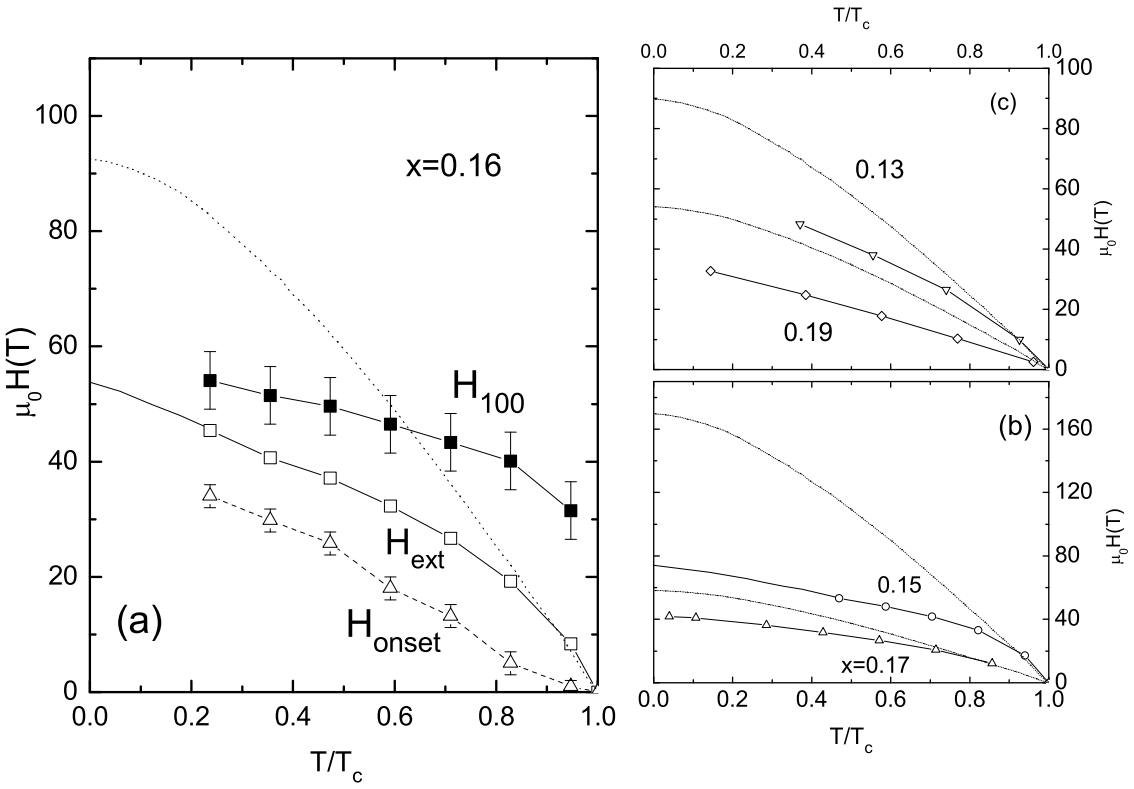

Figure 6.3: (a) Resistive characteristic fields H_{onset}, H_{ext} and H_{100} for H‖ab deduced from different criterion as a function of reduced temperature T/T_c for x=0.16, (b) H_{ext} (open symbols) and H_{100} (filled symbols) versus T/T_c for x=0.15 and 0.17. (c) shows the data for x=0.13 and 0.19. Dotted lines are fits to the WHH theory [98]. Solid lines are extrapolation based on a smooth H(T) behavior.

In Fig. 6.3(b), we plot the characteristic field H_{ext} as a function of T/T_c for the other films(we note that T_c is taken from resistivity in a procedure similar to H_{ext}). In contrast to $H_{c2\perp ab}(T)$ [47], no low temperature divergence or positive curvature is observed in the H||ab configuration for most of the films. Although the low temperature $H_{c2\|ab}(T)$ behavior is unknown for x=0.13 and 0.15 due to the limit of our field, from the overdoped films data a saturation seems to emerge at low temperature, which is similar to hole-doped cuprates [101, 105]. From the H-T plots in Fig. 6.3, we can roughly extrapolate the curves to get $H_{c2\|ab}(0)$ and its doping dependence is shown in Fig. 7.13(a). A large zero temperature critical field is found in the underdoped and optimally doped films, and a dramatic decrease of $H_{c2\|ab}(0)$ is observed for the overdoped films. A similar trend was found in the doping dependence of $H_{c2\perp ab}(0)$ [47, 107], both $H_{c2\|ab}(0)$ and $H_{c2\perp ab}(0)$ decrease rapidly in the overdoped region compared to the underdoped, although the T_c of underdoped films drops even faster.

6.3 Discussion

We have established an experimental parallel field H-T diagram for PCCO. Now let us compare our data with theory. For most conventional superconductors, WHH theory can quantitatively explain the temperature dependence of the upper critical field. For the layered high-T_c cuprates, in the H⊥ab configuration, it is found that the upper critical field is in good agreement with the WHH theory except for some unexplained low temperature upward curvature [105]. This implies that the

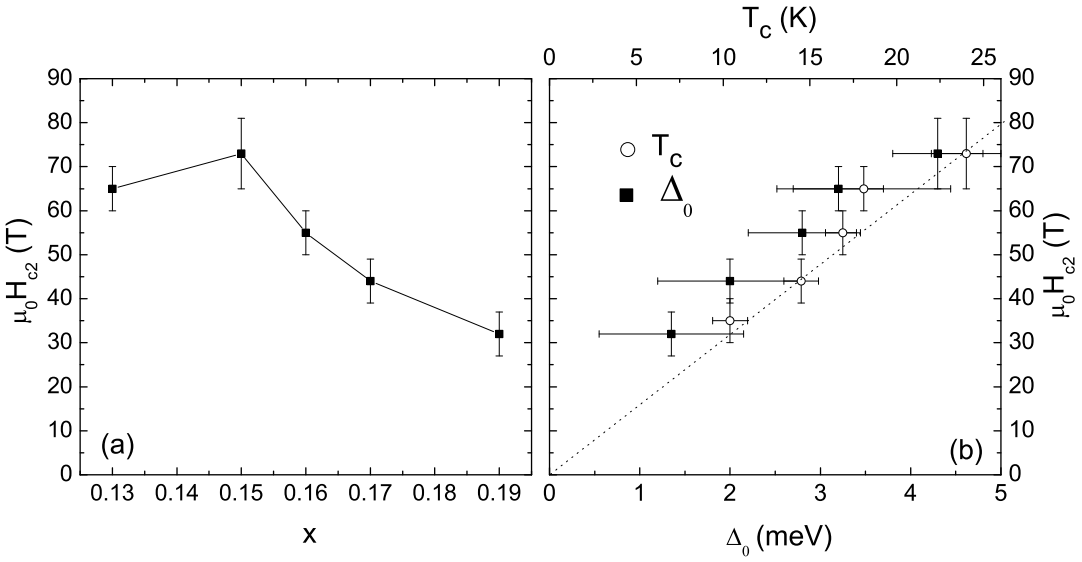

Figure 6.4: (a) Doping dependence of extrapolated $H_{c2\|ab}(0)$. (b) $H_{c2\|ab}(0)$ as a function of T_c(determined from Nernst effect measurement [106]) and superconducting gap $\triangle_0$.

diamagnetic orbital effect dominates the paramagnetic spin effect in the destruction of the superconductivity. In the H‖ab geometry, we attempted to compare our data with WHH theory (dotted lines in Fig. 6.3) by using the initial slopes of the H-T plots. As shown in Fig. 6.3, for the films near optimal doping (x=0.15 and 0.16), we found that WHH curves depart strongly from the experimental data at low temperatures. To show this here, we take x=0.15 as an example. The zero temperature critical field obtained from the WHH formula $H_{c2}(0) = 0.693(-dH_{c2}/dT)\ |_{T=T_c}\ T_c$ is about 170 T(using the initial slope value at T_c, $dH_{c2}/dT\ |_{T=T_c}$=-11.5 T/K), which is much larger than the extrapolated value of 73 T. As seen in Fig. 6.3, the WHH value of $H_{c2}(0)$ is also larger than the experimental number for x=0.13 and 0.16. It appears that the WHH orbital theory only sets the upper bound of $H_{c2}(0)$ for these dopings. However, we find that for the overdoped films, x=0.17 and 0.19, the $H_{c2\|ab}(0)$ values are close to the WHH theoretical estimation.

For a layered superconductor, by neglecting the thickness of the conducting layers, Klemm *et al.* [108] predicted that the upper critical field would diverge for temperature below a certain value T* where the out-of-plane coherence length ξ_c decreases to the value $d/\sqrt{2}$ (d is the distance between the conducting layers) and a dimensional crossover from 3D to 2D would occur at low temperature. The critical magnetic field to decouple the layers at T* was predicted to be $H_c=\phi_0/d^2\gamma$ ($\gamma = H_{c2\|ab}/H_{c2\perp ab}$). Experimentally, the low temperature saturation in the H-T phase diagram for H‖ab is contrary to this prediction and no trace of a dimensional crossover is observed. The predicted H_c, which is about 765 T for x=0.15 (d=6 Å and $\gamma \sim$8, a similar number is found for the other dopings), is also very large. By

considering the thickness (t) of the conducting layers, it has been found [109, 110] that the parallel critical field can be rewritten as $H_{c'} = \sqrt{3}\phi_0/\pi t\xi_{ab}$. From our perpendicular critical field data [47], we can get the in-plane coherence length ξ_{ab} via the Ginzburg-Landau equation $H_{c2\perp ab} = \phi_0/2\pi\xi_{ab}^2$. Setting the corresponding values of x=0.15 (t=3 Å $\xi_{ab}(0)$=60 Å), we find $H_{c'}$=582 T, which is still much higher than our measured value.

We now discuss paramagnetic (Pauli) limitation of the parallel critical field. In this case, the electron spins couple with the applied field and when the spin Zeeman energy reaches the pairbreaking energy, the Cooper pair singlet state is destroyed. An early theory by Clogston and Chandrasekhar [111] estimated the paramagnetic limit based on the isotropic BCS theory and predicted the Pauli paramagnetic limit $H_P = \triangle_0/\mu_B\sqrt{2}$. Under the assumption $2\triangle_0 = 3.5k_BT_c$, we have $H_P(0) = 1.84T_c\frac{T}{K}$. Applying this to our x=0.15 doping (T_c=21.3 K), we get $H_P(0)$=39 T. This is much smaller than our experimental value of 73 T. If we take $\triangle_0$=4.3 meV (maximum gap value) from the optics results [107, 112], then $H'_P(0)$=53 T. For the other dopings, we find that the Clogston theory also underestimates the measured values. This suggests that a simple BCS s-wave model for the paramagnetic limit is not valid for PCCO. This is not surprising since PCCO is believed to be a quasi two dimensional d-wave superconductor. Recent work by Yang [113] estimated the paramagnetic limit for a d-wave superconductor in a purely 2D system by only considering the coupling of the spins of the electrons and the applied field and found that $H_P(0) = 0.56\,\triangle_0/\mu_B$. This is even smaller than the s-wave case due to the existence of nodes in the gap function.

The experimental critical field often exceeds the theoretical predictions for the Pauli limit, even in some conventional s-wave superconductors. To explain this, some other possibilities were introduced, such as spin-orbit coupling to impurities. It was found that the spin-orbit scattering enhances the Pauli critical field over the spin-only value for s-wave symmetry [98, 108]. However, it has been shown [114] that the spin-orbit interaction significantly lowers the critical field for d-wave symmetry. Therefore, the enhancement of the parallel critical field in PCCO is not caused by the spin-orbit coupling.

Despite the discrepancy between theory and data, we find that our extrapolated $H_{c2\|ab}(0)$ can be scaled with both T_c and superconducting gap $\triangle_0$. As seen in Fig. 7.13(b), $H_{c2\|ab}$ is linearly proportional to T_c and can be written in a Zeeman-like way, i.e., $k_B T_c = \frac{1}{4} g \mu_B H_{c2\|ab}(0)$, where g=2 is the electronic g factor, μ_B the Bohr magneton. This suggests that the thermal energy at T_c and the electronic Zeeman energy at $H_{c2\|ab}(0)$ give the single energy scale required to destroy the phase coherence. We note that, for the underdoped x=0.13 and optimally-doped x=0.15, due to the superconducting fluctuation, we determined T_c from the temperatures at which the vortex Nernst effect disappears, which is 18 K and 24 K for 0.13 and 0.15, respectively. This temperature is slightly higher than the resistive transition temperature [106]. For the overdoped films, both tunneling [115] and Nernst effect measurements show that the fluctuation is much weaker, therefore, T_c can be reliably taken from resistivity measurement. Meanwhile, if we compare the Zeeman energy and the maximum superconducting gap values obtained from optics experiments [107, 112], we find that $g\mu_B H_{c2\|ab}(0) \simeq 2\triangle_0$, i.e., $\mu_B H_{c2\|ab}(0)/\triangle_0 \simeq 1$, as

shown in Fig. 7.13. This strongly suggests that the magnetic Zeeman energy reaches the superconducting gap, and thus the superconductivity is destroyed. It has been shown that due to possible quantum fluctuations, the superconductivity can be destroyed within a Zeeman energy interval [116], $\frac{1}{2}\triangle \leq \mu_B H_{c2\|ab} \leq 2\triangle$. Therefore, our results strongly suggest the Pauli paramagnetic limit is responsible for the high field depairing process.

Finally, it is worth mentioning that the SC gap to parallel critical field ratio in some hole-doped cuprates was also found to be roughly one. [100, 105] It seems that in the layered quasi-2D cuprate superconductors, the parallel critical field is universally determined by the paramagnetic limit, suggesting that diamagnetic orbital pair-breaking effect is negligible compared to the spin effect due to a much shorter out-of-plane coherence length.

6.4 Conclusion

In summary, we measured $H_{c2\|ab}$ in electron-doped cuprates $Pr_{2-x}Ce_xCuO_{4-\delta}$ from the underdoped to the overdoped region. We found that the critical field anisotropy, $H_{c2\|ab}/H_{c2\perp ab}$ is about 8. We also found that the Zeeman splitting energy $\mu_B H_{c2\|ab}(0)$ reaches the superconducting gap $\triangle_0$, which strongly suggests that the Pauli paramagnetic limit is responsible for quenching superconductivity in electron-doped cuprates for H parallel to the CuO_2 planes.

Chapter 7

Nernst Effect in $Pr_{2-x}Ce_xCuO_{4-\delta}$

7.1 Nernst effect in type II superconductor

In chapter 2, we discussed the Nernst effect for a normal metal within the Drude and Boltzmann frameworks. In this section, we briefly review the vortex Nernst effect in a type II superconductor and its application to probe superconducting fluctuations [68].

For superconductors with a Ginzburg-Landau (GL) parameter $\kappa = \lambda/\xi$ (λ the penetration depth and ξ the coherence length) larger than $1/\sqrt{2}$, it is energetically more favorable for the external magnetic field to penetrate the superconductors as flux tubes, each carrying a flux quantum $\phi_\circ = h/2e$. This is in strong contrast to type I superconductors which tend to completely exclude the external field. These superconductors are called type II superconductors [117]. High-T_c cuprates have a large penetration depth $\lambda \sim 1000$ Å and a short coherence length $\xi \sim$ 10-100Å and therefore they are type II superconductors.

The flux tube in a type II superconductor has a vortex-like structure. As shown in Fig. 7.1, the order parameter $|\psi|$ is completely suppressed at the center, and only recovers the unperturbed $|\psi_0|$ over a length scale ξ. The local magnetic flux density maximizes at the center of the vortex and has a decay length λ, the penetration depth. Supercurrent circulates around the vortex core to screen the magnetic field

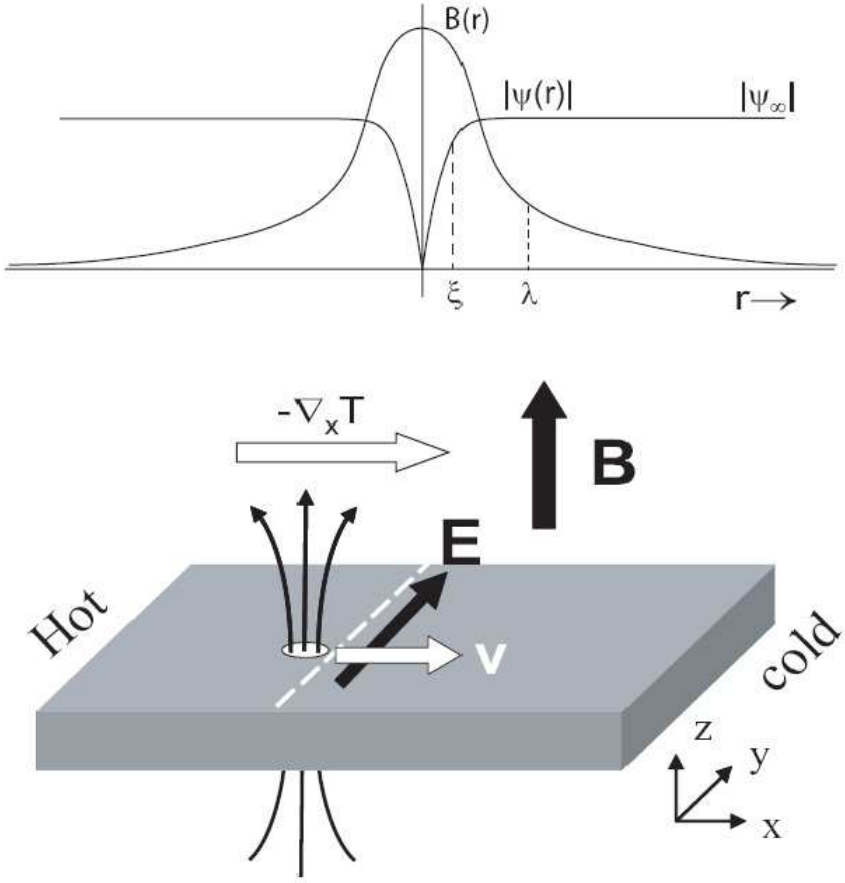

Figure 7.1: Top: the structure of a flux tube in a type II superconductor. The spatial variation of the order parameter ($|\psi|$) and the local flux density h with the relevant length scales [4]. Bottom: the motion of a vortex in a type II superconductor in the presence of temperature gradient $-\nabla_x T$ and magnetic field B_z generates a transverse electrical field E_y, the Nernst field.

from the bulk of the superfluid. When a Cooper pair travels completely around the vortex core, its phase θ must jump by 2π to ensure single value of the wave function. Therefore, each flux tube can be regarded as an excitation that carries a flux quantum $|\phi_0|$ and a 2π phase singularity.

Vortex motion can generate a transverse electrical field by the Josephson effect [118]. The Josephson equation relates the change of the phase of the macroscopic wave function with the electro-chemical potential V:

$$\frac{d\triangle\theta}{dt} = \frac{2eV}{\hbar} \tag{7.1}$$

where $\triangle\theta$ is the phase difference across two superconducting electrodes and V is the electro-chemical potential between them. Since each vortex carries a 2π phase singularity, it will cause a 2π phase slip as it crosses the line joining two transverse electrodes and will generate a pulse of voltage V. In an external field, the continuous flow of the vortices leads to a transverse electrical field. If the density of the vortices (number of vortices per unit area) is $n_v = B/\phi_0$, then the total phase change between the electrodes separated by distance l in the time interval dt is: $(d\triangle\theta) = 2\pi n_v l v dt$, v being the velocity of the vortices. Inserting this into the Josephson equation, we can get the transverse electrical field

$$\vec{E} = V/l = \vec{B} \times \vec{v} \tag{7.2}$$

This indicates that the electrical field E generated by the vortex motion is proportional to the external field B and the velocity of the vortices v. In the superconducting state with a longitudinal thermal gradient $\nabla_x T$, the vortices will move with velocity v_x and will induce a transverse electrical field $E_y = B_z v_x$ by Eq. 7.2.

This signal is called the vortex Nernst effect. In type II superconductors, the vortex Nernst effect is usually much larger than the Nernst signal from any thermally excited quasi-particles. The selective sensitivity of the Nernst effect to the vortex motion makes it a good probe to study the properties of the mixed state of type II superconductors.

In a single vortex picture, when the magnetic field is weak, there are only a few non-interacting vortices. Each normal vortex core carries an entropy of S_ϕ and the entropic force (thermal force) exerted on it by the temperature gradient $(-\nabla T)$ is $f_\phi = S_\phi(-\nabla T)$ [119]. In the steady state, this entropic force is balanced by the damping force $f_\eta = \eta v$, where η is the viscosity. Thus the vortex Nernst field is

$$\begin{aligned} e_y &= \frac{E_y}{|-\nabla T|} = \frac{B_z v_x}{|-\nabla T|} \\ &= B_z S_\phi/\eta. \end{aligned} \tag{7.3}$$

η can be obtained from flux flow resistivity measurement, in which the Lorentz force $\vec{f_L} = \vec{j} \times \vec{\phi_0}$ on the vortex is balanced by the damping force, therefore, we have $j_x\phi_0 = \eta v$, which gives the flux flow resistivity [119]

$$\rho_f = E_y/j = |\vec{B} \times \vec{v}|/j_x = B_z\phi_0/\eta, \tag{7.4}$$

then the vortex Nernst signal is

$$e_y = \frac{\rho_f S_{\phi_0}}{\phi_0} \tag{7.5}$$

which is proportional to the flux flow resistivity and the entropy of each vortex core.

In contrast to the linear magnetic field dependence of normal state quasi-particles (see chapter 2), the vortex Nernst signal has a nonlinear magnetic field

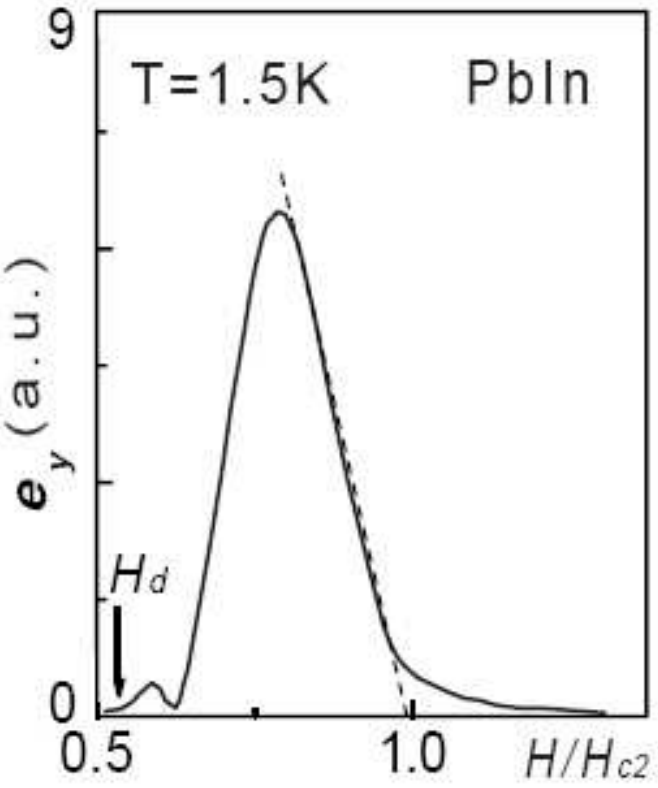

Figure 7.2: The Nernst effect of a conventional low-T_c superconductor PbIn as a function of magnetic field. The large peak is the vortex-Nernst peak which diminishes very quickly to zero above H_{c2} [120].

dependence. Shown in Fig. 7.2 is vortex Nernst signal in a conventional superconductor PbIn. Notice that the vortex Nernst effect is zero until a certain depinning field at which the vortices become mobile. With increasing field both the number of vortices and their mobility increases, and hence the vortex Nernst signal increases dramatically. Above a certain field the vortex Nernst signal starts to decrease because the mobility of the vortices decreases due to enhanced vortex-vortex interactions and this dominates the increase in their number. Therefore the vortex Nernst signal peaks at a certain field and decreases afterwards, reaching zero at a field close to H_{c2}. It is in principle easy to separate the vortex Nernst signal from the normal state Nernst signal because of their very different field dependences and magnitudes.

7.2 Nernst effect as a probe of superconducting fluctuations

As discussed in chapter 1, in the underdoped hole-doped cuprates it is found that a partial energy gap opens at a characteristic temperature T^*. To distinguish it from the gapped superconducting phase below T_c, the region between T^* and T_c is called the "pseudogap" region [32]. One of the possible explanations of the "pseudogap" is amplitude and/or phase fluctuations of the superconducting order parameter. Superconducting fluctuations in a simplest form are small regions of normal material becoming superconducting by releasing thermal energy to their vicinity [121, 122, 123]. For this to be possible the temperature should be close to the transition temperature, and the limit for closeness is set by the energy required

to create Cooper pairs. Since the superconducting region can not be smaller than the size of a Cooper pair (ξ, the coherence length), the minimum required energy to create a superconducting fluctuation in 2D is proportional to ξ^2, the area of the region becoming superconducting. The coherence length of the cuprates is usually two orders of magnitude smaller than in the conventional superconductors. In addition, the transition temperature T_c is much higher in the cuprates, which makes fluctuations in the thermal energy larger. Therefore, it is much easier to create superconducting fluctuations in cuprates compared to the conventional superconductors, and hence the fluctuations occur over a wider temperature region above T_c in cuprates [124].

The Nernst effect is one sensitive probe of superconducting fluctuations. The sensitivity of the Nernst effect is due to the negligibly small Nernst effect of normal carriers and the relatively large vortex Nernst signal characteristic of the mixed state [119]. Therefore, at temperatures above T_c in the presence of a large magnetic field, vortex excitations could survive in the fluctuation regime, and the motion of these vortices could generate a large Nernst signal compared to the normal state quasi-particle signal.

In fact, recent Nernst effect measurements on hole-doped cuprates have shown very surprising results [65, 99, 125]. Especially in the under-doped regime of these cuprates, as seen in Fig. 7.3, an anomalous Nernst signal has been observed to persist to temperatures up to 50- 100 K above T_c (and to magnetic fields much larger than the resistive H_{c2}). It was argued that this anomalous signal above the conventional T_c or H_{c2} is evidence for vortex-like excitations above T_c or H_{c2}. The

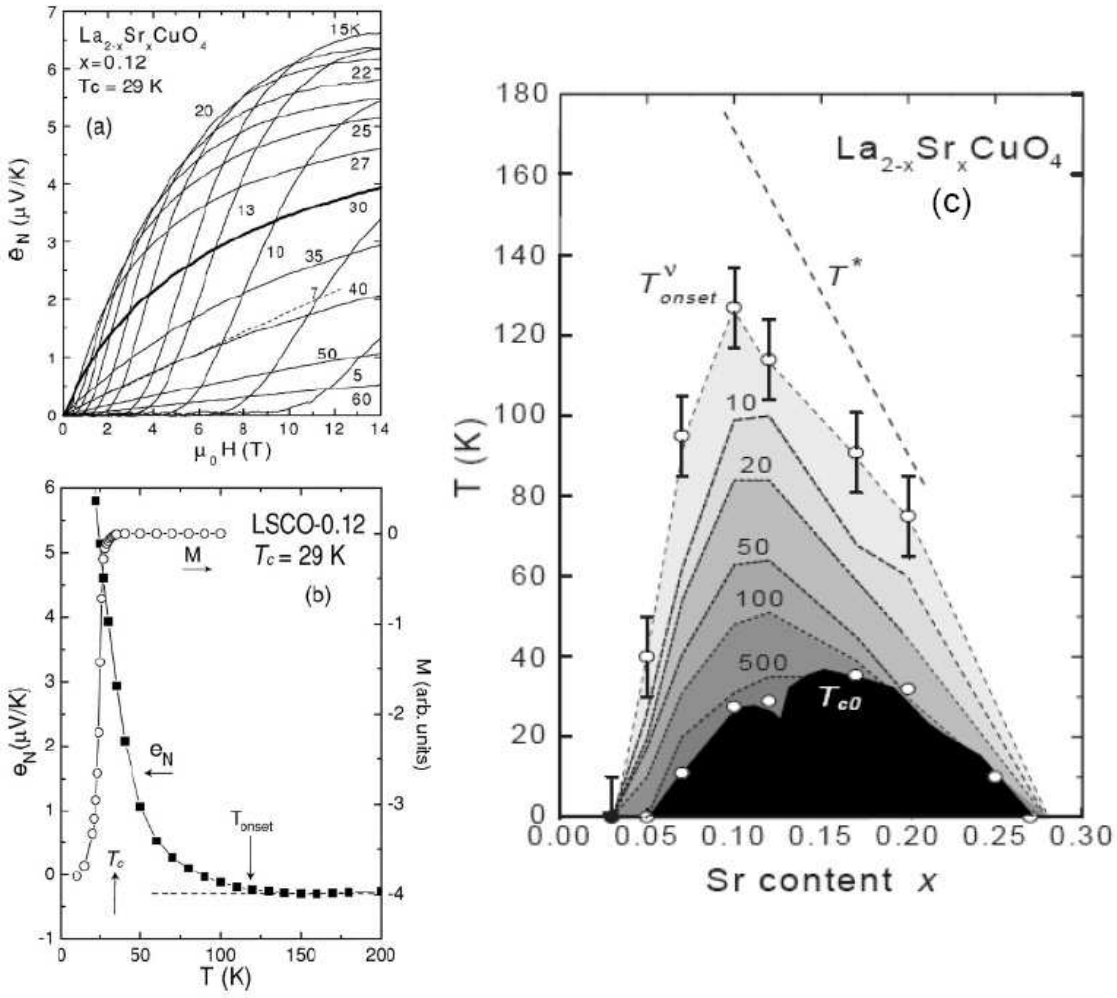

Figure 7.3: Nernst effect in an underdoped $La_{2-x}Sr_xCuO_4$ (x=0.12)(taken from Ref. [99]). (a) Magnetic field dependence of the Nernst signal. The data for T>T_c is quite anomalous compared to conventional low-T_c superconductors. (b) The temperature dependence of e_y measured at 14 T in an underdoped LSCO (solid squares) compared with the magnetization. Dashed line is the negative quasi-particle contribution. (c) The phase diagram of LSCO showing the Nernst region between T_c and T_{onset} (or T_ν) (numbers on the contour curves indicate the value of the Nernst coefficient ν in nV/KT). The dashed line is T^* from heat-capacity measurements.

onset temperature of the anomalous Nernst effect, T_ν, is then the onset of Cooper pair formation. In this picture there is a temperature (or field) at which the Cooper pairs start to form, and another temperature (or field) below which the Cooper pairs attain phase coherence throughout the sample. Therefore, the T_c (or H_{c2}) of resistivity measurements corresponds to the temperature (or field) that phase coherence has been obtained, whereas the onset of the anomalous Nernst signal corresponds to the temperature (or field) of the Cooper pair formation. In other words, the large Nernst signal results from vortex degrees of freedom which arise when the amplitude of order parameter remains fixed to temperatures significantly higher than the zero field T_c while the phase is allow to fluctuate. The onset temperature of the Nernst signal then is taken to be a measure of the onset of the phase fluctuation regime [126].

Inspired by the unusual Nernst effect measurements in hole-doped cuprates, many theories to explain the data have been proposed. We mention two of the theories that deal with amplitude and phase fluctuations of the superconducting order parameters. Ussishkin *et al.* [127] suggest that Gaussian amplitude fluctuations (fluctuations with only consideration of the quadratic terms in the Landau-Ginzburg functional) above T_c are responsible to the Nernst effect for the optimally-doped and overdoped regimes. However, for the underdoped regime they suggest that strong non-Gaussian fluctuations reduce the mean-field transition temperature T_c^{MF}, the theoretical transition temperature in the absence of any fluctuations, and therefore the mean field T_c^{MF} should be used in calculations instead of the actual T_c in order to take into account the contribution of the non-Gaussian fluctuations to the Nernst

effect. Another explanation involves the important and influential work of Emery and Kivelson [126], which preceded the Nernst effect measurements in underdoped cuprates, and the follow-up work of Carlson *et al.* [128]. In this theory, the stiffness to phase fluctuations is determined by the superfluid density (the density of superconducting electrons), ρ_s: the smaller the superfluid density, the more significant the phase fluctuations [126]. In conventional superconductors, the superfluid density ρ_s is very large [4, 126]. Phase rigidity, or the strength of the phase coherence, is so strong that pairing and long-range order phase coherence occur simultaneously at the transition temperature T_c. The phase degree of freedom plays an insignificant role in determining the transition temperature and other relevant properties. However, in the high-T_c superconductors with a small superfluid density, the long-range phase coherence is destroyed at T_c while the local Cooper pairing amplitude remains sizable to higher temperatures.

Beside those fluctuation theories, other theories claim to provide an explanation of the anomalous Nernst effect in the hole-doped cuprates [129, 130, 131, 132, 133, 134]. However, none of these explanations have gained general acceptance.

In contrast to the hole-doped cuprates, the electron-doped cuprates have shown two different normal state gaps: a low energy gap, with a size comparable to the superconducting gap, observed in tunneling spectroscopy when the superconductivity is suppressed with magnetic field [115, 135], and a high energy gap similar to the pseudogap in the hole-doped cuprates, found in the optical conductivity [57, 136], Raman spectroscopy [137] and photoemission measurements [138]. Recent Nernst effect experiments [48, 99, 106] in the electron-doped cuprates near optimal doping

suggested that electron-doped cuprates are more conventional than their hole-doped counterparts, and that superconducting fluctuations are much weaker. Almost no vortex-like Nernst signal was observed above T_c. However, a large normal state Nernst signal was observed, which was explained by a two-carrier (electron and hole) quasi-particle contribution [47, 48]. The large normal state Nernst signal in electron-doped cuprates has a distinctively different temperature and field dependence from the vortex Nernst signal found in the hole-doped cuprates. However, it is possible that the large normal state quasi-particle Nernst signal masks a smaller vortex Nernst signal at temperatures above T_c.

In this chapter, a careful study of the vortex Nernst effect in the electron-doped cuprate system $Pr_{2-x}Ce_xCuO_{4-\delta}$ (PCCO) films is presented and the superconducting fluctuation contribution is reexamined. The normal state Nernst effect in PCCO is also studied in a wide range of doping and temperature. Possible explanations for all this new data will be presented and discussed.

7.3 Vortex Nernst effect in $Pr_{2-x}Ce_xCuO_{4-\delta}$

7.3.1 Experiments and results

$Pr_{2-x}Ce_xCuO_{4-\delta}$ films for Nernst effect measurements were fabricated by pulsed laser deposition on $SrTiO_3$ substrates. Details of film fabrication and characterization were given in chapter 3 and Ref. [69, 70]. The films of size 10×5 mm^2 used in Nernst effect experiments were patterned into a standard Hall bar geometry by ion-mill technique. The Nernst effect measurements were performed using the one-

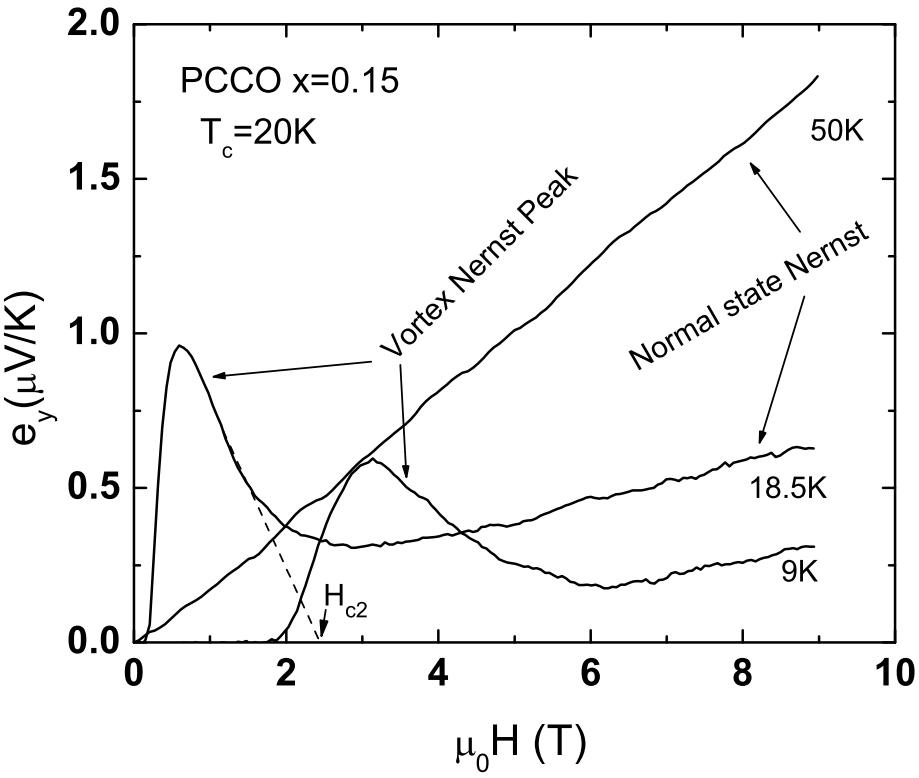

Figure 7.4: Nernst effect in an optimally-doped x=0.15 PCCO film at different temperatures.

heater-two-thermometer technique as described in chapter 3. The Nernst voltage is measured by a Keithley 2001 multimeter with a 1801 preamp while the magnetic field is slowly ramped at a rate of 0.3 T/min between -9 T and 9 T (H$\|$c). The Nernst signal is obtained by subtracting negative field data from positive field data to eliminate any possible longitudinal thermopower contribution.

Fig. 7.4 illustrates the vortex Nernst effect and the normal state Nernst signal in an optimally-doped PCCO film. Below T_c and H_{c2}, a sharp and large vortex

Nernst peak is seen, which starts from the depinning (melting) field. Above H_{c2}, the Nernst signal is linear in field, as also found when the temperature is above T_c. This linear field dependent Nernst signal is attributed to the normal state quasi-particles (see chapter 2). In this figure, we also show a normal state Nernst signal for $T>T_c$ (T=50 K). The normal state Nernst signal at T=50 K at the higher fields is even larger than the peak in the vortex Nernst signal below T_c. This is in striking contrast to hole-doped cuprates, in which the quasi-particle Nernst signal is much smaller than the vortex Nernst signal, as seen in Fig. 7.3 [65]. To obtain the net vortex Nernst signal, the linear normal state Nernst signal can be subtracted from the measured data.

We carefully studied the Nernst effect around T_c to search for possible superconducting fluctuation effects in PCCO, especially in the underdoped regime. Fig. 7.5 shows the low temperature vortex Nernst effect result for an underdoped film x=0.13 (T_c=11.8 K, from the peak temperature of the imaginary part of susceptibility, see Fig. 3.2) after subtraction of the linear normal state Nernst signal. The peak-featured vortex Nernst signal is observed to persist to temperatures higher than T_c. As seen in Fig. 7.5, the vortex Nernst signal is still robust at T=17.5 K, which is about 6 K higher than T_c. When temperature is well above T_c (T>20 K for x=0.13), the vortex Nernst signal vanishes and the quasi-particle linear in field Nernst signal is recovered. The Nernst effect measurement was also performed on PCCO films with dopings x=0.14, 0.15, 0.16, 0.17, 0.19. For x=0.14 and x=0.15, the result is similar to x=0.13, but the onset temperature of the vortex Nernst signal (temperature where a vortex Nernst peak appears) is about 4 K above T_c for

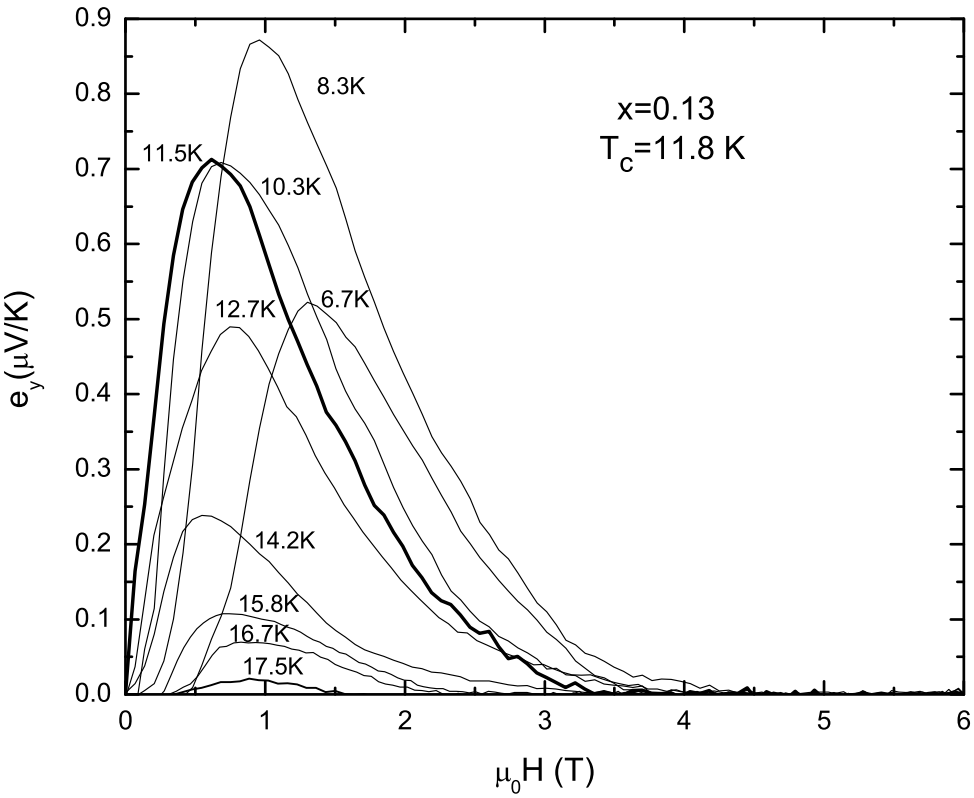

Figure 7.5: Vortex Nernst effect in an underdoped x=0.13 PCCO film at different temperatures.

x=0.14 and 3 K above T_c for x=0.15. However, in the overdoped films, the vortex Nernst signal vanishes at the superconducting transition temperature T_c. Moreover, the linear quasi-particle Nernst signal emerges when temperature is just above T_c, suggesting that the normal state is recovered very close to T_c, with minimal superconducting fluctuations.

Fig. 7.6 displays the onset temperature of the vortex Nernst signal along with the superconducting transition temperature T_c as a function of doping for PCCO. It is clear that in the underdoped region the difference between these two characteristic temperatures is larger than the overdoped side, suggesting a larger superconducting fluctuation effect in the underdoped region with a more conventional behavior in the overdoped region.

7.3.2 Discussion

How do we understand the superconducting fluctuations in the electron-doped cuprates? It is known that superconductivity is characterized by a complex order parameter $|\psi|exp(-i\theta)$, with an amplitude $|\psi|$ and a phase θ at each space point [4]. Fluctuations in either amplitude or phase will affect the superconducting properties. The conventional fluctuation theories primarily deal with thermal fluctuations of the amplitude $|\psi|$ of the order parameter [4, 124]. By solving the time-dependent Ginzburg-Landau equation in the Gaussian approximation, Ussushkin *et al.* [127] calculated the transverse thermoelectric coefficient which results from the amplitude

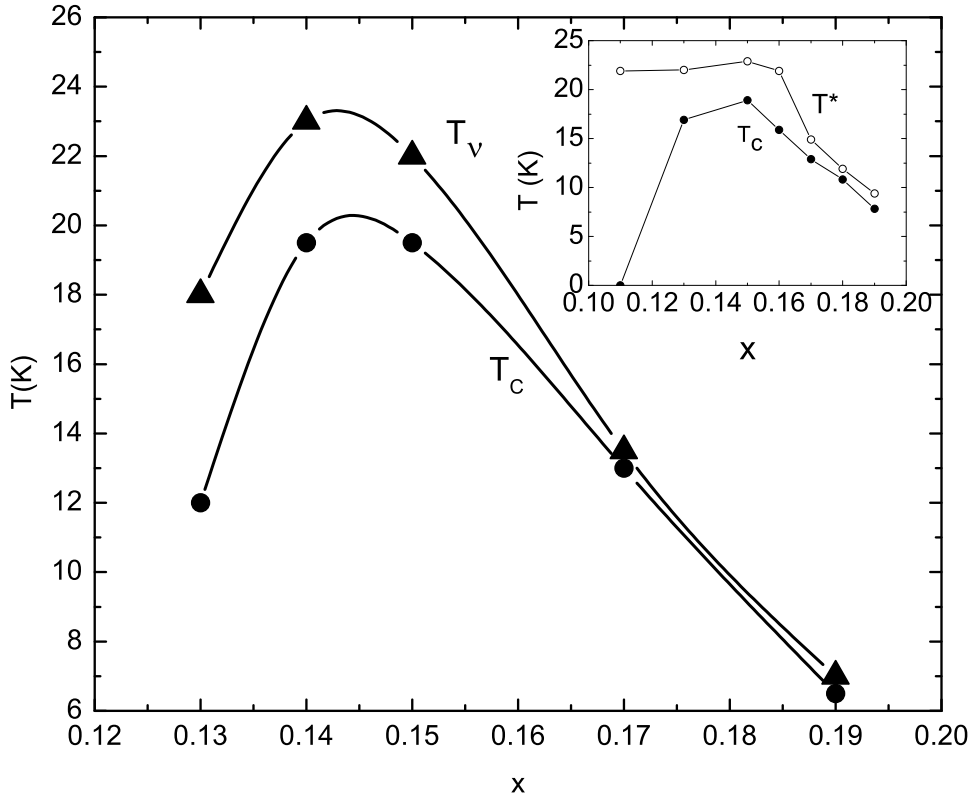

Figure 7.6: Doping dependence of T_c and onset temperature T_ν of vortex Nernst signal (error bar is the size of the dot). Inset shows recent planar tunneling data in PCCO [115].

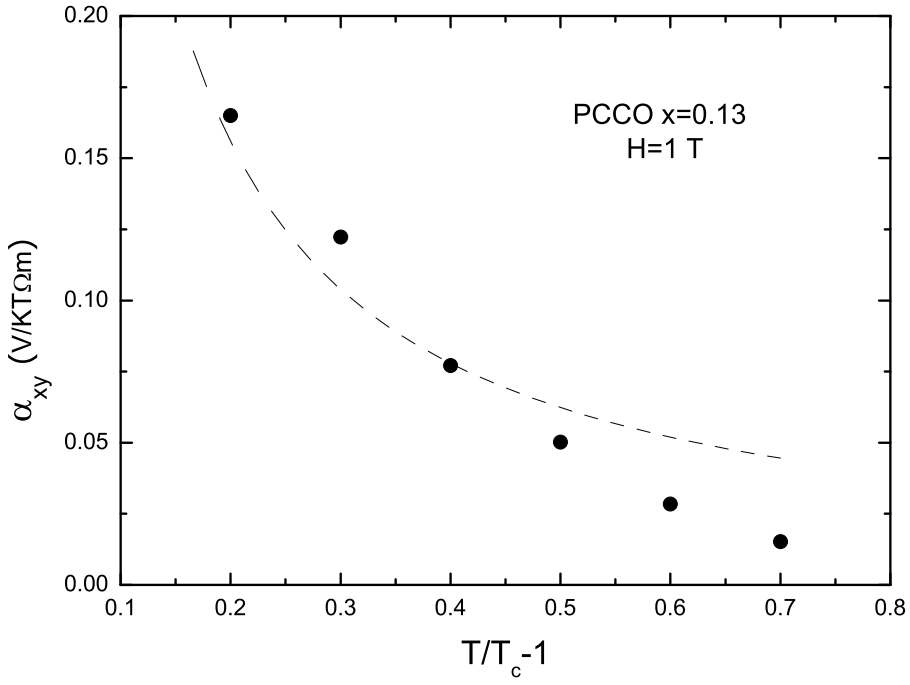

Figure 7.7: Off-diagonal Peltier conductivity α_{xy} of PCCO x=0.13 at H=1 T. Dashed line is the fit using Eq. 7.7.

fluctuations:

$$\alpha_{xy}^{SC} = \frac{1}{6}\frac{e}{\hbar}\frac{\xi^2}{l_B^2} \propto \frac{1}{T - T_c} \tag{7.6}$$

where $l_B = (\phi_0/B)^{1/2}$ is the magnetic length. For 2D superconductors, using the Lawrence-Doniach model, this can be rewritten as

$$\alpha_{xy}^{SC} = \frac{1}{6}\frac{e}{\hbar}\frac{\xi_{ab}^2}{l_B^2 s}\frac{1}{\sqrt{1 + (2\xi_c^2/s)^2}} \tag{7.7}$$

where $\xi_{ab(c)}$ is the in-plane (out of plane) coherence length and s the distance between adjacent layers.

The vortex Nernst signal, $e_y = \alpha_{xy}^{SC}/\sigma_{xx}$ [99], is mainly proportional to the in-plane coherence length ξ_{ab}. In the electron-doped cuprates, the in-plane coherence length increases with doping (H_{c2} decreases rapidly with doping [97]) and thus from Eq. 7.7 one would expect a stronger fluctuation effect as doping increases. However, the weakness of fluctuation effects in the overdoped PCCO compared to underdoped contradicts this theoretical expectation. Therefore, the strong fluctuation effects that are found in the underdoped region are probably not caused by amplitude fluctuations. In addition, compared to the hole-doped cuprates (e.g. LSCO), electron-doped cuprates have a much longer coherence length (about one order of magnitude larger [97, 106]), yet a weaker fluctuation effect is observed: the fluctuation regime, $\triangle T_{fl} = T_\nu/T_c - 1$ is about 0.5 for PCCO with x=0.13 and 4 for LSCO with x=0.1 (T_c=20 K) [65]. These two effects suggest that conventional amplitude fluctuation theory can not explain the Nernst effect results in underdoped electron-doped cuprates. Also, we find that the off-diagonal Peltier conductivity α_{xy}^{SC} does not follow the theoretical expectation (Fig. 7.7), again suggesting that the fluctuations in electron-doped cuprates are not amplitude fluctuations.

Now we turn to phase fluctuations, which are claimed to explain the anomalous Nernst effect in the hole-doped cuprates. In conventional superconductors, phase fluctuations plays an insignificant role in determining the transition temperature because of the large superfluid density ρ_s. However, in the high-T_c superconductors, the proximity to the Mott insulator leads to a very small superfluid density. Therefore, it is possible that long-range phase coherence is destroyed at T_c while the local Cooper pairing amplitude remains sizable. The significance of

the phase fluctuation can be assessed by evaluating the phase stiffness temperature, $T_\theta^{max} = A\rho_s(0)d/m^*$ [126], at which phase order would disappear (here d the spacing between adjacent CuO_2 layers, A=0.9 is a numeric factor for quasi-2D systems and m^* the effective mass). If $T_c \ll T_\theta^{max}$, phase fluctuations are relatively unimportant, and T_c will be close to the mean-field transition temperature, T_c^{MF}, as predicted by BCS theory. On the other hand, if $T_\theta^{max} \approx T_c$, then T_c is determined primarily by phase ordering, and T_c^{MF} is simply the characteristic temperature below which pairing becomes significant locally. In conventional superconductors, T_θ^{max} is orders of magnitude larger than T_c, and phase coherence is so strong that T_c is the pairing temperature. In the overdoped hole-doped cuprates, T_θ^{max}/T_c is around 2-5, suggesting that phase fluctuations become more important. In the underdoped hole-doped cuprates, T_θ^{max} is very close to T_c, suggesting that phase fluctuations are dominant in determining the superconducting phase transition. The fluctuations suppress the transition temperature from the mean-field value T_c^{MF}, at which Cooper pairs form, to the observed T_c where long-rang phase coherence is established. In the electron-doped cuprate PCCO, penetration depth measurements gave $\lambda^{-2}(0)$=9, 15 and 40 μm^{-2} for x=0.13, 0.15 and 0.17 respectively [140]. Using the relation $\rho_s(0) = m^*/e^2\lambda^2(0)$, we can estimate the T_θ^{max}/T_c value for PCCO. Simple calculation gives T_θ^{max}/T_c=2, 2.4 and 11 for 0.13, 0.15 and 0.17 respectively. Thus, phase fluctuations are strongly suppressed in the overdoped region since $\frac{T_\theta^{max}}{T_c} \gg 1$ and then $T_c \approx T_c^{MF}$. Although the values of T_θ^{max}/T_c of the underdoped and optimally-doped PCCO are close to those of optimally-doped and overdoped LSCO, the fluctuation regime is much narrower in PCCO than LSCO ($\triangle T_{fl}$=0.5 for PCCO

with x=0.13, 1.2 and 1.5 for LSCO x=0.17 and 0.2 respectively [65]). A possible reason for this could be the weaker coupling of the Cooper pairs in the electron-doped cuprates. The formation of the superconducting state requires both the formation of the Cooper pairs (determined by the pairing strength as measured by the energy gap $\triangle$) and establishment of phase coherence between different pairs (related to $\rho_s(0)$). The destruction of the superconducting state as temperature is increased is determined by the weaker of these effects. In conventional low-T_c superconductors the pairing strength is the weaker effect and hence, it determines the disappearance of superconductivity. For PCCO (x=0.13), the pairing strength measured by the superconducting gap is about 4 meV, much smaller than the gap value (>15 meV) for the underdoped LSCO [141]. Therefore, the value of $2\triangle/k_BT_c$ is much smaller in PCCO ($\sim$ 4) than in LSCO ($\sim$ 10). This suggests that the temperature driven pair-breaking effect is stronger in PCCO. Thus, the thermal pair breaking competes with the phase fluctuation effect and reduces the size of the fluctuation region in electron-doped cuprates.

Our resistivity measurements on the underdoped and optimally-doped PCCO films also show some interesting results. As displayed in Fig. 7.8, the blue curves are the zero-field resistivity of x=0.13 and 0.15. In order to eliminate the negative magnetoresistance in these dopings, we measured the in-plane resistivity versus field at different temperatures and extrapolated the data to get the "effective" zero-field normal state resistivity [the inset to Fig. 7.8(a) shows one example of this procedure]. Its temperature dependence is shown as red curve in Fig. 7.8. The arrows mark the temperature where the zero-field resistivity deviates from the zero-field normal state

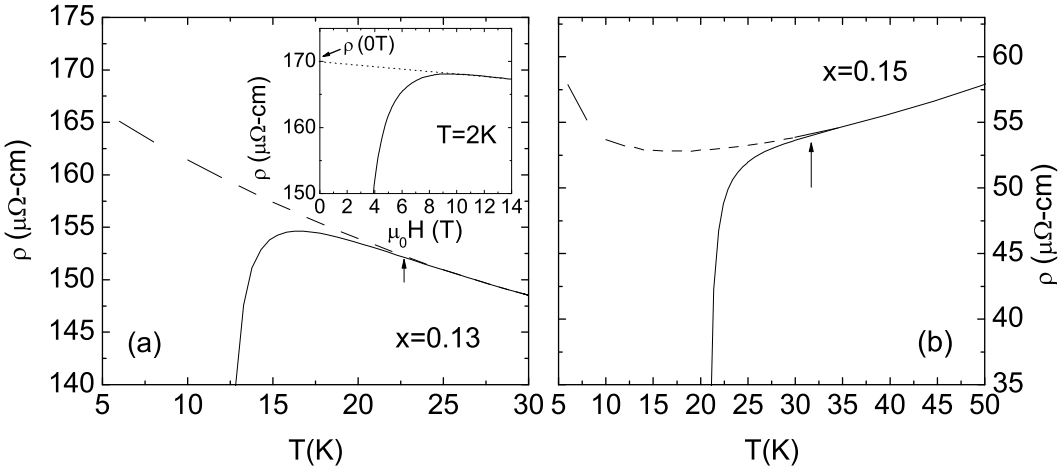

Figure 7.8: Paraconductivity of the underdoped x=0.13 (a) and optimally-doped x=0.15 (b) PCCO films. Inset shows the procedure of obtaining the zero-field normal state resistivity [dashed curves in (a) and (b)].

resistivity. Interestingly, the onset temperature of the deviation is slightly higher than the onset temperatures of the vortex Nernst effect in both underdoped and optimally-doped samples. Although the excessive conductivity (paraconductivity) is often attributed to amplitude fluctuations [124], this is not clear in the PCCO case because of the large resistivity upturn at low temperatures at these dopings. Also, tunneling experiments [115] suggest a superconducting pseudpgap opens at higher temperature above T_c. The depression of the density of states leads to the increasing of the conductivity. Therefore, the competition between the insulating upturn and the superconducting pseudogap could be the reason of the excessive conductivity in the normal state.

Finally, it is worth mentioning that a planar tunneling experiment in PCCO observed a normal state energy gap (pseudogap) throughout the entire doping range [115]. This normal state gap persists to a temperature higher than the superconducting transition temperature T_c in the underdoped region but follows T_c on the overdoped side (inset of Fig. 7.6). This was interpreted as a result of finite pairing amplitude above T_c in the underdoped region. Interestingly, the onset temperature of the vortex Nernst signal extends well into this region, suggesting that it may be related to the normal state gap seen in tunneling.

7.3.3 Conclusion

To conclude this part, we have investigated superconducting fluctuation effects in PCCO films by Nernst effect measurements. We found that the fluctuations are

stronger in the underdoped region than in the overdoped region. We excluded amplitude fluctuations as an explanation for this observation, and found that phase fluctuations could be responsible for the normal state vortex signal found in our underdoped films. This is consistent with the anomalous Nernst effect in the hole-doped cuprates.

7.4 Normal state Nernst effect in $Pr_{2-x}Ce_xCuO_{4-\delta}$

7.4.1 Introduction

Prior Nernst effect and other transport studies on electron-doped cuprates with different oxygen doping suggested the coexistence of two electronic subsystems (i.e. hole and electron bands) around the optimal doping of Ce=0.15 [46, 47, 48]. This two-band behavior was later confirmed by ARPES [50, 51] as discussed in chapter 1. The Fermi surface (FS) evolves from a Mott insulator parent compound to an electron-like FS centered at (π,0) in the underdoped region. At optimal doping, one finds a hole-like FS pocket centered at ($\pi/2$, $\pi/2$) and an electron-like pocket near (π, 0)and (0, π). From this evolution of the band structure with doping, one expects a hole-like FS centered at (π, π) in the overdoped region. In fact, Matsui *et al.* [53] recently observed a large hole-like pocket in an overdoped $Nd_{1.83}Ce_{0.17}CuO_4$ from ARPES experiments.

Most of the prior transport measurements were performed on optimally-doped $Nd_{1.85}Ce_{0.15}CuO_{4-\delta}$ and the charge doping was varied by oxygen content. An anomalously large Nernst effect and magnetoresistance and a sign change of the Hall coeffi-

cient and thermopower were observed in the oxygen-doped NCCO films [46, 47, 48]. The evolution of these transport properties with oxygen reduction suggested that the hole band is controlled by the oxygen content: a single electron band in the fully oxygenated regime, a two-band regime in the optimal oxygenated superconducting phase and a hole-like band in the deoxygenated state. Recently, Balci *et al.* [106] observed a large normal state Nernst signal in $Pr_{2-x}Ce_xCuO_{4-\delta}$ films with Ce concentration varied around optimal-doping. This is consistent with the previous results on the oxygen-doped NCCO. However, more detailed studies of the Nernst effect in electron-doped cuprates over a wider range of Ce concentration is lacking. It is important to investigate the transport properties in the very underdoped or overdoped regimes since useful information could be obtained for further understanding of the band structure (and scattering) at the extreme dopings. In this section, we will present our extensive magnetic field driven normal state Nernst effect measurements on $Pr_{2-x}Ce_xCuO_{4-\delta}$ over a wide range of doping (x=0.05-0.21). We found that the normal state Nernst signal is large around the optimal doping, in agreement with previous reports. In the highly overdoped films (x=0.19 and 0.21), the Nernst signal is still large, contrary to what is expected for a single hole-band system. A similar behavior is found for the slightly underdoped samples ($0.11 \leq x \leq 0.13$), suggesting that the FS in this regime is not a simple electron-pocket either. For the extremely underdoped x=0.05, the Nernst signal decreases rapidly, and the magnitude indicates a single band system at this doping.

7.4.2 Experiments and results

Electron-doped cuprates are distinct from hole-doped cuprates in having a low H_{c2}, and thus the normal state can be easily accessed for temperature below T_c. As we have shown in the previous section, when the external magnetic field is larger than H_{c2} or temperature higher than T_c, the Nernst signal e_y in PCCO is linear in field. We define the Nernst coefficient ν as the slope of $e_y(B)$, i.e., $\nu \equiv e_y/B$.

Before showing all the normal state Nernst effect data, let us first compare the vortex Nernst signal ($T<T_c$) and the normal state ($T>T_c$) for H=2 T in an underdoped x=0.13 film. As shown in Fig. 7.9, two peaks are prominent in the temperature dependence of the Nernst signal. The lower temperature peak is produced by the vortex motion in the superconducting state, and the higher temperature peak is from the normal state quasi-particles. In strong contrast to the Nernst effect in hole-doped cuprates (see Fig. 7.3) [99], the normal state Nernst signal is much larger and its magnitude is comparable to the vortex Nernst signal. As the field approaches H_{c2}, the vortex Nernst signal decrease quickly, but the normal state increases linearly, as seen in Fig. 7.4. In the following, the normal state Nernst signal is taken at H=9 T which is greater than $H_{c2}(0)$ for all the PCCO films.

Although our focus of interest is the Nernst effect at the doping extremes, we measured the normal state Nernst effect on PCCO films systematically throughout the entire doping range, from the extremely underdoped (x=0.05) to the highly overdoped (x=0.21). Fig. 7.10 shows the temperature dependence of the normal state Nernst signal e_y for all the doped PCCO films. The Nernst signal increases

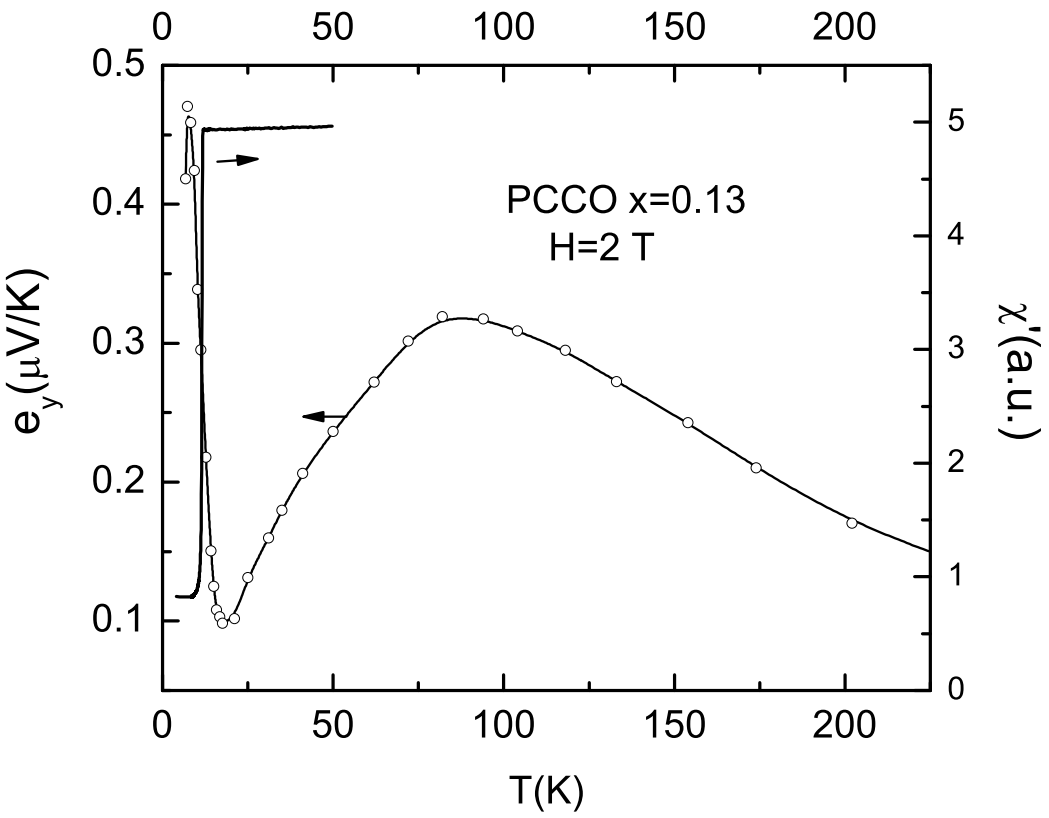

Figure 7.9: Temperature dependence of the Nernst signal in an underdoped PCCO with x=0.13 at H=2 T. The $H_{c2}(0)$ of this film is about 7 T and T_c is 11.5 K. Solid line is the real part of the zero-field AC susceptibility.

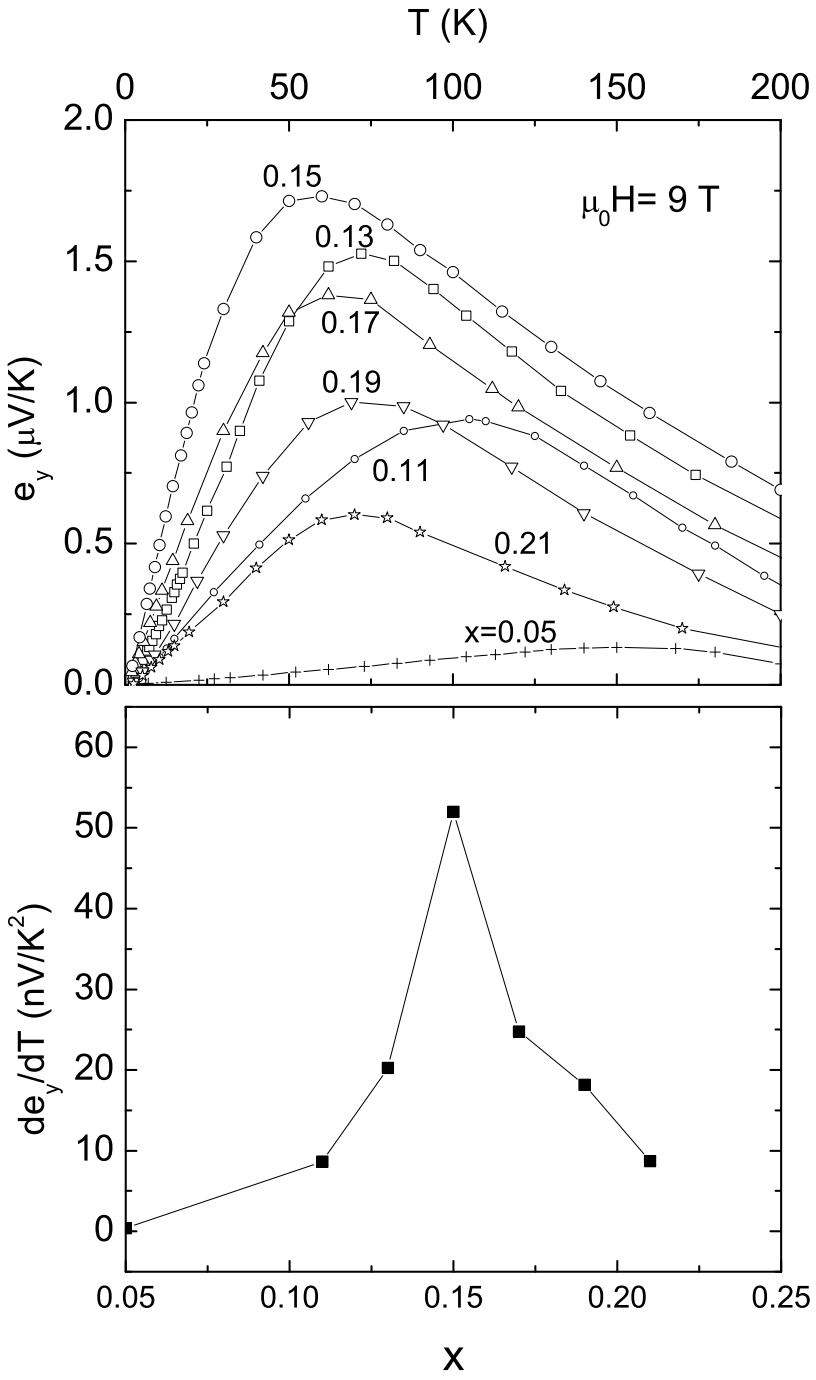

Figure 7.10: (a) Temperature dependence of normal state Nernst signal at μ_0H=9 T for all the doped PCCO films. (b) Doping dependence of the initial slope of the Nernst signal curves in (a) at low temperatures.

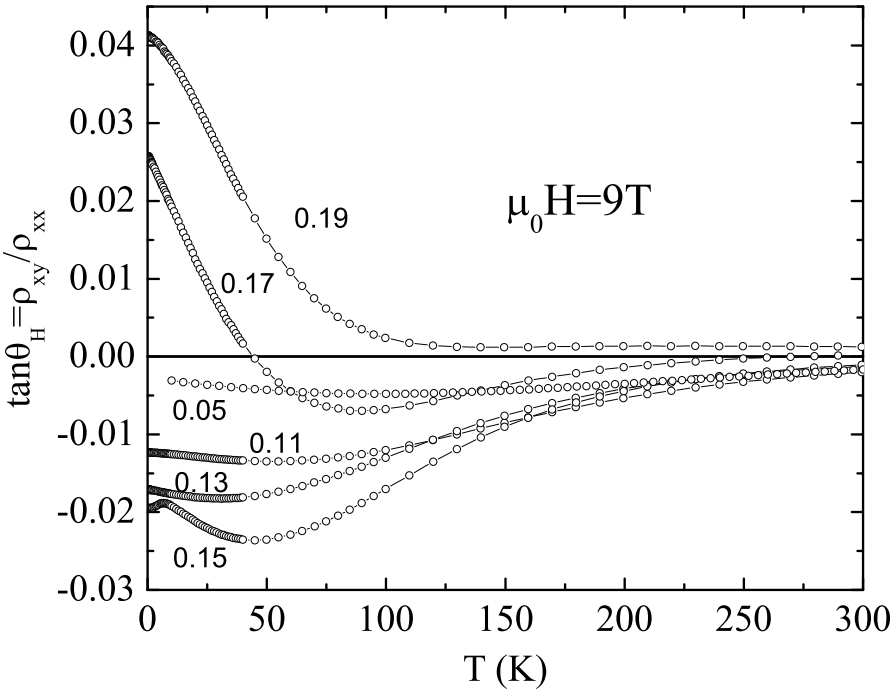

Figure 7.11: Temperature dependence of the Hall angle $tan\theta_H$ of the PCCO films.

as temperature decreases, reaches a peak at a certain temperature then decreases linearly towards zero as T→0. The magnitude of the Nernst signal and its temperature dependence are rather similar for all the dopings except the extremely underdoped x=0.05. The linear temperature dependence of the the Nernst signal below the peak temperatures is as predicted for quasi-particles (see later discussion). In Fig. 7.10(b), the doping dependence of the slope (de_y/dT) of the low temperature Nernst signal is shown. We see that de_y/dT has a maximum at the optimal doping and decreases rapidly with underdoping and overdoping.

For later discussion use, we present the Hall angle, $tan\theta_H = \rho_{xy}/\rho_{xx}$, obtained

from the Hall effect data shown in chapter 1 for all the PCCO films. As shown in Fig. 7.11, the Hall angle reveals a continuous variation from a small negative value (x=0.05) to a large one (x=0.15), and finally an abrupt change of sign to a positive value in the overdoped region. The Hall mobility $\mu_H = tan\theta_H/H$ and $\omega_c\tau = tan\theta_H$ can be directly obtained from the Hall angle data [47].

7.4.3 Discussion

One-band transport

The anomalously large normal state Nernst effect that we observed throughout almost the entire doping range strongly contrasts with the hole-doped cuprates and with normal metals in which the magnitude of the Nernst signal is in the order of nV/K. To understand this, we attempted a simple comparison with conventional theories for a one-band (single-carrier) system. Within Boltzmann theory, the Nernst coefficient can be expressed as (see chapter 2 and Ref. [142]),

$$\nu = \frac{\pi}{3}\frac{k_B^2 T}{eB}\frac{\partial tan\theta_H}{\partial \epsilon} = \frac{\pi^2 k_B^2 T}{3m^*}\frac{\partial \tau}{\partial \epsilon}|_{\epsilon_F} \tag{7.8}$$

where $tan\theta_H$ is the Hall angle and τ the scattering time. Eq. 7.8 shows that the Nernst signal is linearly dependent on the temperature and our low temperature data at all dopings is consistent with this prediction. The high temperature data does not obey the linear dependence and there is no theory that we are aware of which can explain the high temperature behavior, where the Nernst signal seems proportional to the inverse of temperature, i.e., $e_y \propto 1/T$. To estimate the magnitude of the low temperature Nernst signal, we can replace $\frac{\partial \tau}{\partial \epsilon_F}$ with $\frac{\tau}{\epsilon_F}$ by assumption of a weak

energy dependence of τ at the Fermi energy ϵ_F. This gives [80]

$$e_y = \nu B = 283\omega_c\tau\frac{k_BT}{\epsilon_F}\mu V/K \tag{7.9}$$

where $\omega_c = eB/m^*$ is the cyclotron frequency. Eq. 7.9 suggests that the Nernst signal is proportional to $\omega_c\tau$ and inversely proportional to Fermi energy.

For a single carrier system, $\omega_c\tau$ can be estimated from the residual resistivity ρ_0 and the carrier density n, i.e., $\omega_c\tau = B/\rho ne$, which is equivalent to $\omega_c\tau = tan\theta_H$. For the optimally-doped x=0.15, normal state resistivity measurement (Fig. 3.3) gives ρ_0=57 $\mu\Omega cm$. The estimation of the carrier density n is rather unclear. For comparison, we estimate n in two different ways. From the Hall coefficient, one gets $n_{Hall} = \frac{1}{R_H(0)e}$=$4.2 \times 10^{21}/cm^3$ and $\omega_c\tau$=0.022 (see also Fig. 7.11). Another way is by naively assuming 0.15 electron/unit cell, one can get n_{cell}=$\frac{0.15}{3.95^2\times 6}$Å^{-3}=$1.58\times 10^{21}/cm^3$, which yields $\omega_c\tau$=0.059. The Fermi energy ϵ_F can be obtained from ARPES [24], which gives ϵ_F ~0.53 eV and then ϵ_F/k_B=6100 K. Inserting the numbers into the expression for e_y in Eq. 7.9, we find de_y/dT=1.2 nV/K^2 (from n_{Hall}) and 2.1 nV/K^2 (from n_{cell}). These values are more than one order of magnitude smaller than the measured value [53 nV/K^2, Fig 7.10(b)].

Now we apply this simple estimation to the overdoped sample. The numbers for x=0.19 are ρ_0=20 $\mu\Omega cm$, n_{Hall}=$6.5 \times 10^{21}/cm^3$ and n_{cell}=$2.01 \times 10^{21}/cm^3$. $\omega_c\tau$ then is 0.04 and 0.139 respectively. The Fermi energy, due to the lacking of experimental results, can be estimated from the following for free electrons [151]

$$\epsilon_F = (\pi^2k_B^2/3)n/\gamma \tag{7.10}$$

Assume that γ does not change much with doping, then ϵ_F simply depends on n.

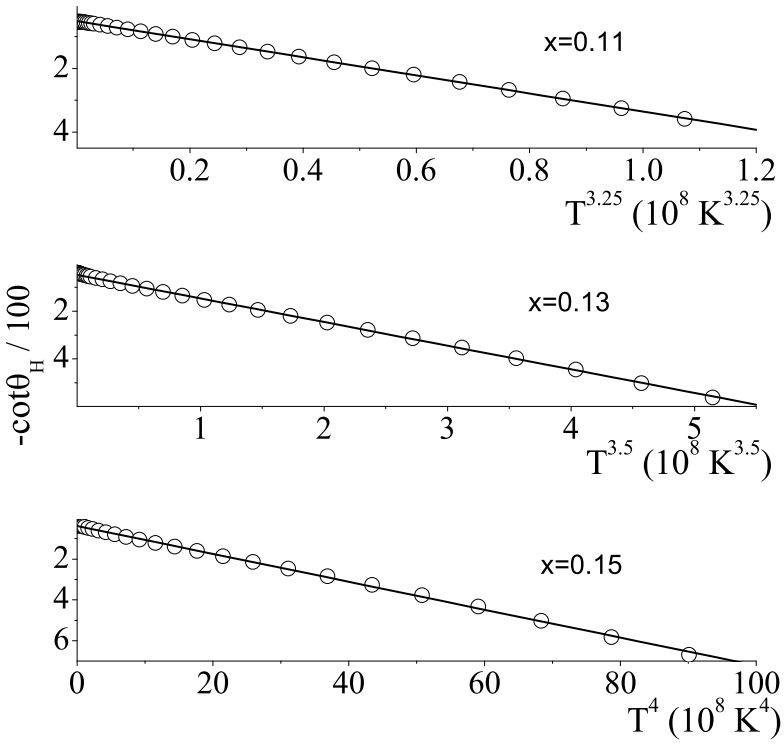

Figure 7.12: Temperature dependence of $cot\theta(T)$ of the underdoped and optimally-doped PCCO films (from Ref. [143]).

Therefore, using the experimental value of ϵ_F for x=0.15, we can estimate that ϵ_F is about 8000 K for x=0.19. Thus, de_y/dT=1.4 nV/K^2 and 5 nV/K^2 for n_{Hall} and n_{cell} respectively. The decrease of the Nernst signal with increased doping is consistent with Eq. 7.9 due to the increase of Fermi energy. However, the estimated values are still much smaller than the measured value of 20 nV/K^2 for x=0.19.

The large difference of the simple estimation with our experiments shows that a conventional one-band model is not applicable to PCCO even in the highly over-doped region, which is expected to be a one-carrier metal with a large hole-like FS.

If we estimate the carrier density from the area of the Fermi pockets obtained from ARPES [53] and the SDW calculation [59], similarly to the procedure we used in chapter 5, we get $n_{FS} = 4.32 \times 10^{21}/cm^3$. This yields $de_y/dT \sim 2$ nV/K^2, which is also one order of magnitude smaller than the experiments. This shows that the overdoped PCCO is not a simple one-carrier metal describable by the Drude model. It suggests that correlation effects must play a role, even at a doping far from the Mott state..

The failure of the single-carrier Boltzmann transport in explaining the Nernst signal in PCCO is not surprising since it is also known to be unable to explain the temperature dependence of the Hall coefficient [144]. Anderson proposed a model with two relaxation times [145], a possible result of spin-charge separation, to explain the observed $cot\theta_H(T) \propto T^2$ in hole-doped cuprates. In this model, the resistivity is only sensitive to the relaxation of momentum normal to the Fermi surface (holon-spinon scattering), resulting in a relaxation time $\tau_{tr} \propto T^{-1}$ ($\sigma_{xx} \propto \tau_{tr}$). In the presence of a magnetic field, a second component influenced by spinon-spinon scattering (relaxation of momentum tangent to the Fermi surface) is involved, giving $\tau_H \propto T^2$ ($\sigma_{xy} \propto \tau_{tr}\tau_H$). This will lead to a Hall angle $\theta_H \equiv \omega_c\tau_H \propto T^{-2}$, which is consistent with results in optimally-doped p-type cuprates. However, in the electron-doped PCCO (Fig. 7.12), we actually find that the inverse of Hall angle $cot\theta_H$ in the underdoped region is proportional to T^α (100 K<T<300 K), α increases from 3.34 for x=0.11 to 4 for 0.15. This certainly contradicts the spin-charge separation model. Abrahams and Varma proposed a model which could explain this. In this model, the α is twice as the resistivity component, which is about 2 in PCCO.

For the overdoped films, due to the sign change of Hall angle in the intermediate temperature range, we can only analyze the low temperature data for T<10 K. Interestingly, $cot\theta_H$ and resistivity follow the same temperature dependence, i.e., α=2. This suggests that the same regions on the Fermi surface contributes to both Hall effect and resistivity. These overdoped results are in contradiction with the theory of Abrahams and Varma [146] of small angle impurity scattering.

A single-band model with an anisotropic mean-free path (MFP) was also proposed to explain the anomalous Hall effect in cuprates [147, 148]. The two characteristic MFPs (l_f and l_c) are different along the Fermi surface (f on the flat parts and c on the curved parts). This model predicts $\sigma_{xx} \propto l_f$ and $\sigma_{xy} \propto l_f l_c$, and thus, the Hall angle is proportional to l_c alone. With the appropriate temperature dependence, it is possible to interpret the Hall angle of the hole-doped cuprates. However, for the electron-doped cuprates, it is known that the resistivity is quadratic in temperature, i.e., $l_f \propto 1/T^2$ and the Hall angle suggests that l_c should follow $l_c \propto 1/T^4$. This temperature dependence of the MFP is quite unusual and the scattering mechanism is still not understood. Moreover, this model is unable to explain the sign change in the temperature dependence of Hall coefficient in the overdoped PCCO samples.

Two-band transport

The sign change and the temperature dependence of both Hall coefficient and thermopower, the anomalously large Nernst signal and magnetoresistance (to be

shown next) can not be explained by a one-band model. Therefore, one has to consider a two-carrier transport model for the electron-doped cuprates.

Again, we start with an estimation of the Nernst signal within a two-band (ambipolar) Boltzmann framework [142]. In this model, assuming an identical relaxation for both electron and hole carriers, we have

$$\sigma_{xx} = (n_h + n_e)\frac{e^2\tau}{m}, \quad \sigma_{xy} = (n_h - n_e)\frac{e^2\tau}{m}\omega_c\tau \tag{7.11}$$

leading to a Nernst coefficient

$$\nu = \frac{2\pi^2 k_B^2 T}{3eB}\frac{n_e n_h}{(n_e + n_h)^2}(\frac{1}{\epsilon_F^e} + \frac{1}{\epsilon_F^h})\omega_c\tau \tag{7.12}$$

The Nernst signal is maximal when the bands are exactly compensated ($n_h = n_e$). Substituting $n_e = n_h = k_F^2/4\pi$ for a 2D Fermi surface and $\epsilon_F^h = \epsilon_F^e = \frac{\hbar k_F^2}{2m}$, we can rewrite Eq. 7.12 as

$$e_y = B\nu = \frac{2\pi^2}{3}\frac{k_B^2 T\tau}{e\hbar}\frac{1}{(k_F\ell_B)^2} \tag{7.13}$$

where k_F is the Fermi wave number and $\ell_B^2{=}\hbar/eB$ the magnetic length. Inserting $k_F \sim 0.4$ Å^{-1} obtained from ARPES experiments ($v_F = 4.3 \times 10^5 m/s$ and $k_F = 0.6\pi/a \sim \frac{mv_F}{\hbar}$, m the bare electron mass) [50, 25] and $\tau \sim 4.3 \times 10^{-13}$ s from optics ($1/\tau = 80$ cm^{-1} for T just above T$_c$) [107, 112] for PCCO x=0.15, we get de_y/dT ~33 nV/K^2 for μ_0H=9 T. This simple estimation is slightly smaller than the measured value of 53 $\mu V/K^2$, but suggests that this two-band Boltzmann model could explain the Nernst effect in PCCO.

Now we turn to a qualitative two-band Drude model for the transport properties of PCCO. We start with the Hall effect and thermopower. In a two-carrier

system, the Hall coefficient and thermopower can be expressed as [47]

$$R_H = \frac{R_h\sigma_h^2 + R_e\sigma_e^2}{\sigma^2} \tag{7.14}$$

$$S = \frac{S_h\sigma_h + S_e\sigma_e}{\sigma^2} \tag{7.15}$$

$$\sigma = \sigma_h + \sigma_e \tag{7.16}$$

where $S_h(S_e)$ is the thermopower of holes (electrons). Eq. 7.15 can be shown to be equivalent to Eq. 2.65. It is then clear that a temperature-dependent Hall coefficient and thermopower could arise if two types of charge carriers with different signs and different temperature dependences for their relaxation times are present. Assuming that a continuous decrease of σ_e/σ_h accompanies the doping because n_e decreases and n_h increases, then both R_H and S can be driven from a negative value, when $\sigma_e \gg \sigma_h$, to a positive one, when $\sigma_e \ll \sigma_h$. The low temperature R_H moving towards a positive value for $x \geq 0.15$ in PCCO strongly suggests the emergence of the hole-like contribution.

Qualitatively, the Nernst coefficient for a two-band system can be derived from Eq. 2.66[46, 47, 67],

$$\nu = \frac{\nu_h\sigma_h + \nu_e\sigma_e}{\sigma} + \frac{\sigma_h\sigma_e(S_h - S_e)(\sigma_h R_h - \sigma_e R_e)}{\sigma^2} \tag{7.17}$$

The first term in this equation looks like thermopower in Eq. 7.15, and it can smoothly evolve from ν_e to ν_h as σ_e/σ_h decreases. However, the sign of ν will not change since $\nu_{e(h)} = \alpha_{xy}/\sigma_{xx}$ and α_{xy} has the same sign for both electrons and holes. This term is small if one band is dominant. The second term, however, can be responsible for the potentially larger Nernst signal with respect to a single carrier

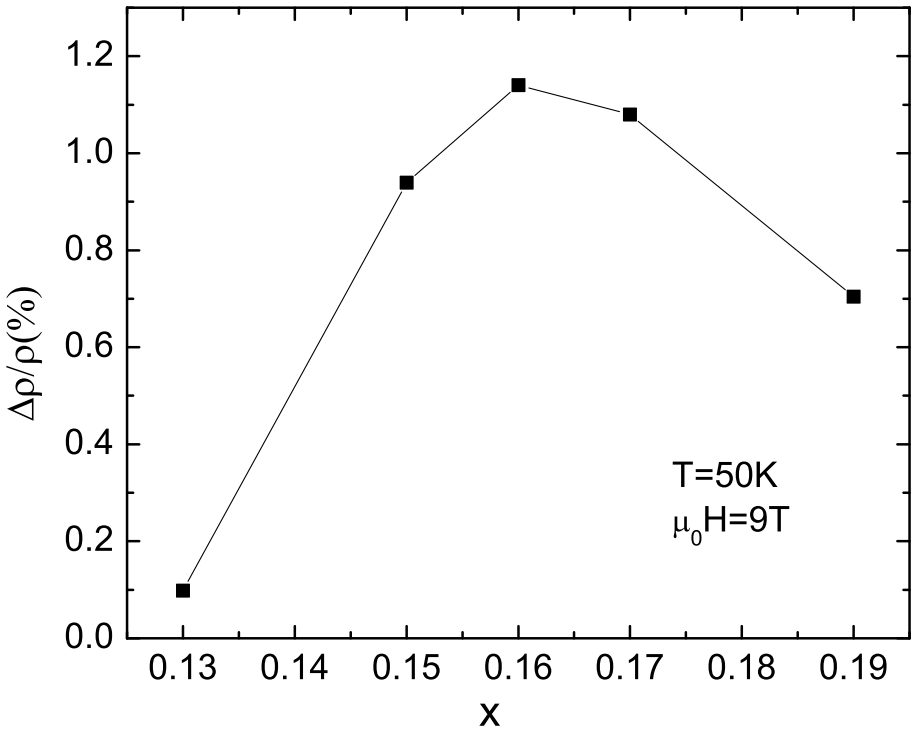

Figure 7.13: Doping dependence of the normal state magnetoresistance in PCCO films at T=50 K (T is set at 50 K in order to avoid the low temperature superconducting fluctuations).

system. The factor $(\sigma_h R_h - \sigma_e R_e) = (\mu_h - \mu_e)$ can reach a maximum value if the mobilities are large and $\mu_h = -\mu_e$, which will lead to an enhanced Nernst signal.

The magnetoresistance in a two-carrier system is closely related to the Nernst effect, as seen from the expression for magnetoresistance in a two-band model,

$$\frac{\triangle\rho}{\rho} = \frac{\sigma_h \sigma_e (\sigma_h R_h - \sigma_e R_e)^2 B^2}{\sigma^2} \tag{7.18}$$

We can identify the same mobility coefficient, $(\sigma_h R_h - \sigma_e R_e)$, found in the Nernst

coefficient in the second term of Eq. 7.17. This indicates that a maximum of the magnetoresistance is likely to coincide with a maximum of the Nernst coefficient as the doping and the mobilities. We note that this argument has been used previously for explaining the Nernst effect in oxygen-doped NCCO [46, 47]. In Fig. 7.13, we show the magnetoresistance at 50 K as a function of Ce content. We see that the transverse magnetoresistance is large and positive (compared to the magnetoresistance in the p-doped cuprates, which is one order of magnitude smaller) for all the superconducting films. The maximum magnetoresistance occurs around optimal doping, at which doping, the Nernst signal [Fig. 7.10(b)] also reach a maximum. The strong correlation between Nernst effect and the magnetoresistance strongly suggests that PCCO is a two-band system for dopings in the superconducting dome region of the phase diagram.

The enhanced Nernst effect in a two-band system can also be easily understood from the alternative expressions for the Nernst signal and thermopower that we introduced in chapter 2 (and Ref. [67]),

$$e_y = S\left(\frac{\alpha^h_{xy}+\alpha^e_{xy}}{\alpha^h_{xx}+\alpha^e_{xx}} - \frac{\sigma^h_{xy}+\sigma^e_{xy}}{\sigma^h_{xx}+\sigma^e_{xx}}\right) \tag{7.19}$$

$$= S(tan\theta_T - tan\theta_H) \tag{7.20}$$

and

$$S = \frac{\alpha^h_{xx}+\alpha^e_{xx}}{\sigma^h_{xx}+\sigma^e_{xx}} \tag{7.21}$$

These two expressions are equivalent to Eq. 7.17 (with $e_y = \mu B$) and 7.15. Considering the charge carrier symmetry, $\sigma^h_{xy} = -\sigma^e_{xy}$ and $\alpha^h_{xy} = \alpha^e_{xy}$, the second term in Eq. 7.19 will vanish, but the first term will be significantly enhanced. Meanwhile,

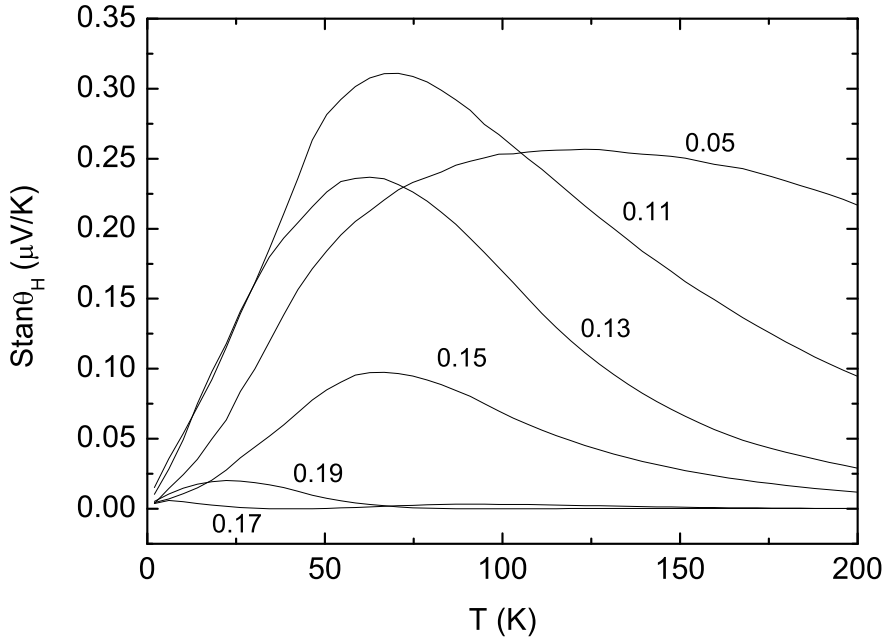

Figure 7.14: Temperature dependence of $Stan\theta_H$ of PCCO films.

the counterflow of carriers with different sign in Eq. 7.21, i.e., $\alpha^h_{xx} = -\alpha^e_{xx}$, will lead to a small thermpower. Thus, in PCCO, the enhanced Nernst signal and small thermopower (see Fig 4.2 and Fig 4.3) around the optimally-doping supports the two-band model. For the underdoped x=0.13 and 0.11, although a larger thermopower is found, the Nernst signal is still large, which could be due to a contribution from the emerging hole band, as found in the traces of hole-pocket in ARPES [50, 53].

The small thermopower (Fig 4.2 and Fig 4.3) and sizable Nernst signal (comparable to the optimal doping) in the highly overdoped x=0.19 (and 0.21), also suggest a possible two-band contribution. This appears incompatible with the single large hole pocket seen in ARPES [53]. To explore this further, we look at $Stan\theta_H$ obtained

from the thermopower data presented in chapter 4 and the Hall angle data we have just shown, for all the doped PCCO films. As seen in Fig. 7.14, $Stan\theta_H$ decreases with increasing doping and its magnitude is much smaller than the Nernst signal in Fig. 7.10 for all the dopings except the extremely underdoped x=0.05. As we just described (also in chapter 2), to have a large Nernst signal, the difference between $Stan\theta_H$ (the second term in Eq. 7.21) and $Stan\theta_T$ (the first term in Eq. 7.21) has to be large. In PCCO, the large discrepancy between e_y and $Stan\theta_H$ (see Fig. 7.10 and Fig. 7.14) suggests a large thermal Hall angle (recall that S is small), i.e., a large value of $\frac{\alpha^h_{xy}+\alpha^e_{xy}}{\alpha}$. For a single carrier system, such as the extremely underdoped x=0.05 PCCO, the small Nernst signal is comparable to $Stan\theta_H$, suggests a negligible $Stan\theta_T$ (see Eq. 2.37). Therefore, the large value of $Stan\theta_T$ indicates a two-carrier contribution. This is also seen in the overdoped PCCO from Fig. 7.10 and Fig. 7.14, strongly suggesting the incompatibility with the single hole-like FS expectation. We note that two-band transport in the highly overdoped PCCO is also consistent with the high-field nonlinear Hall resistivity, as we presented in chapter 5.

Similar to the Hall coefficient case, the strong temperature dependence of both thermopower and Nernst effect in PCCO is also not understood. The peak feature that found in thermopower and Nernst effect measurements suggests a common origin. A prior work [149] proposed that the thermoelectric power of the underdoped hole-doped cuprates could reveal the opening of a pseudogap. The pseudogap increases the thermopower leading to a broad maximum above T_c but below T^*. For the PCCO system, we also observed a maximum thermopower at fairly high tem-

perature (between 50 K and 100 K) in the underdoped region. It is possible that the thermopower is influenced by the high temperature gap found in the optics [57] and ARPES measurements [53]. It is also possible that the SDW gap in the underdoped region and the strong spin fluctuations (gap-like) in the overdoped region at high temperature affect the thermoelectric effect. The Nernst effect, the transverse component of themopower in magnetic field, also presents a broad higher temperature peak in the entire doping range. The peak feature could also be a result of the influence of high energy gap or gap fluctuations in the overdoped region. Further understanding of this will require future study.

The peak feature in the temperature dependence of the Nernst signal could also be a result of a phonon-drag effect. As proposed by Behnia *et al.* [150] for Bismuth, in the Ettingshausen geometry (transverse temperature gradient generated by external magnetic field when a longitudinal electrical current is present) , when electrons loose their impulsion on a collision with phonons, the electric current gives rise to an entropy current of phononic origin, hence a significant Ettingshausen effect [61]. Since the Onsager relation ties the amplitudes of the Ettingshausen and Nernst effects, this implies that the Nernst effect should also be enhanced. However, the application of this model to the PCCO case is not clear at this time and future study will be necessary.

7.4.4 Conclusion

To summarize this section, we performed measurements of the magnetic field driven normal state Nernst effect on electron-doped cuprate $Pr_{2-x}Ce_xCuO_{4-\delta}$ films over a wide range of doping and temperature. We find an anomalously large Nernst signal near optimal doping, which is consistent with prior reports. More interestingly, the Nernst signal is still large in the highly overdoped films and the slightly underdoped films. This can not be explained by a single-band model, and a two-band model has to be considered. The qualitative consistence between the experimental data and the two-band model for the overdoped films suggests that either the FS is not a simple hole-like pocket, which is not compatible to the photoemission experiments, or correlation effects have an unknown influence on the scattering which leads to an enhanced Nernst effect. Further study is needed to understand this discrepancy.

Chapter 8

Nernst Effect in $Y_{1-x}Pr_xBa_2Cu_3O_7$ films

8.1 Introduction

The anomalously large Nernst voltage well above the zero-field T_c in hole-doped cuprate superconductors is now a well established experimental observation with a dominant view that it is due to vortex-like excitations in the phase uncorrelated superfluid above T_c [99, 125]. Such excitations nucleate in the presence of an external field due to a non-zero pairing amplitude of incoherent phase at $T>T_c$ and drift down the thermal gradient generating a transverse voltage. The appearance of the Nernst signal on approaching T_c from above, therefore, marks the onset of a phase uncorrelated pairing amplitude. The observation of an enhanced diamagnetism near the onset temperature T_ν of the anomalous Nernst signal in some hole-doped cuprates strongly supports the vortex-like excitations scenario [152] The fact that the regime of this large Nernst effect overlaps with the temperature range where a pseudogap is seen in the electronic excitation spectrum, somehow also suggests that the anomalous Nernst effect may be related to the pseudogap phenomenon, although counterviews also exist on the prescription of vortex-like excitations and correlation between Nernst effect and pseudogap phenomenon [127, 133]. Rullier-Albenque *et al.* [153] have established a correlation between the width of the phase fluctuation regime over which a large Nernst voltage is seen and disorder in the

CuO_2 planes induced by electron irradiation. The disordered samples show a wider range of phase fluctuations. However, high T_c cuprates can also be subjected to out-of-plane disorder by changing the ionic radius of the rare earth and alkaline earth sites while keeping the hole concentration fixed. The disorder works as a weak scatterer and reduces T_c substantially [154].

The cuprate $Y_{1-x}Pr_xBa_2Cu_3O_{7-\delta}$ (Pr-YBCO) presents a very interesting system to study the role of out-of-plane disorder on the regime of incoherent phase fluctuations in $YBa_2Cu_3O_{7-\delta}$ cuprates because the ionic radius of Pr^{3+} is larger by a factor of about 1.134 compared to the ionic radius of Y^{3+}. In this chapter, we present the first measurements of the normal state Nernst Effect in $Y_{1-x}Pr_xBa_2Cu_3O_{7-\delta}$ over a broad range of composition. These data have been augmented by measurements of Hall angle and in-plane resistivity over a wide range of field and temperature. We note that while the zero-field superconducting transition temperature T_c drops with increasing Pr in a quasi non-linear manner as reported earlier [155], the fluctuation regime $\triangle T_{fl}=(T_\nu\text{-}T_c)$ widens. Most remarkably, an interesting correlation emerges between T_ν and T_c in the YBCO family of cuprates with in-plane and out-of-plane disorder.

8.2 Experiments and results

The c-axis oriented epitaxial $Y_{1-x}Pr_xBa_2Cu_3O_{7-\delta}$ (x=0, 0.1, 0.2, 0.3, 0.4) films of thickness about 2500 Å were fabricated on (100) $SrTiO_3$ substrates by pulsed laser deposition using a KrF excimer laser (λ=248 nm) with a typical repetition rate and

energy density of 5 Hz and 2 J/cm^2 respectively, which yields a growth rate of 1.6 Å/second. The deposition temperature and oxygen partial pressure during film deposition were set 800 ^0C and about 400 mTorr respectively.

The in-plane resistivity and Hall effect measurements were done on the films patterned to a standard Hall bar in a Quantum Design PPMS with a 14 T magnet. The Nernst measurements were performed using a one-heater-two-thermometer technique as we described in chapter 3. The film was attached on one end to a copper block with a mechanical clamp and the other end was left free. A small chip resistor heater is attached on the free end, and a temperature gradient is created by applying a constant current to the heater. Two tiny Lakeshore Cernox thermometers are attached on the two ends of the sample to monitor the temperature gradient continuously. The Nernst voltage is measured with a Keithley 2001 multimeter with a 1801 preamp while the field is slowly ramped at a rate of 0.3 T/min between -14 T and +14 T ($H \perp ab$). The system temperature was well controlled to give stability of the temperature of $\pm$1 mK, which enables us to perform a high resolution Nernst voltage measurement (typically $\sim$10 nV in our setup). The temperature gradient is around 0.5-2 K/cm depending on the temperature of measurement, and the sample temperature is taken as the average of hot and cold end temperatures. The Nernst signal is obtained by subtracting negative field data from positive field data to eliminate any possible thermopower contribution.

Fig. 8.1 shows the temperature dependence of the in-plane resistivity ρ_{ab} for $Y_{1-x}Pr_xBa_2Cu_3O_{7-\delta}$ films with Pr concentration from 0 to 0.4. The zero field superconducting transition temperature T_c decreases from 90 K for the x=0 film to

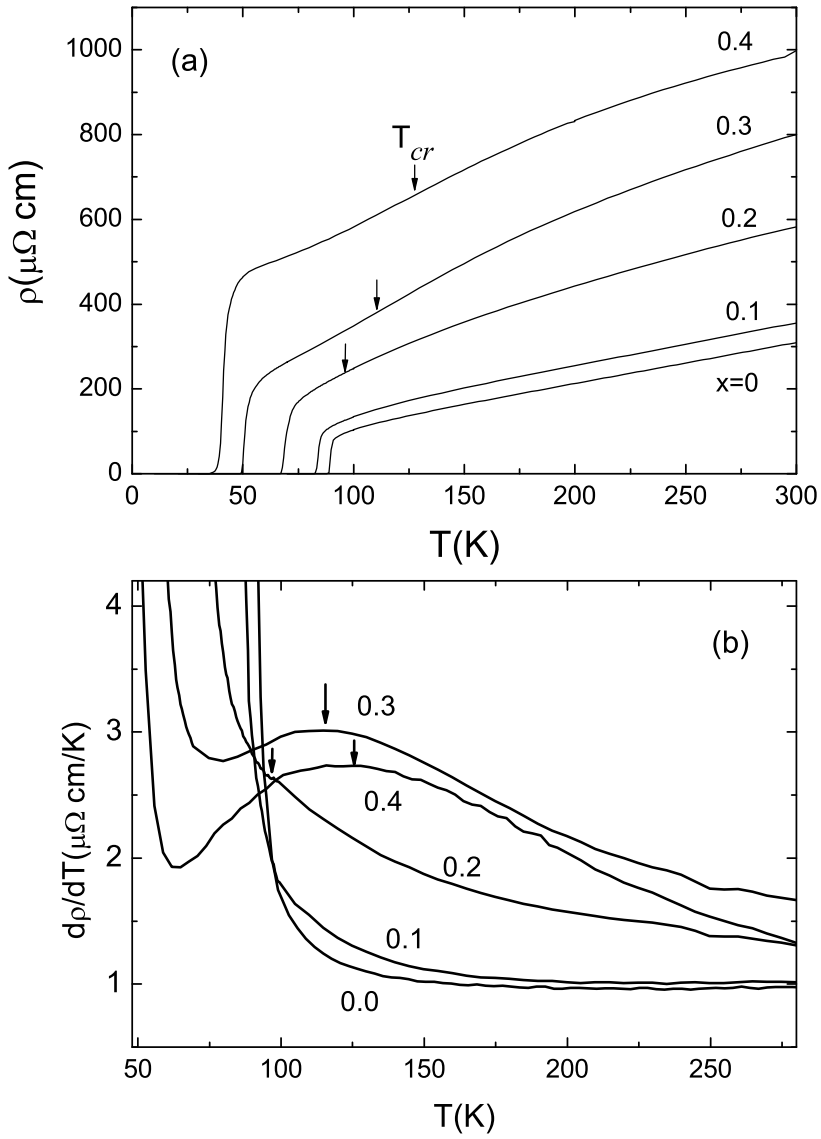

Figure 8.1: (a) In-plan resistivity as a function of temperature for the $Y_{1-x}Pr_xBa_2Cu_3O_{7-\delta}$ films (x from 0 to 0.4). (b) shows the temperature derivative of the resistivity from the main panel for all the films. The arrows indicate the temperature where the peak of the derivative plot appears.

about 40 K for the underdoped x=0.4 film in agreement with published work on these cuprates [156, 157, 158]. The in-plane resistivity increases with Pr content, which suggests a decrease of carrier concentration or carrier mobility due to out-of-plane disorder caused by Pr. While the resistivity $\rho_{ab}(T)$ remains metallic in the normal state, a small upturn in $\rho_{ab}(T)$ on cooling is seen in the x=0.4 film just above T_c, which may be due to charge localizations found in many other cuprates. The resistivity has a linear temperature dependence for the fully oxygenated Pr-free film, while it deviates from linearity on increasing the Pr doping. The temperature below which this deviation from linearity sets in is about 190 K in the x=0.1 film and gradually exceeds 300 K for the film with the highest Pr concentration. This non-linear ρ_{ab} below 300 K for the higher Pr-rich samples indicates a pseudogap regime above T_c. This deviation of ρ_{ab}(T) from linearity on cooling is not monotonic. To illustrate this point we show in the inset of Fig. 8.1 the temperature derivative $d\rho_{ab}(T)/dT$ of all the films. The $d\rho_{ab}(T)/dT$ vs T plot of the films with $x \geq 0.2$ goes through a maximum and the peak temperature shifts towards higher values with the increasing Pr content. This observation is consistent with the resistivity data of $Y_{1-x}Pr_xBa_2Cu_3O_{7-\delta}$ single crystals [155]. We note that the peak temperature T_{cr} is much lower than the pseudogap temperature, as found from the deviation of the linear resistivity. Sandu *et al.* [155] have identified this critical temperature T_{cr} in the ρ_{ab}(T) data of their $Y_{1-x}Pr_xBa_2Cu_3O_{7-\delta}$ single crystals as a signature of the onset of dissipation due to thermally excited vortex loops. We will shortly compare T_{cr} with the onset temperature T_ν of the anomalous Nernst voltage, which is a direct indicator of vortex loop excitations. At this juncture, it is also worth-

while to point out that the overall behavior of the $\rho(T)$ of these films is similar to that observed by Convington and Greene [159] in their $Y_{1-x}Pr_xBa_2Cu_3O_{7-\delta}$ films. The important consequence of Pr doping is a significant enhancement in resistivity without affecting the linear temperature dependence of ρ at T$\geq$120 K. This points towards enhanced scattering within CuO_2 planes without affecting the carrier concentration as seen in Zn doped YBCO. At larger Pr concentrations ($x\geq$0.5), the $\rho(T)$ curves develop an S shape similar to that seen in oxygen deficient YBCO in the vicinity of superconducting transition. This is a signature of reduction in carrier concentration.

Temperature dependence of the Hall effect for all the films was measured in a 14 T field and the result is consistent with prior work (see Ref. [156, 157]). The normal state Hall coefficient R_H first increases as the temperature is lowered from 300 K and then drops near the superconducting transition. At a given temperature, the Hall number decreases with Pr doping. It is about 4 times smaller at T=300 K in the x=0.4 film than for the Pr-free sample suggesting a strong localization of mobile holes by the local field of the Pr ions. The temperature dependence of the Hall angle $cot\theta_H(T)$ for all the films was calculated. We find that the $cot\theta_H(T)$ data can be fitted to the form $cot\theta_H = a + bT^n$ with n close to 2. A similar temperature dependence of $cot\theta_H(T)$ in Pr-YBCO samples has been observed in previous reports [156, 157, 158]. A deviation from the power law dependence of $cot\theta_H(T)$ on temperature is seen near T_c in all films. It has been suggested that this deviation could be related to the opening of the pseudogap [160]. To find the temperature T_H where this deviation starts, we plot $(cot\theta_H - a)/bT^n$ as a function

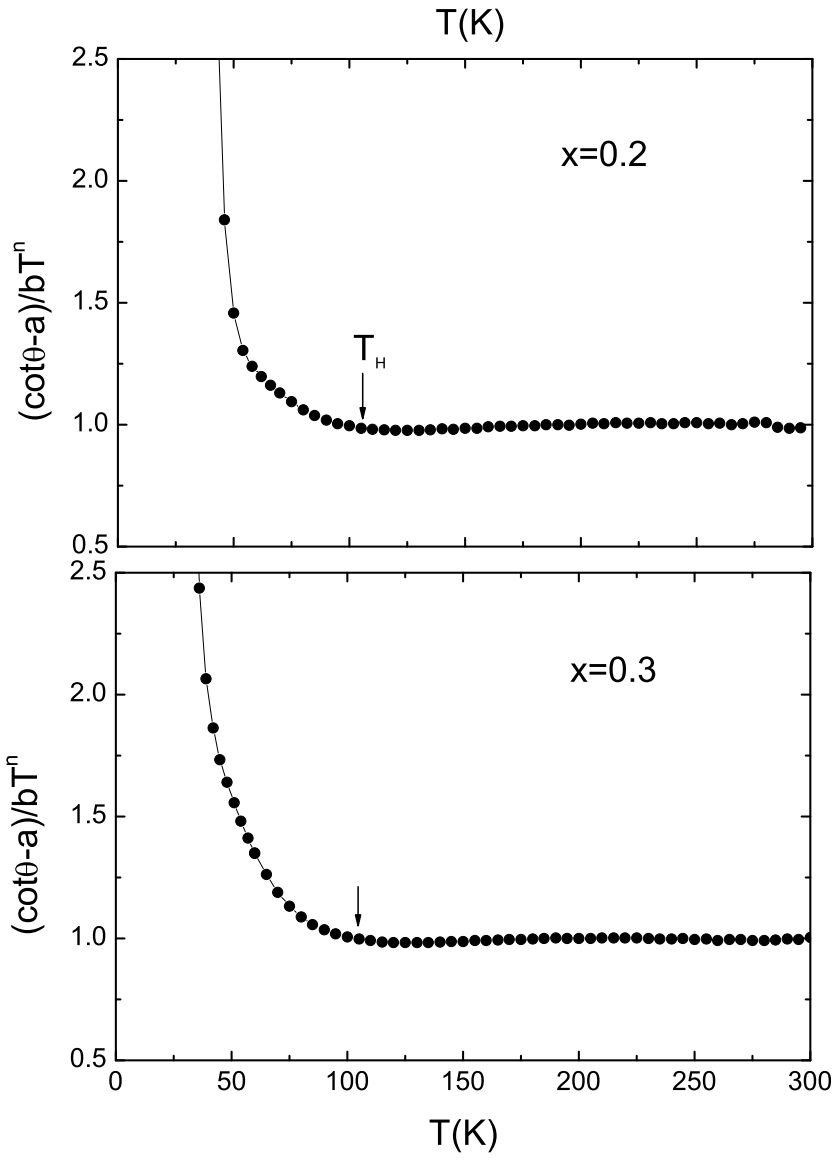

Figure 8.2: $(cot\theta_H - a)/bT^n$ (see text for details) versus temperature for x=0.2 and 0.3 films. The arrows mark the temperature T_H at which the deviation from the high temperature behavior starts.

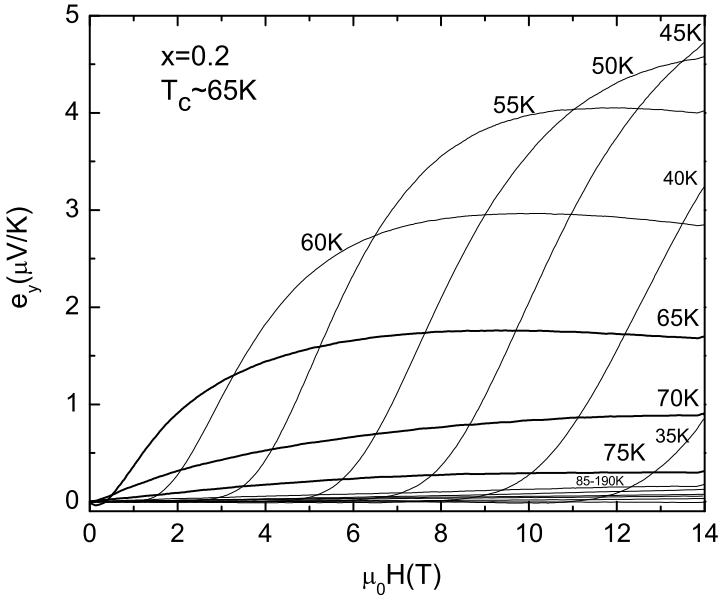

Figure 8.3: The field dependence of the Nernst signal for a $Y_{1-x}Pr_xBa_2Cu_3O_{7-\delta}$ film with x=0.2 at different temperatures.

of temperature for the films (Fig. 8.2) with x=0.2 and 0.3. As seen in the figure, $(cot\theta_H - a)/bT^n$ is a constant of order unity when the temperature is much higher than T_c. It starts to increase sharply below a critical temperature T_H ~105 K for these two Pr content films. We actually find that T_H remains nearly independent of the Pr concentration. Since T_H, which is close to T_{cr} found from the resistivity, is much lower than the pseudogap temperature, it has also been argued [161] that the T_H scale may be related to the onset of superconducting fluctuations or vortex-like excitations in the normal state.

The Nernst effect was measured in all Pr-substituted films. Fig. 8.3 shows the field dependence of the Nernst signal (e_y) at different temperatures for x=0.2 film. A

qualitatively similar field dependence of e_y was observed for the other concentrations of Pr. These data are not shown in Fig. 8.3 for the sake of clarity. The rapid rise of the Nernst signal for field less than the upper critical field (H_{c2}) observed for $T<T_c$ is due to the motion of vortices driven by the temperature gradient. At higher temperatures ($T>T_c$), the Nernst signal remains sizable and has a non-linear field dependence. On increasing the temperature well beyond T_c, the signal e_y becomes extremely small. Here it tends to a negative linear field dependence, which typically is attributed to quasiparticles in the normal state [99].

The temperature dependence of the Nernst signal taken at 14 T for all the films is shown in Fig. 8.4. As seen in the figure, this signal is extremely small for all the films in the high temperature range well above T_c. On decreasing the temperature, the Nernst signal starts to increase rapidly at a certain temperature T_ν, which depends on the Pr concentration. The temperature (T_ν) below which the Nernst signal rises rapidly above the high temperature normal state data is marked by arrows in Fig. 8.4.

8.3 Discussion

The large Nernst signal observed in the temperature window of T_c and T_ν has been interpreted as evidence for vortex-like excitations or strong superconducting fluctuation in most of the hole-doped cuprates [99]. In Fig. 8.5, we show the characteristic temperatures T_{cr}, T_H and T_ν deduced from the measurements of resistivity, Hall angle and Nernst effect respectively along with the zero-field transition tem-

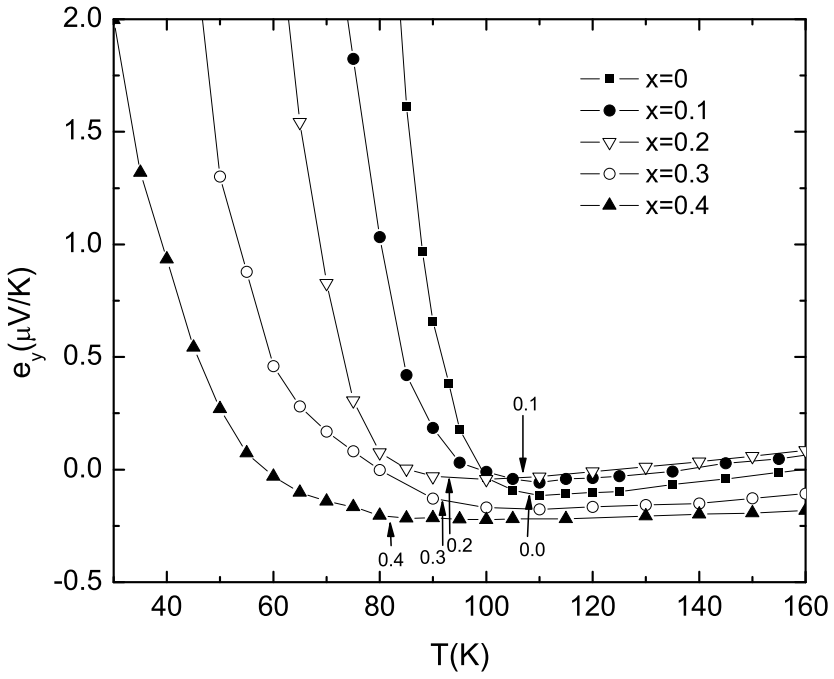

Figure 8.4: The temperature dependence of the Nernst signal taken at 14 T for the $Y_{1-x}Pr_xBa_2Cu_3O_{7-\delta}$ films. The arrows show the temperatures at which the Nernst signal deviates from the high temperature background.

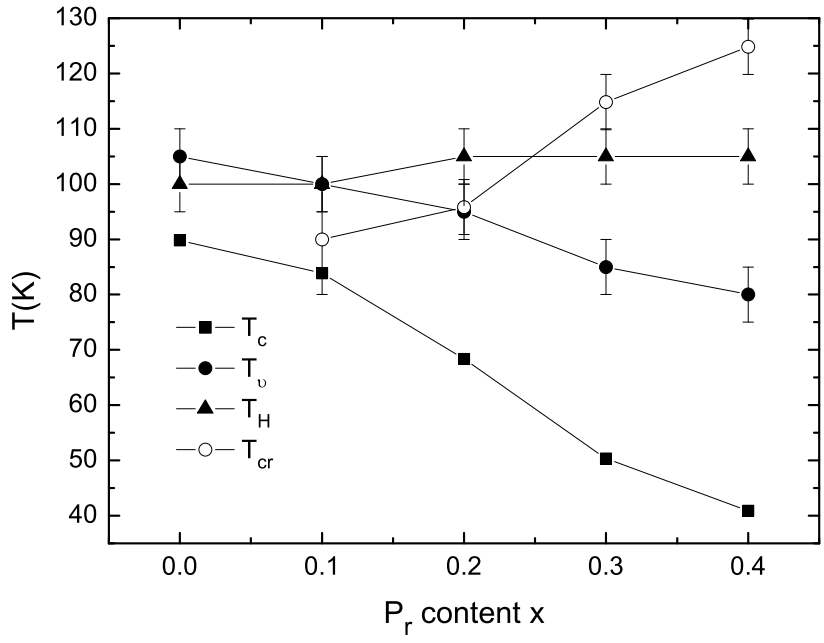

Figure 8.5: Doping dependence of the temperature scales in $Y_{1-x}Pr_xBa_2Cu_3O_{7-\delta}$ films deduced from the temperature derivative of the in-plane resistivity (T_{cr}, open circle), Hall angle (T_H, solid triangle) and Nernst effect measurements (T_ν, filled circle), solid square is the superconducting transition T_c.

perature T_c as a function of Pr concentration. We note that the onset temperature of the anomalous Nernst signal T_ν is lower than T_H and T_{cr}, and the difference between them increases in Pr-rich samples. It as found [152] that in hole-doped cuprates, the onset temperature of the anomalous Nernst signal compares well with the temperature at which a fluctuating diamagnetism appears, it is clear that T_ν is a true indicator of the emergence of vortex like excitations in a phase incoherent condensate. We note that while the T_c drops with increasing Pr, the width of the fluctuation regime $\triangle T_{fl}(=T_\nu\text{-}T_c)$ actually broadens.

The observed increase in $\triangle T_{fl}$ can be associated primarily with the out-of-plane disorder caused by the substitution of Pr at the Y sites of $YBa_2Cu_3O_7$. This site disorder may also have a spin component as the moment on the Pr sites can lead to pair breaking effects. Rullier-Albenque *et al.* [153] have studied the effects of in-plane disorder on the Nernst effect in $YBa_2Cu_3O_7$ and $YBa_2Cu_3O_{6.6}$. They note that the fluctuation regime above T_c expands considerably with the disorder. In Fig. 8.6 we plot the T_ν vs T_c data of our films along with the results of Rullier-Albenque and coworkers. Quite remarkably, these data fall on a single curve with a slope $dT_\nu/dT_c \sim 0.36$. The figure also shows the characteristic temperature T_ν for Zn-doped YBCO [162]. It is known that zinc causes a strong in-plane disorder with a drastic suppression of T_c. The normalized temperature T_ν of the zinc doped YBCO also follows the general trend seen in Fig. 8.6. A simple extrapolation of the curve shown in Fig. 8.6 suggests that a disorder-free $YBa_2Cu_3O_7$ should have a T_c of 110K. In Fig. 8.6 we have also plotted the T_ν of the pristine oxygen-deficient $YBa_2Cu_3O_{7-\delta}$ crystals [139]. Although these samples do not have any deliberately

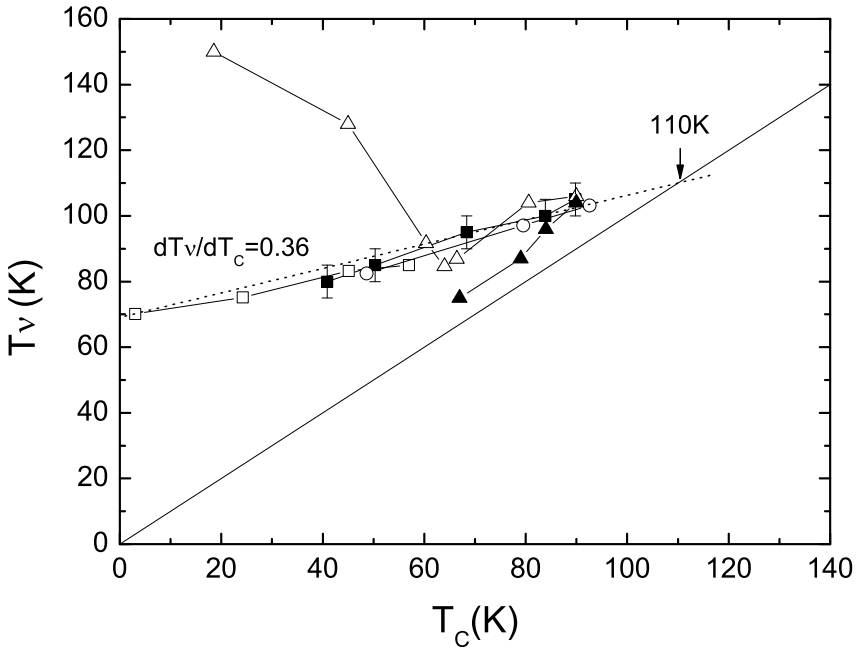

Figure 8.6: Onset temperature T_ν of the anomalous Nernst signal versus T_c for the oxygen-doped and disordered YBCO. Solid square: Pr-YBCO, open triangle: oxygen-doped YBCO (Ref. [139]), open square: $YBa_2Cu_3O_{6.6}$ with electron irradiation (Ref. [153]), open circle: $YBa_2Cu_3O_7$ with electron irradiation (Ref. [153]) and solid triangle: Zn-YBCO (Ref. [162]).

created in-plane or out-of-plane disorder there is some randomness in the occupancy of the plane site oxygen due to a non-zero δ. This positional disorder of oxygen should create local fluctuations in the potential seen by holes. Moreover, the hole concentration of these samples decreased with δ. The T_ν vs T_c curve for these samples shows a large deviation from the data for the disordered samples when the oxygen concentration falls below 6.6 per unit cell of YBCO. From these data it is clear that at least below optimal doping the phase fluctuation regime derives contributions from disorder as well as deficiency of mobile carriers. We expect that electron irradiation of $YBa_2Cu_3O_{7-\delta}$ with $\delta > 0.4$ would enhance their T_ν.

8.4 Conclusion

In summary, we have performed measurements of the Nernst effect, resistivity and Hall effect on Pr-substituted $YBa_2Cu_3O_{7-\delta}$ films. We find that an anomalous large Nernst signal survives above the superconducting transition temperature in the Pr-rich samples. This large Nernst voltage is attributed to vortex-like excitations in a phase incoherent superfluid existing above T_c. The regime of temperature over which these fluctuations prevail broadens with the Pr concentration. We attribute this effect primarily to the out-of-plane disorder caused by praseodymium, which is consistent with the measurements on other YBCO cuprates with in-plane and out-of-plane disorders. However, we do not completely rule out the contribution of reduced carrier concentration, particularly in the Pr-rich sample ($x \approx 0.5$).

Chapter 9

Summary and Future Research

This chapter contains summaries of the novel transport results we have obtained on the electron-doped cuprate superconductor $Pr_{2-x}Ce_xCuO_{4-\delta}$ (PCCO), and the Nernst and Hall effects study of Pr doped $YBa_2Cu_3O_{7-\delta}$. We will concentrate on the salient results of PCCO and give suggestions for future work.

9.1 Summary of thermotransport of $Pr_{2-x}Ce_xCuO_{4-\delta}$

Our Nernst effect and thermoelectric power experiments revealed several important aspects of the physics of electron-doped cuprates.

First, the Nernst effect, as a sensitive probe of the electronic band structure, is expected to be very small for metals with simple electron or hole Fermi surfaces. Experiments (ARPES) and band structure calculations (Ref. [58, 59]) suggest a simple hole-like Fermi surface in the overdoped regime of electron-doped cuprates due to the absence of antiferromagnetism (or spin-density wave, and therefore, a small Nernst signal is expected. However, our experiments revealed a fairly large normal state Nernst signal in highly overdoped (and underdoped) $Pr_{2-x}Ce_xCuO_{4-\delta}$ films, when compared to the Nernst signal observed in optimally-doped samples (as found here and reported previously). This observation is in contradiction with the band structure expectations. It is suggested that this is either due to a possible two

band contribution or to the thermal spin fluctuations we found in the high-field Hall effect experiments. A simple one Fermi pocket is not compatible with our Nernst effect data. Further investigations, both experimental and theoretical, are needed to clarify this contradiction.

Second, a careful low temperature (T around T_c) vortex Nernst effect measurement on $Pr_{2-x}Ce_xCuO_{4-\delta}$ films in the entire superconducting doping range ($0.13 \leq x \leq 0.19$) revealed a broad superconducting fluctuation effect in the underdoped region, similar to the hole-doped case. A vortex Nernst signal peak persists up to 6 K above T_c (11 K) in the underdoped x=0.13 film. The onset temperature of this "normal state" vortex Nernst signal (T_ν) decreases with increased doping. The linear normal state Nernst signal is completely recovered right at T_c in the overdoped region, suggesting the absence of superconducting fluctuations. Because of a larger in-plane coherence length in electron-doped cuprates with respect to their hole-doped counterparts, a stronger amplitude fluctuation of the superconductivity is expected. However, exactly the opposite is found, which suggests that amplitude fluctuations are unlikely to be origin of these fluctuation effects. Moreover, the dramatic increase of superfluid density with increased doping implies less phase fluctuations in the overdoped region. This is consistent with our data and thus suggests that the normal state vortex Nernst effect is due to incoherent phase fluctuations.

9.2 Summary of high-field transport of $Pr_{2-x}Ce_xCuO_{4-\delta}$

For the first time, we performed electrical transport experiments (resistivity and Hall effect) on electron-doped cuprate $Pr_{2-x}Ce_xCuO_{4-\delta}$ ($0.11 \leq x \leq 0.19$) films in a pulsed magnetic field (up to 60 T) at low temperatures (1.5 K$\leq$T$\leq$150 K). Interestingly, in the underdoped films, the linear Hall resistivity in low field persists up to 58 T at all the measured temperatures. In contrast, for the dopings of $x \geq 0.15$, a strong field dependent non-linear Hall resistivity is observed at low temperatures. The temperature regime that the nonlinearity appears increases with further doping; the nonlinear Hall resistivity starts from the lowest temperature (1.5 K) near optimal doping, while it is 10 K and 30 K for the overdoped x=0.17 and 0.19 respectively. Below these temperatures, the Hall resistivity is always linear at all fields in the overdoped films. At much higher temperatures, the linear Hall resistivity seems to be recovered for all the dopings. This nonlinear high field Hall resistivity suggests a contribution of both electron and hole bands.

The in-plane magnetoresistance measurements also show interesting features at high field. The low temperature negative magnetoresistance, argued to be a result of spin scattering, extends up to 58 T in the underdoped films, while it switches to positive at optimal doping, suggesting a suppression of the spin contributions. In the overdoped region, a crossover of the field dependence of magnetoresistance is observed. The low field quadratic magnetoreistance becomes linear in high field.

To explain these anomalous high field behaviors in Hall resistivity and magnetoresistance, we attempted to fit the data with a simple two-band Drude model.

However, we could not fit both Hall resistivity and magnetoresistance with the same parameters. In addition, the fitting parameters (Hall numbers) for the optimally-doped films are in contradiction with the estimation from the areas of the Fermi pockets found in ARPES experiments. This shows that a simple two-band Drude model is not valid in the electron-doped cuprates with a complex Fermi surface.

Alternatively, we speculated that the non-linear Hall resistivity is a result of spin density wave induced Fermi surface reconstruction in high field. The large SDW gap allows the survival of the electron Fermi pockets in high fields in the underdoped region, while the suppression of the smaller SDW gap with field near optimal doping results in a change of Fermi surface, which allows the hole band to contribute at high field. This is consistent with our measurements. For the overdoped films, we attribute the nonlinear Hall resistivity in the intermediate temperature range to thermal spin fluctuations in a quantum critical region. The high field linear magnetoresistance in overdoped films is also compatible with this speculation. Our interpretation involves the vanishing of a spin density wave gap at the critical doping, and therefore, our high field data also support the view that a quantum phase transition occurs near optimal doping in the electron-doped cuprates.

A systematic study of resistive superconducting transition in $Pr_{2-x}Ce_xCuO_{4-\delta}$ films for magnetic field applied parallel to the conducting ab-planes were carried out in pulsed magnetic field. The extrapolated zero temperature parallel critical field ($H_{c2\|ab}(0)$) exceeds 58 T for the underdoped and optimally-doped films. For the overdoped films, 58 T is sufficient to suppress the superconductivity. We found that the Zeeman energy $\mu_B H_{c2\|ab}(0)$ reaches the superconducting gap ($\triangle_0$), i.e.

$\mu_B H_{c2\|ab}(0) \simeq \triangle_0$, for all the dopings. This strongly suggests that the parallel critical field is determined by the Pauli paramagnetic limit in electron-doped cuprates.

9.3 Summary of Nernst effect of $Y_{1-x}Pr_xBa_2Cu_3O_{7-\delta}$

The very strong superconducting fluctuations in the hole-doped cuprates (such as LSCO) as reported recently is an interesting topic in superconductivity research. The votexlike excitations extends well into a pesudogap temperature regime well above T_c in these materials suggests a possible correlation. $Y_{1-x}Pr_xBa_2Cu_3O_{7-\delta}$ is a system of interest for studying the pseudugap effect. We performed measurements of Nernst effect, resistivity and Hall angle on epitaxial films of $Y_{1-x}Pr_xBa_2Cu_3O_{7-\delta}$ ($0 \leq x \leq 0.4$) over a broad range of temperature and magnetic field. Similar to prior reports, our Hall and resistivity data suggest a broad pseudogap regime with more Pr doping. The Nernst effect on Pr doped YBCO films show a large signal above the superconducting transition temperature T_c, which is similar to the observations in other hole-doped cuprates. It thus suggests vortex-like excitations in the phase incoherent condensate existing above T_c in this material. We also establish a correlation between disorder and the width of the phase fluctuation regime for the YBCO family of cuprates, which suggests a $T_c \simeq 110$ K for disorder-free $YBa_2Cu_3O_{7-\delta}$.

9.4 Future research

The low temperature thermotransport experiments that we carried out on $Pr_{2-x}Ce_xCuO_{4-\delta}$ films have provided us some important information for under-

standing of electron-doped cuprates. However, there are still many important issues that need to be clarified in the near future. First, the normal state themopower of PCCO at ultra low temperature (T<2 K) is unknown due to the limit of our experimental setup. It is important to know if the finite thermopower offset at T→0 that we observed in the underdoped films at T= 2 K will actually still exist in low temperature measurments. The verification of this issue will confirm or deny the theory proposed by Yakovenko (see chapter 4).

Unlike the specific heat, there is no low temperature Schottky anomaly in thermopower measurements. Therefore, it could provide some information to the electron density of states at very low temperatures since thermopower is proportional to the specific heat. Another interesting perspective is to check the temperature dependence of the normal state thermopower at ultra-low temperatures near the critical doping ($x \sim 0.16$) to compare it to the theoretical expectation, $S/T \propto -lnT$ [84] for a metallic quantum critical point.

Further high magnetic field experiments will also be of interest. We have not measured the high temperature (T>100 K) Hall resistivity and magnetoresistance on PCCO films. As we speculated, in the quantum critical region, the spin fluctuations will affect the high field transports. It is important to know if the Hall resistivity is still linear at high temperatures and in high field when the spin density wave gap vanishes. Although our current result suggests a high temperature linearity at the optimal doping, it is important to complete the investigation.

Another interesting experiment is to check for a possible Shubnikov-de Haas (SDH) effect in the overdoped PCCO, which is supposed to have only one large

hole pocket at the Fermi surface. The recent discovery of quantum oscillations of the Hall resistance in an underdoped YBCO crystal under high magnetic field is argued to be a result of a small hole pocket at the Fermi surface [163]. For the overdoped electron-doped cuprates, the large hole-like Fermi pocket should give a high-frequency oscillation. However, sample quality is a problem. The disorder and defects in the PLD fabricated films would be an obstacle to such experimental observations. Therefore, it is crucial to have very clean overdoped samples. One way is to perform the high field measurement on the overdoped crystals, which are difficult to obtain from flux growth and a floating zone furnace is needed to grow such crystals. Another way is to get the high quality films grown in a MBE chamber. It has been shown that the residue resistivity of the MBE fabricated films is extremely small, which suggests that the films are very clean. If high quality sample can be prepared, it will be likely that SDH oscillation be observed. Such observation will confirm the single hole Fermi pocket conjecture in the overdoped region.

The high magnetic field can be utilized to investigate the pairing symmetry in electron-doped cuprates. Since the superconductivity can be suppressed in a 60 T pulsed magnetic field applied parallel to the ab-planes, the measurement of the resistivity upper critical field by rotating the sample in the ab-plane could provide information of the pairing symmetry. If it is d-wave pairing, one would expect a four-fold oscillation of the parallel H_{c2} due to the existence of gap nodes [164], otherwise, the H_{c2} should be angle independent if it is s-wave system.

For the Nernst effect measurements, which probe superconducting fluctuations, it would be interesting to further investigate the effect of disorder on the

hole-doped cuprates. Disorder can be introduced by proton or electron irradiation. Disorder should not affect the charge density, and therefore, if the anomalous Nernst signal is from the phase fluctuations, one would expect that the fluctuation regime should not change much since it is primarily determined by the superfluid density. This would certainly verify the incoherent phase fluctuation scenario for explaining the large vortexlike normal state Nernst signal in hole-doped cuprates.

Bibliography

[1] H. Kamerlingh Onnes, Leiden Comm. **120b, 122b, 124c** (1911).

[2] W. Meissner and R. Ochsenfeld, Naturwissenschaften **21**, 787 (1933).

[3] H. London and F. London, Proc. Roy. Soc.(London) **A149**, 71 (1935).

[4] M. Tinkham, *Introduction to Superconductivity*, 2nd ed. (McGraw-Hill, New York, 1996).

[5] H. Frohlich, Phys. Rev. **79**, 845 (1950).

[6] E. Maxwell, Phys. Rev. **78**, 477 (1950).

[7] J. Bardeen, L. N. Cooper, and J. R. Schrieffer, Phys. Rev. **108**, 1175 (1957).

[8] J. G. Bednorz and K. A. Müller, Z. Phys. B **64**, 189 (1986).

[9] M. K. Wu, J. R. Ashburn, C. J. Torng, P. Hor, R. L. Meng, L. Gao, Z. J. Huang, Y. Q. Wang, and C. W. Chu, Phys. Rev. Lett. **58**, 908 (1987).

[10] C. W. Chu, P. H. Hor, R. L. Meng, L. Gao, Z. J. Huang, and Y. Q. Wang, Phys. Rev. Lett. **58**, 405 (1987).

[11] H. Maeda, Y. Tanaka, and M. Fukutomi, Jpn. J. Appl. Phys. **27**, L209 (1988).

[12] Z. Z. Sheng, A. M. Hermann, A. El Ali, C. Almasan, J. Estrada, T. Datta, and R. J. Matson, Phys. Rev. Lett. **60**, 937 (1988).

[13] S. N. Putilin, E. V. Antipov, and O. Chmaissem, Nature(London) **362**, 226 (1993).

[14] L. Gao, Y. Y. Xue, F. Chen, Q. Xiong, R. L. Meng, D. Ramirez, and C. W. Chu, Phys. Rev. B **50**, 4260 (1994).

[15] Y. Tokura, H. Takagi, and S. Uchida, Nature(London) **337**, 345 (1989).

[16] N. P. Ong, *Physical Properties of High Temperature Superconductors*, ed. D. M. Ginsberg, World Scientific, Singapore (1990), Vol. 2, p.459.

[17] D. N. Basov and T. Timusk, Rev. Mod. Phys. **77**, 721 (2005).

[18] J. R. Waldram, *Superconductivity of Metals and Cuprates*, Institute of Physics Publishing Ltd. (1996), page 257.

[19] A. Damascelli, Z. Hussain, and Z.-X. Shen, Rev. Mod. Phys. **75**, 473, (2003).

[20] C. C. Tsui and J. R. Kirtley, Rev. Mod. Phys. **72**, 969 (2000).

[21] Dong Ho Wu, Jian Mao, S. N. Mao, J. L. Peng, X. X. Xi, T. Venkatesan, R. L. Greene, and Steven M. Anlage, Phys. Rev. Lett. **70**, 85 (1993).

[22] Q. Huang, J. F. Zasadzinski, N. Tralshawala, K. E. Gray, D. G. Hinks, J. L. Peng, and R. L. Greene, Nature(London) **347**, 369 (1990).

[23] R. Prozorov, R. W. Giannetta, P. Fournier, and R. L. Greene, Phys. Rev. Lett. **85**, 3700 (2000).

[24] N. P. Armitage, D. H. Lu, D. L. Feng, C. Kim, A. Damascelli, K. M. Shen, F. Ronning, Z.-X. Shen, Y. Onose, Y. Taguchi, and Y. Tokura, Phys. Rev. Lett. **86**, 1126 (2001).

[25] T. Sato, T. Kamiyama, T. Takahashi, K. Kurahashi, and K. Yamada, Science **291**, 1517 (2001).

[26] C. C. Tsuei and J. R. Kirtley, Phys. Rev. Lett. **85**, 182 (2000).

[27] G. Blumberg, A. Koitzsch, A. Gozar, B. S. Dennis, C. A. Kendziora, P. Fournier, and R. L. Greene, Phys. Rev. Lett. **88**, 107002 (2002).

[28] M. R. Norman and C. Pepin, Rep. Prog. Phys. **66**, 1547 (2003).

[29] R. J. Cava, A. Santoro, and D. W. Johnson, Phys. Rev. B **35**, 6716 (1987).

[30] H. K. Müller-Buschbaum *et al.*, Anorg. Allg. Chem. **414**, 76 (1975).

[31] M. Francois, E. Walker, and J. L. Jorda, Solid State Commun. **63**, 1149 (1987).

[32] T. Timusk and B. Statt, Reports on Progress in Physics, **62**, 61 (1999).

[33] L. Benfatto, S. Caprara, C. Castellani, A. Paramekanti, and M. Randeria, Phys. Rev. B **63**, 174513 (2001).

[34] Sudip Chakravarty, R. B. Laughlin, Dirk K. Morr, and Chetan Nayak, Phys. Rev. B **63**, 094503 (2001).

[35] G. M. Luke, L. P. Le, B. J. Sternlieb, Y. J. Uemura, J. H. Brewer, R. Kadono, R. F. Kiefl, S. R. Kreitzman, T. M. Riseman, C. E. Stronach, M. R. Davis, S. Uchida, H. Takagi, Y. Tokura, Y. Hidaka, T. Murakami, J. Gopalakrishnan, A. W. Sleight, M. A. Subramanian, E. A. Early, J. T. Markert, M. B. Maple, and C. L. Seaman, Phys. Rev. B **42**, 7981 (1990).

[36] T. Uefuji, K. Kurahashi, M. Fujita, M. Matsuda, and K. Yamada, Physica **C378**, 273 (2002).

[37] H. J. Kang, Pengcheng Dai, J. W. Lynn, M. Matsuura, J. R. Thompson, Shou-Cheng Zhang, D. N. Argyriou, Y. Onose, and Y. Tokura, Nature(London) **423**, 522 (2003).

[38] E. M. Motoyama, G. Yu, I. M. Vishik, O. P. Vajk, P. K. Mang, and M. Greven, Nature(London) **445**, 186 (2007).

[39] W. E. Pickett, *Electronic structure of the high-temperature oxide superconductors*, Rev. Mod. Phys. **61**, 433 (1989).

[40] H. J. Kang, Pengcheng Dai, H. A. Mook, D. N. Argyriou, V. Sikolenko, J. W. Lynn, Y. Kurita, Seiki Komiya, and Yoichi Ando, Phys. Rev. B **71**, 214512 (2005).

[41] J. Orenstein and A. Millis, Science **288**, 468 (2000).

[42] V. J. Emery, Phys. Rev. Lett. **58**, 2794 (1987).

[43] C. M. Varma, S. Schmitt-Rink, and E. Abrahams, Solid State Communications **62**, 681 (1987).

[44] F. C. Zhang and T. M. Rice, Phys. Rev. B **37**, 3759 (1988).

[45] Z. Z. Wang, T. R. Chien, N. P. Ong, J. M. Tarascon, and E. Wang, Phys. Rev. B **43**, 3020 (1991).

[46] Wu Jiang, S. N. Mao, X. X. Xi, Xiuguang Jiang, J. L. Peng, T. Venkatesan, C. J. Lobb, and R. L. Greene, Phys. Rev. Lett. **73**, 1291 (1994).

[47] P. Fournier, X. Jiang, W. Jiang, S. N. Mao, T. Venkatesan, C. J. Lobb, and R. L. Greene, Phys. Rev. B **56**, 14149 (1997).

[48] F. Gollnik and M. Naito, Phys. Rev. B **58**, 11734 (1998).

[49] Y. Dagan, M. M. Qazilbash, C. P. Hill, V. N. Kulkarni, and R. L. Greene, Phys. Rev. Lett. **92**, 167001 (2004).

[50] N. P. Armitage, F. Ronning, D. H. Lu, C. Kim, A. Damascelli, K. M. Shen, D. L. Feng, H. Eisaki, Z.-X. Shen, P. K. Mang, N. Kaneko, M. Greven, Y. Onose, Y. Taguchi, and Y. Tokura, Phys. Rev. Lett. **88**, 257001 (2002).

[51] H. Matsui, K. Terashima, T. Sato, T. Takahashi, S.-C. Wang, H.-B. Yang, H. Ding, T. Uefuji, and K. Yamada, Phys. Rev. Lett. **94**, 047005 (2005); H. Matsui, K. Terashima, T. Sato, T. Takahashi, M. Fujita, and K. Yamada, Phys. Rev. Lett. **95**, 017003 (2005).

[52] J. Bok, G. Deutscher, D. Pavuna, and S. A. Wolf, editors, *The gap symmetry and fluctuations in high Tc superconductors* (Plenum Press, New York, 1998), chap. The Spin Fluctuation Model for High Temperature Superconductivity: Progress and Prospects by David Pines.

[53] H. Matsui, APS March Meeting, Abstract: K3.00003, (2006); H. Matsui, T. Takahashi, T. Sato, K. Terashima, H. Ding, T. Uefuji, and K. Yamada, Phys. Rev. B **75**, 224514 (2007).

[54] Subir Sachdev, Science **288**, 475 (2000).

[55] Y. Dagan, M. C. Barr, W. M. Fisher, R. Beck, T. Dhakal, A. Biswas, and R. L. Greene, Phys. Rev. Lett. **94**, 057005 (2005).

[56] P. Fournier, P. Mohanty, E. Maiser, S. Darzens, T. Venkatesan, C. J. Lobb, G. Czjzek, R. A. Webb, and R. L. Greene, Phys. Rev. Lett. **81**, 4720 (1998).

[57] A. Zimmers, J. M. Tomczak, R. P. S. M. Lobo, N. Bontemps, C. P. Hill, M. C. Barr, Y. Dagan, R. L. Greene, A. J. Millis, and C. C. Homes, Europhys. Lett. **70**, 225 (2005); Y. Onose, Y. Taguchi, K. Ishizaka, and Y. Tokura, Phys. Rev. Lett. **87**, 217001 (2001).

[58] J. Lin and A. J. Millis, Phys. Rev. B **72**, 214506 (2005).

[59] A. J. Millis, A. Zimmers, R. P. S. M. Lobo, N. Bontemps, and C. C. Homes, Phys. Rev. B **72**, 224517 (2005).

[60] M. P. Marder, *Condensed Matter Physics* (John Wiley & Sons, Inc., New York, 2000).

[61] J. M. Ziman, *Electrons and Phonons, The Theory of Transport Phenomena in Solids* (Oxford University Press, 1960).

[62] N. W. Ashcroft & N. D. Mermin, *Solid State Physics* (Saunders College Publishing, 1976).

[63] C. M. Hurd, *The Hall Effect in Metals and Alloys* (Plenum Press, New York-London, 1972).

[64] R. D. Barnard, *Thermoelectricity in metals and alloys* (John Wiley & Sons, New York, 1972).

[65] Yayu Wang, Z. A. Xu, T. Kakeshita, S. Uchida, S. Ono, Yoichi Ando, and N. P. Ong, Phys. Rev. B **64**, 224519 (2001).

[66] N. P. Ong, Phys. Rev. B **43**, 193 (1991).

[67] Romain Bel, Kamran Behnia, and Helmuth Berger, Phys. Rev. Lett. **91**, 066602 (2003).

[68] Yayu Wang, Ph.D thesis, (2004).

[69] E. Maiser, P. Fournier, J.-L. Peng, F. M. Araujo-Moreira, T. Venkatesan, R. L. Greene, and G. Czjzek, Physica **C297**, 15 (1998).

[70] J. L. Peng, E. Maiser, T. Venkatesan, R. L. Greene, and G. Czjzek, Phys. Rev. B **55**, R6145 (1997).

[71] Hye Jung Kang, Pengcheng Dai, Branton J. Campbell, Peter J. Chupas, Stephan Rosenkranz, Peter L. Lee, Qingzhen Huang, Shiliang Li, Seiki Komiya, and Yoichi Ando, Nature Materials **6**, 224 (2007).

[72] Y. Wang, N. S. Rogoado, R. J. Cava, and N. P. Ong, Nature(London) **423**, 425 (2003).

[73] A. Migliori; F. F. Balakirev, J. B. Betts; G. S. Boebinger, C. H. Mielke, and D. Rickel, Int. J. Mod. Phys. B, **16**, 3398 (2002)

[74] Yoichi Ando, S. Ono, X. F. Sun, J. Takeya, F. F. Balakirev, J. B. Betts, and G. S. Boebinger, Phys. Rev. Lett.**92**, 247004 (2004) and references therein.

[75] J. L. Tallon and J. W. Loram, Physica C**349**, 53 (2001).

[76] Guo-qing Zheng, P. L. Kuhns, A. P. Reyes, B. Liang, and C. T. Lin, Phys. Rev. Lett. **94**, 047006 (2005).

[77] R. C. Budhani, M. C. Sullivan, C. J. Lobb, and R. L. Greene, Phys. Rev. B **65**, R100517 (2002).

[78] C. H. Wang, G. Y. Wang, T. Wu, Z. Feng, X. G. Luo, and X. H. Chen, Phys. Rev. B **72**, 132506 (2005).

[79] K. Miyake and H. Kohno, J. Phys. Soc. Jpn, **74**, 254 (2005).

[80] K. Behnia, D. Jaccard, and J. Flouquet, J. Phys.: Condens. Matter **16**, 5187 (2004).

[81] P. Fournier, J. Higgins, H. Balci, E. Maiser, C. J. Lobb, and R. L. Greene, Phys. Rev. B **62**, R11993 (2000).

[82] H. Balci and R. L. Greene, Phys. Rev. B **70** 140508(R) (2004).

[83] P. K. Mang, O. P. Vajk, A. Arvanitaki, J. W. Lynn, and M. Greven, Phys. Rev. Lett. **93**, 027002 (2004).

[84] I. Paul and G. Kotliar, Phys. Rev. B **64**, 184414 (2001).

[85] V. Yakovenko and Pengcheng Li, unpublished.

[86] V. A. Khodel, M. V. Zverev, and Victor M. Yakovenko, Phys. Rev. Lett. **95**, 236402 (2005) and references therein.

[87] J. Fenton and A. J. Schofield, Phys. Rev. Lett. **95**, 247201 (2005).

[88] E. Fawcett, Rev. Mod. Phys. **60**, 209 (1988).

[89] George Gruner, *Density Waves in Solids*, (Westview Press, 2000).

[90] M. Matsuda, Y. Endoh, K. Yamada, H. Kojima, I. Tanaka, R. J. Birgeneau, M. A. Kastner, and G. Shirane, Phys. Rev. B **45**, 12548 (1992).

[91] H. Kimura, K. Hirota, H. Matsushita, K. Yamada, Y. Endoh, S.-H. Lee, C. F. Majkrzak, R. Erwin, G. Shirane, M. Greven, Y. S. Lee, M. A. Kastner, and R. J. Birgeneau, Phys. Rev. B **59**, 6517 (1999).

[92] Y. S. Lee, R. J. Birgeneau, M. A. Kastner, Y. Endoh, S. Wakimoto, K. Yamada, R. W. Erwin, S.-H. Lee, and G. Shirane, Phys. Rev. B **60**, 3643 (1999).

[93] O. K. Andersen, A. I. Liechtenstein, O. Jepsen, and F. Paulsen, J. Phys. Chem. Solids **56**, 1573 (1995).

[94] F. F. Balakirev, J. B. Betts, A. Migliori, S. Ono, Y. Ando, and G. S. Boebinger, Nature(London) **424**, 912 (2003).

[95] M. Abdel-Jawad, M. P. Kennett, L. Balicas, A. Carrington, A. P. Mackenzie, R. H. McKenzie, and N. E. Hussey, Nature Physics, **2**, 821 (2006).

[96] Y. Ando, G. S. Boebinger, A. Passner, L. F. Schneemeyer, T. Kimura, M. Okuya, S. Watauchi, J. Shimoyama, K. Kishio, K. Tamasaku, N. Ichikawa, and S. Uchida, Phys. Rev. B **60**, 12475 (1999).

[97] P. Fournier and R. L. Greene, Phys. Rev. B **68**, 094507 (2003).

[98] N. Werthamer, E. Helfand, and P. Hohenberg, Phys. Rev. **147**, 295 (1966).

[99] Y. Wang, L. Li, and N. P. Ong, Phys. Rev. B **73**, 024510 (2006) and references therein.

[100] J. L. O'Brien, H. Nakagawa, A. S. Dzurak, R. G. Clark, B. E. Kane, N. E. Lumpkin, N. Miura, E. E. Mitchell, J. D. Goettee, J. S. Brooks, D. G. Rickel, and R. P. Starrett, Phys. Rev. B **61**, 1584 (2000).

[101] T. Sekitani, N. Miura, S. Ikeda, Y. H. Matsuda, and Y. Shiohara, Physica B **346**, 319 (2004).

[102] S. I. Vedeneev, A. G. M. Jansen, E. Haanappel, and P. Wyder, Phys. Rev. B **60**, 12467 (1999).

[103] A. S. Dzurak, B. E. Kane, R. G. Clark, N. E. Lumpkin, J. OBrien, G. R. Facer, R. P. Starrett, and A. Skougarevsky *et al.*, Phys. Rev. B **57**, R14084 (1998).

[104] U. Welp, W. K. Kwok, G. W. Crabtree, K. G. Vandervoort, and J. Z. Liu, Phys. Rev. Lett. **62**, 1908 (1989).

[105] S. I. Vedeneev, Cyril Proust, V. P. Mineev, M. Nardone, and G. L. J. A. Rikken, Phys. Rev. B **73**, 014528 (2006).

[106] H. Balci, C. P. Hill, M. M. Qazilbash, and R. L. Greene, Phys. Rev. B **68**, 054520 (2003).

[107] M. M. Qazilbash, A. Koitzsch, B. S. Dennis, A. Gozar, H. Balci, C. A. Kendziora, R. L. Greene, and G. Blumberg, Phys. Rev. B **72**, 214510 (2005).

[108] R. A. Klemm, A. Luther, and M. R. Beasley, Phys. Rev. B **12**, 877 (1975).

[109] F. Harper and M. Tinkham, Phys. Rev. **172**, 441 (1968).

[110] S. Vedeneev and Y. N. Ovichinnikov, JETP Lett. **75**, 195 (2002).

[111] A. Clogston, Phys. Rev. Lett. **3**, 266 (1962); B. Chandrasekhar, Appl. Phys. Lett. **1**, 7 (1962).

[112] C. C. Homes, R. P. S. M. Lobo, P. Fournier, A. Zimmers, and R. L. Greene, Phys. Rev. B **74**, 214515 (2006).

[113] K. Yang, S. L. Sondhi, Phys. Rev. B **57**, 8566 (1998).

[114] C. Grimaldi, J. Phys.: Condens. Matter. **12**, 1329 (2000).

[115] Y. Dagan, M. M. Qazilbash, and R. L. Greene, Phys. Rev. Lett. **94**, 187003 (2005).

[116] I. L. Aleiner and B. L. Altshuler, Phys. Rev. Lett. **79**, 4242 (1997).

[117] A. A. Abrikosov, JETP **5**, 1174 1957.

[118] B. D. Josephson, Physics Letters **1**, 251 (1962).

[119] R. P. Huebener, *Magnetic Flux Structures in Superconductors*, 1st ed. (Springer-Verlag, Berlin, 1979).

[120] F. Vidal, Phys. Rev. B **8**, 1982 (1973).

[121] D. S. Fisher, M. P. A. Fisher, and D. Huse, Phys. Rev. B. **43**, 130 (1991).

[122] S. Ullah and A. T. Dorsey, Phys. Rev. Lett. **65**, 2066 (1990); S. Ullah and A. T. Dorsey, Phys. Rev. B **44**, 262 (1991).

[123] R. J. Troy and A. T. Dorsey, Phys. Rev. B. **47**, 2715 (1993).

[124] A. I. Larkin and A. A. Varlamov, *The Physics of Superconductors, Vol 1: Conventional and High-Tc Superconductors* (Springer, Berlin, 2003).

[125] Z. Xu, N.P. Ong, Y. Wang, T. Kakeshita, and S. Uchida, Nature(London) **406**, 486 (2000).

[126] V. J. Emery and S. A. Kivelson, Nature(London) **374**, 434 (1995).

[127] I. Ussishkin and S. L. Sondhi, Int. J. Mod. Phys. B **18**, 3315 (2004); I. Ussishkin, S. L. Sondhi, and D. A. Huse, Phys. Rev. Lett. **89**, 287001 (2002).

[128] E. W. Carlson, V. J. Emery, S. A. Kivelson, and D. Orgad, *The Physics of Conventional and Unconventional Superconductors* ed. K. H. Bennemann and J. B. Ketterson (Springer-Verlag); cond-mat 0206217 (2002).

[129] H. Kontani, Phys. Rev. Lett. **89**, 237003 (2002).

[130] S. Tan and K. Levin, Phys. Rev. B **69**, 064510 (2004).

[131] C. Honerkamp and P. A. Lee, Phys. Rev. Lett. **92**, 177002 (2004).

[132] R. Ikeda, Phys. Rev. B **66**,100511, (2002).

[133] A. S. Alexandrov, Phys. Rev. Lett. **93**, 217002 (2004).

[134] P. W. Anderson, Phys. Rev. Lett. **96**, 017001 (2006)

[135] L. Alff, Y. Krockenberger, B. Welter, M. Schonecke, R. Gross, D. Manske, and M. Naito, Nature(London) **406**, 486 (2000).

[136] C. C. Homes, B. P. Clayman, J. L. Peng, and R. L. Greene, Phys. Rev. B **56**, 5525 (1997).

[137] A. Koitzsch, G. Blumberg, A. Gozar, B. S. Dennis, P. Fournier, and R. L. Greene, Phys. Rev. B **67**, 184522 (2003).

[138] N. P. Armitage, D. H. Lu, C. Kim, A. Damascelli, K. M. Shen, F. Ronning, D. L. Feng, P. Bogdanov, Z.-X. Shen, Y. Onose, Y. Taguchi, Y. Tokura, P. K. Mang, N. Kaneko, and M. Greven, Phys. Rev. Lett. **87**, 147003 (2001).

[139] N. P. Ong, Y. Wang, S. Ono, Y. Ando, and S. Uchida, Annalen der Physik(Leipzig) **13**, 9 (2004).

[140] A. Snezhko, R. Prozorov, D. D. Lawrie, R. W. Giannetta, J. Gauthier, J. Renaud, and P. Fournier, Phys. Rev. Lett. **92**, 157005 (2004).

[141] A. Ino, C. Kim, M. Nakamura, T. Yoshida, T. Mizokawa, A. Fujimori, Z.-X. Shen, T. Kakeshita, H. Eisaki, and S. Uchida, Phys. Rev. B **65**, 094504 (2002).

[142] V. Oganesyan and I. Ussishkin, Phys. Rev. B **70**, 054503 (2004).

[143] Y. Dagan and R. L. Greene, to be published in Phys. Rev. B (2007).

[144] T. R. Chien, Z. Z. Wang and N. P. Ong, Phys. Rev. Lett. **67**, 2088 (1991); J. M. Harris, Y. F. Yan, and N. P. Ong, Phys. Rev. B **46**, 14297 (1992); A. Carrington, A. Mackenzie, C. T. Lin, and J. R. Cooper, Phys. Rev. Lett. **69**, 2855 (1992).

[145] P. W. Anderson, Phys. Rev. Lett. **67**, 2092 (1991).

[146] E. Abrahams and C. M. Varma, Phys. Rev. B **68**, 094502 (2003).

[147] C. Kendziora, D. Mandrus, L. Mihaly, and L. Forro, Phys. Rev. B **46**, 14297 (1992); N. E. Hussey, J. R. Cooper, J. M. Wheatley, I. R. Fisher, A. Carrington, A. P. Mackenzie, C. T. Lin, and O. Milat, Phys. Rev. Lett. **76**, 122 (1996).

[148] B. P. Stojkovic and D. Pines, Phys. Rev. Lett. **76**, 811 (1996).

[149] J. L. Tallon, J. R. Cooper, P. S. I. P. N. de Silva, G. V. M. Williams, and J. W. Loram, Phys. Rev. Lett. **75**, 4114 (1995).

[150] Kamran Behnia, Marie-Aude Masson, and Yakov Kopelevich, Phys. Rev. Lett. **98**, 076603 (2007).

[151] V. Z. Kresin and S. A. Wolf, Phys. Rev. B **41**, 4278 (1990).

[152] Yayu Wang, Lu Li, M. J. Naughton, G. D. Gu, S. Uchida, and N. P. Ong, Phys. Rev. Lett. **95**, 247002 (2005).

[153] F. Rullier-Albenque, R. Tourbot, H. Alloul, P. Lejay, D. Colson, and A. Forget, Phys. Rev. Lett. **96**, 067002 (2006).

[154] K. Fujita, T. Noda, K. M. Kojima, H. Eisaki, and S. Uchida, Phys. Rev. Lett. **95**, 097006 (2005).

[155] V. Sandu, E. Cimpoiasu, T. Katuwal, C. C. Almasan, Shi Li, and M. B. Maple, Phys. Rev. Lett. **93**, 177005 (2004).

[156] Peng Xiong, Gang Xiao, and X. D. Wu, Phys. Rev. B **47**, 5516R (1992).

[157] Wu Jiang, J. L. Peng, S. J. Hagen, and R. L. Greene, Phys. Rev. B **46**, 8694(R) (1992).

[158] M. B. Maple, J. Magn. Magn. Mater. **177**, 18 (1998).

[159] M. Covington and L. H. Greene, Phys. Rev. B **62**, 12440 (2000).

[160] H. Y. Hwang, B. Batlogg, H. Takagi, H. L. Kao, J. Kwo, R. J. Cava, J. J. Krajewski, and W. F. Peck, Jr., Phys. Rev. Lett. **72**, 2636 (1994).

[161] D. Matthey, S. Gariglio, B. Giovannini, and J.-M Triscone, Phys. Rev. B **64**, 024513 (2001).

[162] Z. A. Xu, J. Q. Shen, S. R. Zhao, Y. J. Zhang, and C. K. Ong, Phys. Rev. B **72**, 144527 (2005).

[163] Nicolas Doiron-Leyraud, Cyril Proust, David LeBoeuf, Julien Levallois, Jean-Baptiste Bonnemaison, Ruixing Liang, D.A. Bonn, W.N. Hardy, and Louis Taillefer, Nature(London) **447**, 565 (2007).

[164] Franziska Weickert, Philipp Gegenwart, Hyekyung Won, David Parker, and Kazumi Maki, Phys. Rev. B **74**, 134511 (2006).